Dissertation Thesis

Czech
Technical
University
in Prague

F6

Faculty of Transportation Sciences
Department of Mechanics and Materials

Mechanical Behavior of Materials under High Strain-rates Investigated by SHPB

Dynamic Properties of Cellular Meta-materials

Tomáš Fíla

Supervisor: prof. Ing. Ondřej Jiroušek, Ph.D.
Supervisor–specialist: doc. Ing. Daniel Kytýř, Ph.D.
Field of study: Technology in Transportation and Telecommunication
Subfield: Transportation Systems and Technology
March 2020

Acknowledgements

I would like to thank my supervisor prof. Ondřej Jiroušek and my supervisor-specialist assoc. prof. Daniel Kytýř for providing me the leadership, supervision, advisory, and financial support during the work on the thesis. I would like to further thank all my colleagues in the team who helped me during both the design and commissioning phase of the experimental setup and during the subsequent experimental campaigns. Among many of my friends and team members, special thanks belong particularly to Petr Zlámal, Petr Koudelka, Jan Falta, Marcel Adorna, and Tomáš Doktor. Here, I have to also express thanks to the Institute of Theoretical and Applied Mechanics of the Czech Academy of Sciences for supporting me during my doctoral studies and for its technical, professional, and financial background. I would also thank to my wife Kateřina, my children Matěj and Michaela and to the rest of my family for providing me support and for their attitude and comprehension during my studies. The support of the following projects:

15-15480S,
19-23675S,
SGS17/148/OHK2/2T/16,
SGS18/153/OHK2/2T/16,
SGS18/154/OHK2/2T/16 and
CZ.02.1.01/0.0/0.0/16_019/0000766

is also gratefully acknowledged.

Declaration

I hereby submit, for the evaluation, and defense, the doctoral thesis elaborated at the CTU in Prague, Faculty of Transportation Sciences.

I have no relevant reason against using this schoolwork in the sense of paragraph 60 of Act No. 121/2000 Coll. on the Copyrights and Rights Related to Copyright and on the Amendment to Certain Acts (the Copyright Act).

I declare I have accomplished my final thesis by myself and I have named all the sources used in accordance with the Guideline on ethical preparation of university final theses.

In this thesis, the selected results, images and parts of the texts from the contributions listed as the references no. [1–7] were used. In all the cases, I am the corresponding author of the contributions or one of the main authors and there is no conflict in copyright agreements for them to be published as a part of the dissertation thesis.

Tomáš Fíla
Prague, 5. March 2020

Abstract

This doctoral thesis is focused on the experimental analysis of cellular meta-materials subjected to a dynamic impact with a high strain-rate. In particular, additively manufactured auxetic lattices (structures with a negative Poisson's ratio) are investigated. Two in-house Hopkinson bar experimental setups are developed for the testing of the structures: i) a conventional Split Hopkinson Pressure Bar (SHPB, Kolsky bar), and ii) a novel direct impact Open Hopkinson Pressure Bar (OHPB). Both setups are tailored for the application on the low impedance materials and are used for the experiments subjecting the cellular meta-materials to a high strain-rate uni-axial compression. In the thesis, the developed apparatuses, the instrumentation, evaluation methods and the experimental program are described in detail. The experiments are optically inspected using several high-speed cameras and a digital image correlation technique is employed for the advanced analysis of the deformation behavior of the meta-materials. Using the data from several experimental campaigns, the strain-rate sensitivity of the selected auxetic lattices and their Poisson's ratio is investigated in detail. It is found out that the auxetic structures are, in general, strain-rate sensitive and their Poisson's ratio is both strain-rate and strain dependent. Other representative results exploiting the deformation behavior of cellular materials, e.g., hybrid open-cell foams and hybrid hollow strut auxetic lattices are also presented in the study.

Keywords: Hopkinson bar, SHPB, direct impact Hopkinson bar, OHPB, impact energy absorption, strain-rate sensitivity, cellular materials, interpenetrating phase composites (IPCs), meta-materials, digital image correlation (DIC), additive manufacturing

Supervisor: prof. Ing. Ondřej Jiroušek, Ph.D.
Department of Mechanics and Materials, FTS
CTU in Prague
Na Florenci 25,
110 00 Prague 1,
Czech Republic

Abstrakt

Tato dizertační práce je zaměřena na experimentální analýzu buněčných (celulárních) metamateriálů při dynamickém rázu za vysokých rychlostí deformace. Analyzovány jsou zejména aditivně vyráběné auxetické struktury (materiály se záporným Poissonovým číslem). Za tímto účelem byla vyvinuta dvě experimentální zařízení: i) konvenční dělená Hopkinsonova tyč (Split Hopkinson Pressure Bar - SHPB) a ii) inovativní zařízení OHPB (Open Hopkinson Pressure Bar) pro testování přímým rázem. Obě zařízení jsou navržena a optimalizována pro testování materiálů s nízkou mechanickou impedancí (měkkých materiálů) a jsou použity pro testování celulárních metamateriálů v jednoosém tlaku při rázu za vysokých rychlostí. V práci je detailně popsáno technické řešení obou experimentálních zařízení, jejich instrumentace, použité metody pro vyhodnocení i všechny experimentální programy provedené během studie. Experimenty byly opticky pozorovány s využitím více typů rychlokamer a data z nich byla dále zpracována pomocí metody digitální korelace obrazu (digital image correlation - DIC) pro pokročilou analýzu deformačních chování metamateriálů. Data z několika experimentálních kampaní byla použita pro analýzu citlivosti auxetických buněk na rychlost deformace a pro analýzu citlivosti Poissonova čísla na rychlost i velikost deformace. Je zjištěno, že auxetické struktury jsou obecně citlivé na rychlost deformace a že hodnota Poissonova čísla těchto struktur záleží jak na rychlosti tak velikosti deformace. V práci jsou dále uváděny některé reprezentativní výsledky dalších celulárních materiálů, především potom hybridních pěn s otevřenými póry a hybridních auxetických struktur s dutými pruty.

Klíčová slova: Hopkinsonova tyč, SHPB, Hopkinsonova tyč pro přímý ráz, OHPB, absorbéry kinetické energie, citlivost na rychlost deformace, celulární materiály, metamateriály, aditivní výroba, digitální korelace obrazu

Překlad názvu: Stanovení mechanického chování materiálů při rychlých deformacích metodou SHPB

Contents

5 Experiments and Results 101

Figures

Tables

Abbreviations

C/PU Polyurethane foam coated with carbon.

CMOS Complementary Metal Oxide Semiconductor.

DIC Digital Image Correlation.

DIHPB Direct Impact Hopkinson Pressure Bar.

DPI Dots per Inch.

FEM Finite Element Method.

FPA Focal Plane Array.

FPS Frames per Second.

HOPS Hybrid Optics Positioning System.

IIR Infinite Impulse Response.

IPC Interpenetrating Phase Composite.

LED Light Emitting Diode.

LWIR Long Wavelength Infrared.

MWIR Mid Wavelength Infrared.

NCC Normalized Cross-Correlation.

Ni/PU Polyurethane foam coated with nickel.

OHPB Open Hopkinson Pressure Bar.

PC Personal Computer.

PECS Pulsed Electric Current Sintering.

PM Powder Metallurgy.

PMMA Polymethyl methacrylate.

PNG Portable Network Graphics.

RC Remote Control.

RVE Representative Volume Element.

SHPB Split Hopkinson Pressure Bar.

SLM Selective Laser Melting.

SLS Selective Laser Sintering.

SNR Signal to Noise Ratio.

SWIR Short Wavelength Infrared.

Chapter 1

Introduction

In recent years, the dramatic development of modern, advanced and progressive methods for the production of new materials has occurred. Progress in the innovative methods of material production such as 3D printing, laser sintering, nanotechnology or advanced coating has allowed for the design of so-called meta-materials. Meta-materials can be described as materials that are engineered to exhibit properties that are not found in naturally occurring materials. Application of optimization techniques in the design process of meta-materials can be used to develop a material with beneficial properties tailored for a particular purpose. This approach opens a variety of applications of meta-materials in almost any field of engineering and technology. As the aim of this thesis is the measurement of the response of meta-materials at high strain-rates, the following examples will cover applications in the field of structural mechanics. In this field, the behavior of meta-materials can be used for the development of, e.g., lightweight structures of complex shapes, shock absorbers, or to optimize the elastic response of the material or affect its non-linear behavior, etc. However, as the internal structure of meta-materials is rather complex (often on all levels: micro, mezzo or macro), the description of their mechanical properties is non-trivial, dependent on many factors, and their behavior often exhibits mechanisms that are not well described and understood. Therefore, further extensive research aimed at the investigation of the mechanical properties and material behavior of meta-materials under different conditions is still needed for proper understanding the structure-mechanical property relationship.

The aim of this thesis is the investigation of the mechanical behavior of cellular meta-materials at high strain-rate impacts using the Hopkinson bar method. Most materials exhibit different mechanical properties and deformation behavior with an increasing deformation velocity. As the deformation mechanisms of the meta-materials during high-velocity impacts still have not been fully described, the thesis is focused particularly on the measurement methodology, instrumentation, experimental investigation, and advanced analysis of the cellular meta-materials subjected to the impact loading in a variety of Hopkinson bar apparatuses. In the first part of the thesis, an overview of the actual state-of-the-art is provided to embed the content of the thesis into the context of the actual research in this field. In the materials and methods part, the covered topics include the calculation and design of a Split Hopkinson Pressure Bar (SHPB) apparatus (with an emphasis on the key parameters for the testing of cellular meta-materials), the instrumentation of the Hopkinson bar including high-speed cameras and digital image correlation (DIC), the limitations of the SHPB method and the introduction of a novel Open Hopkinson Pressure Bar (OHPB) with beneficial properties for testing meta-materials. In the latter parts of the thesis, an overview of results of the selected Hopkinson bar experiments performed with various types of cellular meta-materials (e.g., selective laser sintered auxetic lattices, hybrid nickel-polyurethane open-cell foams, hybrid auxetic lattices, etc.) is shown together with the discussion of the observed deformation behavior. In the final part, the overall summary of the work is given and the major findings and conclusions based on the study are drawn.

All the experiments were carried out in the DynLab (Dynamic Laboratory) located at the Department of Mechanics and Materials of the Faculty of Transportation Sciences, Czech Technical University in Prague. The laboratory was established in 2016.

Chapter 2

State-of-the-art

The experimental and numerical investigation of the structural parameters and material behavior of meta-materials is a highly actual task that has been performed by a number of research teams. This part of the thesis summarizes the key contributions of the ongoing research, provides a comprehensive literature overview of the problem and serves as a basis for the author's own work. In this part, an overview of the relevant theoretical background together with the experimental investigation as well as the numerical analyses are shown.

2.1 Strain-rate effects and impact loading

Most materials exhibit, more or less, significant changes in the mechanical behavior with an increasing loading rate (strain-rate). These effects were initially observed and identified in bulk metallic materials during increased loading rates (e.g., during forming processes). The changes in the deformation behavior can be related to the nature of the internal structure of the material and phenomena such as the changing plastic-flow in the material, micro-localization of the plastic flow, and micro-inertia effects, or can be coupled with the thermal related effects in the material, particularly in the situation when the processes in the material are, due to the increasing strain-rate, no longer isothermal and exhibit adiabatic or even a more complex behavior. The fundamental diagram showing the strain-rate sensitive behavior of a material is shown in Fig. 2.1.

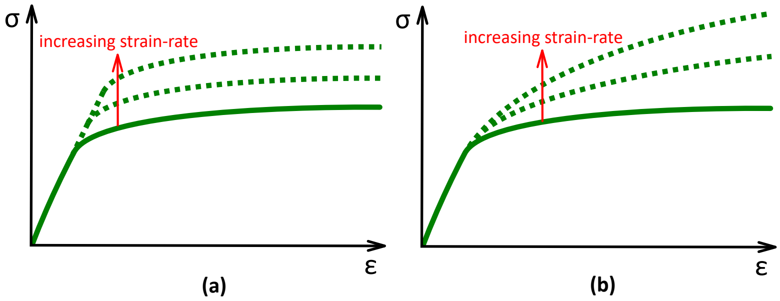

Figure 2.1: The fundamental principles of strain-rate hardening: (a) increase of the yield stress, (b) hardening with the increasing strain.

Initial studies regarding the strain-rate sensitivity of conventional metallic materials and alloys were performed in the first half of the 20th century [8–11]. Based on the experimental studies, the influence of the atomic arrangement, essential types of the strain-rate sensitivity and basic relations of the flow stress and strain-rate were identified and formulated [12–21]. It was shown, for a variety of materials, that the strain-rate related effects are very significant and have to be taken into account during the design of any structure subjected to dynamic loading [22–28]. Moreover, different mechanical properties and material models have to be adopted to reliably simulate the behavior of the material at high strain-rates using a numerical approach [29–31]. The drop-weight tower, the Hopkinson bar and the Taylor anvil techniques were found to be fundamental, well-defined and vital techniques for the investigation of materials during dynamic loading and impact [8, 11, 32, 33].

As the materials have become more complex and production methods have allowed the manufacturing of complex shapes and a complex internal structure of the material, an extensive and detailed investigation of the material properties at a variety of strain-rates is a key factor for the relevant design of the structure. Nowadays, an approach based on an experimental investigation combined with a numerical analysis is generally believed to be a very suitable technique for the production of optimized and functionally graded materials and structures [34–37].

2.2 Meta-materials

According to the basic definition, meta-materials can be described as materials that are engineered to exhibit properties that are either not found in naturally occurring materials [38]. Meta-materials can be divided into several sub-categories. Mechanical meta-materials are a special type of meta-materials with mechanical properties defined by their structure rather than their composition [39]. Mechanical meta-materials can exhibit non-standard or "negative" properties such as a negative Poisson's ratio (auxetics), negative longitudinal and volume compressibility [40], or can exhibit properties similar to a fluid (meta-fluid) [41]. Typical lattice structures of a mechanical meta-material is shown in Fig. 2.2.

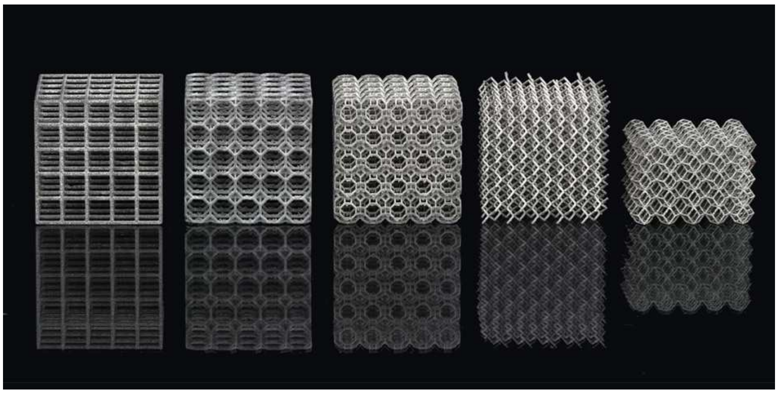

Figure 2.2: The typical lattice structures of mechanical cellular meta-materials [42].

2.3 Auxetic materials

Auxetic structures are meta-materials that possess a negative Poisson's ratio due to their internal structure and hence their deformation response to the applied loading is different from that of "standard" materials (or materials with positive Poisson's ratio). As a result, they expand in a transverse direction when loaded in tension and shrink when compressed (see Fig. 2.3). This behavior can be achieved artificially due to the special design of the internal structure, but examples of naturally occurring materials with the same property also exist, such as mineral rods, zeolites, silicates, and a few biological tissues [43]. An example of a material with a negative Poisson's ratio was described by Kolpakov [44] in 1985. The first cellular materials with a negative Poisson's ratio were designed and synthetized in 1987 by Lakes et al. [45] from conventional low-density open-cell polymer foams by tri-axial compression and the subsequent placing in a mold causing the ribs of each cell to permanently protrude inward. The word "auxetic", referring to material with a negative Poisson's ratio, was used by Evans [46] in 1991. With the advancement of material science and especially with the emergence of computer-aided design, together with additive manufacturing technologies, different structures with 2D and 3D auxetic behavior have been designed, produced, and tested [46–50]. Currently, there are generally eight types of common auxetic structures that can be classified as: (a) rigid node rotation, (b) chiral, (c) re-entrant lattice, (d) elastic instability, (e) kirigami fractal cut, (f) origami, (g) star shape connected, and (h) missing-rib [51, 52]. Design optimization and improvements of the deformation characteristics have been also investigated [53–55], including out-of-plane deformation characteristics and bending behavior [56, 57]. Owing to their specific properties, many interesting applications of auxetic materials have been described as potentially rendering use in different application areas, ranging from the medical (foldable devices, angioplasty, or esophageal stents) [58,59] to the automotive, aerospace, sport, or defense industries. Due to the possible increase in the strain energy absorption, special attention has been paid to the application of auxetic materials for energy absorption purposes during crash, blast, and other impact loadings [60–62]. Advancements in additive manufacturing and particularly the introduction of selective laser sintering/melting (SLS/SLM), powder metallurgy (PM) sintering, and pulsed electric current sintering

(PECS) enabled one to use metals as the base material for the production of structures [63]. This has broadened the application area of auxetic materials in impact protection devices [64], and increased the energy absorption capability through the possibility of using lighter and thinner components. These new technologies are still rather expensive, but with their increasing accessibility and the potential of their utilization in mass production leading to a reduction in the final price, the application of 3D printing in this area is expanding.

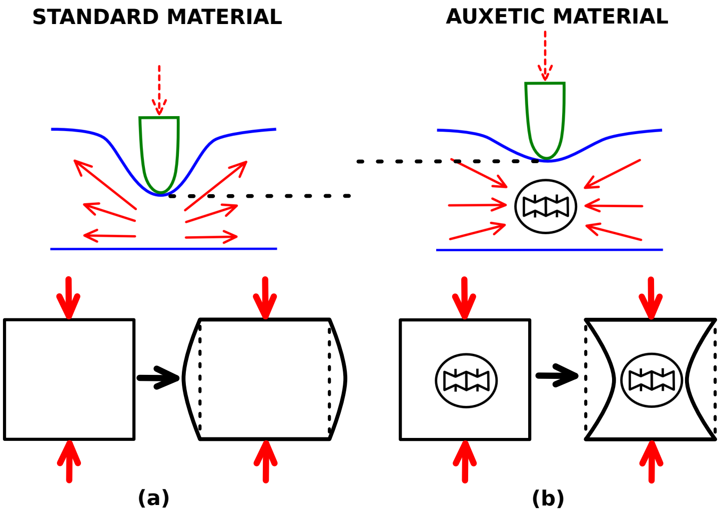

Figure 2.3: The principle of an auxetic material: (a) behavior of a standard material, (b) behavior of the auxetics.

2.4 Meta-materials impact testing and analysis

Regarding the issue of energy absorption, it is crucial to describe the deformation behavior of the structure under large deformations (i.e., a large overall compressive strain) properly. In the experimental investigation, it is necessary to reliably evaluate the strains during the experiment and assess the deformation modes taking the large displacements, large rotations, and contacts between the struts into account. This is crucial for the calibration or verification of the numerical models against the experimentally obtained data [65]. Nevertheless, outside the small-strain linear region, these characteristics must be evaluated experimentally due to their strong non-linearity [66]. Furthermore, the strain-rates and the velocities of the specific deformation processes have to be taken into account considering the expected applications of the auxetics, particularly the energy absorption of the high-speed impacts or blasts.

The deformation response of many homogeneous materials (i.e., ferrous alloys, copper, aluminum, etc.) is strain-rate dependent and significant variations between the quasi-static and the dynamic characteristics can be observed, including differences in low and high velocity impacts [67]. The difference of the dynamic behavior is further amplified in the case of cellular meta-materials due to the cellular nature of the constructs. The strain-rate dependency of the base material is then combined with the effects of the micro-inertia, localized heating, pore pressure, and others [68, 69]. Understanding these phenomena and the assessment of their influence on the effective properties of the auxetics can only be revealed experimentally under sufficient range of strain-rates to which the sample is subjected. Among the available methods, the single-stage powder gun has particularly been successfully used for the evaluation of the mechanical characteristics of auxetics [70]. Other experimental studies investigating the mechanical behavior of the auxetic structures under dynamic loading conditions, e.g., the crash behavior of a cylindrical tube with auxetic structures [71], the drop-weight impact characteristics [72], and the impact properties of an auxetic textile [73, 74] were also published. Studies analyzing auxetic structures under dynamic conditions using numerical simulations are also available [75–78].

Design optimization requires an in-depth investigation of the deformation behavior for the given specific loading conditions. Analytical, numerical and experimental studies investigating the re-entrant, chiral, cross-chiral, and other auxetic lattices under quasi-static loading have already been carried out [79–82]. The energy absorption and deformation behavior of tubes filled with auxetics have been studied by, e.g., Mohsenizadeh [83]. Papers dealing with the characteristics of auxetic materials subjected to dynamic loading are also available. Dynamic crushing of an open-cell polyurethane auxetic foam using an impact test was investigated by Scarpa and Lim [84–86]. Yang investigated auxetic sandwich panels using a quasi-static three-point bending test and a dynamic drop-weight impact test [87, 88]. Auxetic materials for sport safety applications were investigated by Duncan using a drop hammer impact test [89]. Both Scarpa and Duncan showed that auxetic foams can exhibit performance superior to conventional foams, e.g., in terms of damping properties, acoustic properties, and dynamic crushing [84, 89]. Generally, a key factor influencing the deformation behavior under dynamic loading is the strain-rate of the impact. For many materials, the mechanical behavior at various strain-rates can be significantly different. Mechanical properties based on quasi-static testing can produce misleading results and can significantly underestimate or overestimate the properties valid for the dynamic impact conditions [90]. Dynamic impact testing at high strain-rates is performed using specialized experimental apparatuses, especially SHPB.

2.5 Hopkinson bar testing

The Hopkinson bar method is an experimental technique for the measurement of the dynamic properties of materials at high strain-rates (approx. $1000 - 10000\,\mathrm{s}^{-1}$). It is based on the elastic strain wave propagation in slender bars. Currently, various arrangements exist for testing in compression, tension, torsion or bending [11,91–93]. The SHPB is a well-established variant of the Hopkinson bar for the dynamic testing of materials and can be used for evaluation of stress-strain curves at high strain-rates in compression. While the SHPB can be easily used for the measurements of ductile, high-strength materials, such as solid metals, its application on materials with a low mechanical impedance and geometrically complex inner structure is complicated and may lead to unreliable conclusions [94, 95]. Such measurements require the modification of the experimental setup. Moreover, advanced data correction techniques have to be applied for the proper evaluation of the mechanical properties [94,96]. Recently, a number of studies analyzing lattices [97], foams and honeycomb structures subjected to impact loading in SHPB have been published [98–100]. Strain rate sensitivity, inertia effects [98] and deformation behavior at high strain-rates [96] were investigated. A novel approach utilizing DIC techniques in SHPB experiments have also been introduced [101].

2.6 Digital image correlation in high-speed testing

DIC is a method for accurate measurements of changes in images (image registration technique). In material science and engineering, the method is often used for the evaluation of displacement and strain fields in a loaded specimen. DIC is a well established method for testing materials subjected to quasi-static conditions. However, in the case of high strain-rate loading, the method has to overcome several limitations, e.g., the lower resolution of the high-speed camera images, the illumination of the scene, and a low number of images in the image sequence resulting in large displacements between two subsequent images during the test [102]. However, the applicability of the method under dynamic conditions was shown in several studies [103–105]. In dynamic loading, some studies focused on materials with a microstructure used the DIC of high-speed camera images as a tool for the full-field analysis of the strain and other phenomena in the specimen [98, 101, 106] in the Hopkinson bar method.

2.7 State-of-the-art summary

Based on the state-of-the-art literature overview, the following conclusions can be drawn:

- The field of mechanical meta-materials is an extensively researched area with a lot of phenomena that are not fully described.
- Auxetics are materials exhibiting a negative Poisson's ratio with beneficial properties for the energy absorption applications.
- The Hopkinson bar method is a vital method for the experimental investigation of materials at high strain-rates. However, for the application on mechanical meta-materials, several limitations of the method have to be overcome.

- A few or no studies have been performed with auxetics subjected to impact loading at high strain-rates using Hopkinson bar.
- DIC is a suitable technique for the investigation of displacement and strain fields even during high strain-rate loading.

Chapter 3

Aim of the Ph.D. study

The main objectives of my Ph.D. work can be summarized by the following points:

1. The design of a Hopkinson bar experimental device for the testing of low impedance materials, particularly cellular meta-materials and auxetic lattices.
2. The development of an experimental methodology for the testing of cellular and auxetic materials using the developed Hopkinson bar experimental device.
3. Experiments with representative volume element (RVE) samples using the developed Hopkinson bar experimental device. The analysis of the Hopkinson bar experimental device performance and the limits of the strain-rate for the RVE samples.
4. Application of DIC for the analysis of strain and displacements in the specimen during the Hopkinson bar experiment.
5. Experiments with cellular meta-materials and auxetic materials using the developed Hopkinson bar experimental device.
6. The investigation of the deformation behavior of cellular meta-materials and auxetics subjected to dynamic compressive loading.

7. The evaluation of the experimental data that can be used as source data for the material model and for the numerical analyses of the structures using finite element method (FEM).

Chapter 4

Materials and Methods

In this chapter, an overview of the materials and methods used, adopted or developed during the study is summarized. The mechanical properties and deformation behavior of cellular meta-materials were investigated in compression using the Hopkinson bar method and evaluated using advanced methods, e.g., DIC. A detailed description of the tested materials, the design of the developed experimental setups, their performance, parameters, limitations or reasons for the selected physical arrangements and technical solutions is provided.

4.1 Mechanical meta-materials

A variety of mechanical meta-materials was investigated using several different Hopkinson bar setups. Two major types of materials were tested: (i) selective laser sintered auxetic lattices, (ii) hybrid foam and hybrid auxetic structures.

4.1.1 SLS auxetic lattices

Initial versions

Three different types of auxetic structures exhibiting an in-plane and volumetric negative strain-dependent Poisson's ratio were printed using a selective laser sintering (SLS) method in an AM 250 device (Renishaw, UK). The material used in the additive manufacturing printing process of the auxetic structures was the powdered 316L–0407 austenitic stainless steel alloy, which is comprised of iron alloyed with chromium of a mass fraction up to 18 %, nickel up to 14 %, and molybdenum up to 3 %, along with other minor elements. The alloy is an extra-low carbon variation on the standard 316L alloy. The density of the wrought material is $7990\,\mathrm{kgm^{-3}}$ and the melting point is in the range of $1371 - 1399\,°\mathrm{C}$. The mechanical properties of the sintered bulk material declared by the manufacturer are: a compressive strength in the horizontal direction of 662 MPa, in the vertical direction of 574 MPa; a yield strength in the horizontal direction of 518 MPa, in the vertical direction of 440 MPa, a modulus of elasticity in the horizontal direction of 167 GPa, in vertical direction of 134 GPa. The following auxetic structures were used in the study: a two dimensional missing rib, a two dimensional re-entrant honeycomb and a three-dimensional re-entrant honeycomb. The structures are shown in Fig. 4.1. The aforementioned types of structures were selected as they can be produced using SLS with satisfactory quality and a reasonable ratio between the overall dimensions (limited by the employed SHPB setup - see Section 4.5) and the number of unit cells in the structure. Moreover, they exhibit a significant development potential as their properties can be tuned by the optimization of the cell geometry. The missing rib specimen had dimensions of 11.7 × 12.0 × 13.0 mm and a nominal porosity 53.1 %. The 2D re-entrant had dimensions of 12.0 × 12.0 × 13.0 mm and a nominal porosity 52.3 %. The 3D inverted re-entrant had dimensions of 12.1 × 12.0 × 13.0 mm and a nominal porosity 74 %. All the structures had a nominal strut thickness of 0.6 mm. The overall dimensions of the samples were chosen to fit in the SHPB setup and, based on the SHPB performance (see Section 4.5), to reach the densification region during the impact experiment. The cross-section to specimen height ratio was approx. 1 and was selected to minimize the frictional and inertia effects in the SHPB experiment. In this first experimental campaign, the influence of the strain-rate sensitive filling on the constructs was also investigated. The samples were divided into three groups for the subsequent filling with the strain-rate sensitive material. The samples from the first group were filled using ordnance gelatin. The samples of the second group were filled with a porous low expansion polyurethane foam (Soudal, N.V., Belgium). This type of filling was selected due to its low specific weight and closed pore nature after curing, which contributes to the strain-rate sensitivity of this filling. More details about the application of the strain-rate sensitive filling, specimen preparation procedure and curing process can be found in our paper [1]. The following sample combinations were tested: (i) quasi-static, all the structures, 1+1+1 (unfilled + polyurethane filling + gelatin filling); (ii) SHPB, 2D re-entrant, 3+2+2; (iii) SHPB, 3D re-entrant, 2+2+2; (iv) SHPB, 2D missing rib, 3+2+2.

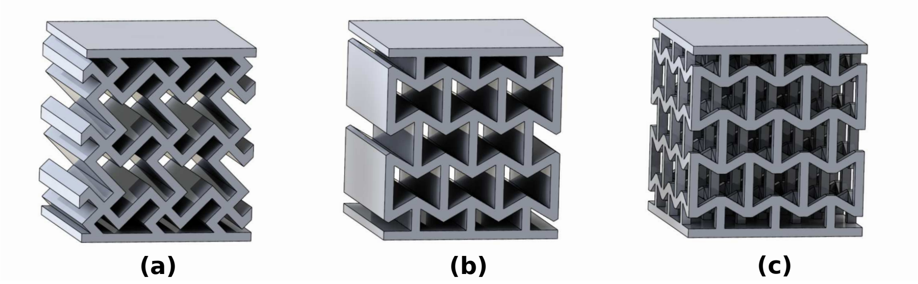

Figure 4.1: The SLS Auxetics - the initial version: (a) missing rib, (b) 2D re-entrant honeycomb, (c) 3D re-entrant honeycomb.

Optimized versions

After the initial experimental campaign, the design of the constructs was optimized and different versions of the auxetic lattices were produced using an identical printing machine and the material as in the previous paragraph.

Using the optimized printing process, it was possible to accommodate more auxetic cells within the specimen and manufacture thinner struts of the cells. The printed samples of the optimized structures are shown in Fig. 4.2. In contrast with the previous version, the geometry with a higher number of unit-cells in the cross-section of the produced samples was designed. This was achieved by changing the ratio of the characteristic unit-cell dimension to the overall specimen dimensions (constrained by the diameter of the bars used in the SHPB setup), i.e., the dimensions of the unit-cells were reduced to obtain at least 6 unit-cells in both directions of the specimen cross-section. This number was selected according to the general requirements on the RVE as defined by Gibson and Ashby et al. [107]. In relation to the decrease in the unit-cell dimensions, the nominal thickness of the individual struts within the microstructure was also reduced down to approx. 0.3 mm. The overall dimensions of the samples were 12.2 × 12.2 × 12.6 mm and, thus, were tailored to the dimensions and performance of the SHPB setup, which ensured reaching the densification region of the materials response during the impact experiments. The missing-rib specimens were composed of 36 unit-cells in a 6 × 6 arrangement at a nominal porosity of 74.4 %, the two-dimensional re-entrant honeycomb specimens were composed of 42 unit-cells in a 6 × 7 arrangement at a nominal porosity of 73.4 %, and the three-dimensional re-entrant honeycomb specimens were composed of 252 unit-cells in 6 × 6 × 7 arrangement at a nominal porosity of 72.4 %. The production of such samples was at the resolution limit of the used SLS device as the treatment of the heat dissipation brought serious challenges to tuning the manufacturing procedure in order to avoid the collapse of the specimens during printing. For each type of microarchitecture, three specimens were used during the quasi-static experiments and five specimens for each strain-rate during the Hopkinson

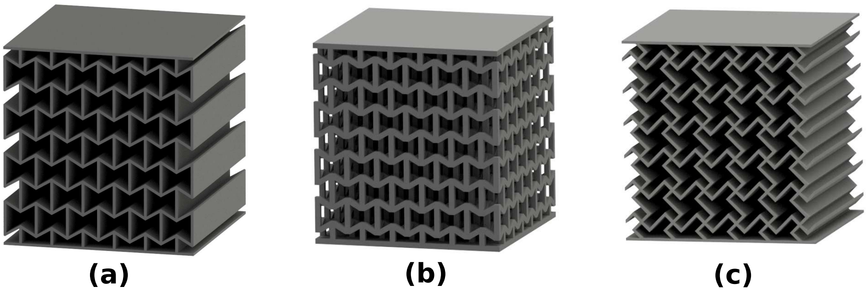

Figure 4.2: The SLS Auxetics - the optimized version: (a) 2D re-entrant honeycomb, (b) 3D re-entrant honeycomb, (c) missing rib.

bar dynamic testing. Hence, 23 samples of each microstructure were tested and evaluated yielding 69 tested samples in total. The SEM inspection of the printed lattices was performed showing that imperfections occur primarily on the surface of the specimen with the magnitude of twice the size of the powder particles of the printing material. This is, in this case, approximately $2 \times 50\,\mu$m. The resulting surface quality affects the ability of the SLS printing to reproduce the sharp edges and corners designed in the microstructure, where, particularly, sharp corners are printed as filleted connections with a radius equivalent to the surface roughness.

4.1.2 Hybrid foam

Metal foams can be manufactured in different ways, starting from a molten metal, a solid powder, in the state of a vapor or from a metal ion solution [108]. In the context of this study, the investigated foams, were fabricated by an electro-chemical coating process [109]. The basic framework for the Ni/PU foams (nickel-polyurethane hybrid foams) is an open-cell polyurethane foam (Schaumstos Direkt Rudiger Nolte, Enger, Germany) with an average pore size of 20 ppi (pores per inch) and a density of $0.022\,\mathrm{gcm}^{-3}$. The PU template structure was cut into two different sets of specimens. Both sets have a cylindrical shape of 20 mm in diameter, but with different heights of 10 mm and 20 mm, respectively. After the coating process, the coating thickness of both sets of specimens was determined to be $150\,\mu$m. Due to fluctuations in the conductivity, some small scattering regarding the macroscopic density and, therefore, the real coating thickness occurred. The specimens of the hybrid foam are shown in Fig. 4.3.

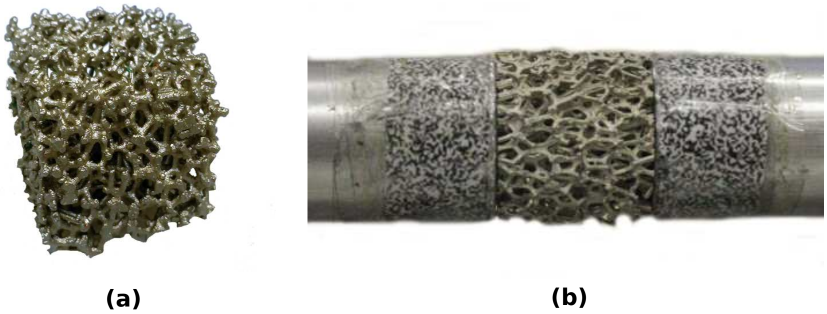
(a)

(b)

Figure 4.3: The tested hybrid foam: (a) hybrid foam specimen, (b) specimen mounted in the Hopkinson bar.

4.1.3 Hybrid auxetic structures

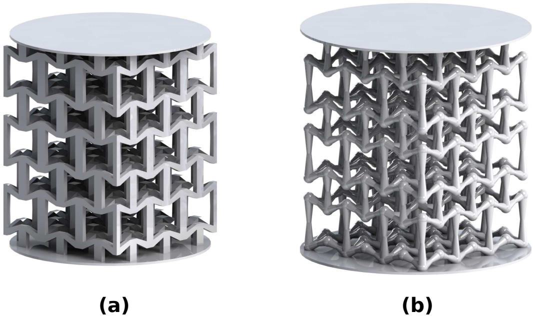

Figure 4.4: The hybrid auxetic structures - the render: (a) 3D re-entrant with rectangular cross-section of the struts, (a) 3D re-entrant with circular cross-section of the struts.

The geometry of the samples was based on a periodical assembly of 3 × 3 × 3 re-entrant honeycomb auxetic unit cells. Two different types of structures with 25 samples per structure were manufactured. The first structure consisted of struts with a circular cross section, and the second structure had struts with a rectangular cross-section. The 3D renders of both types of specimens are

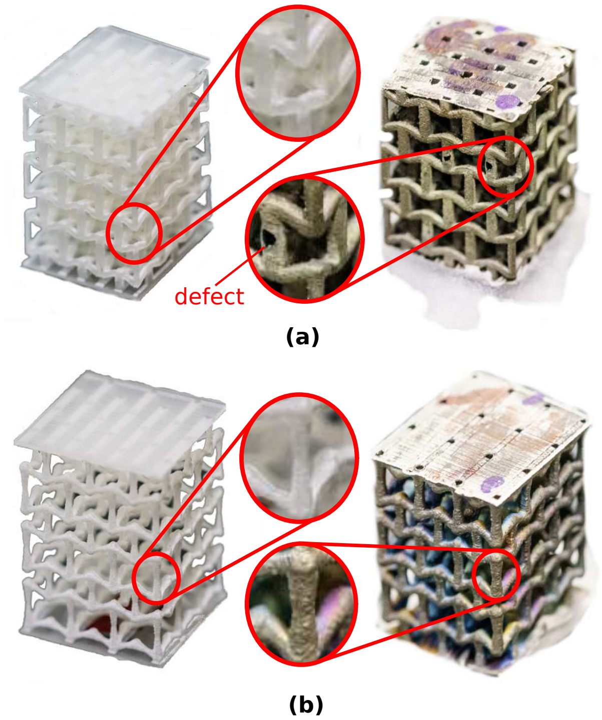

Figure 4.5: The printed and coated hybrid auxetic constructs

shown in Fig. 4.4. The specimens were printed using a Pro Jet HD3000 3D printer (3D Systems, Rock Hill, USA) from a UV-curable polymer VisiJet EX200 with the highest resolution ($656 \times 656 \times 800\,\text{dpi}$). The overall sample dimensions of the rectangular specimens were approximately $12.5 \times 12.5 \times 18.4\,\text{mm}$ and the circular specimens were approximately $13.7 \times 13.7 \times 19.5\,\text{mm}$. The selected polymeric samples were electro-chemically coated with a $\approx 60\,\mu\text{m}$ and $\approx 120\,\mu\text{m}$ thick layer of nickel, respectively. Further information on the coating process can be found in Jung et al. [110]. After the coating process, the polymer was taken out via pyrolysis at about 1000 °C. The printed polymeric constructs as well as the final hybrid coated hollow-strut auxetic structures are shown in Fig. 4.5.

4.2 SHPB principle

SHPB is an experimental technique for the investigation of the mechanical properties of materials at high strain-rates. The nominal achievable strain-rate of the method is in range of $1000 - 10000\,\mathrm{s}^{-1}$. The main principle of the method is based on an elastic strain wave propagation in a set of co-axial slender bars. In the conventional arrangement, the SHPB setup consists of three co-axial bars: (i) a striker bar, (ii) an incident bar, and (iii) a transmission bar. The striker bar is mounted in a system that can accelerate it (e.g., a gas-gun) or set it with a preload, while the tested specimen is mounted between the incident and the transmission bar. When the striker impacts the incident bar (or when its preload is released), a compression elastic strain-wave is developed in the incident bar. The elastic strain wave propagates through the incident bar until it impacts the interface between the bar and the specimen. On the boundary of the specimen, a part of the incident wave is reflected back in the incident bar while a part of the incident wave passes through the specimen compressing it. On the opposite boundary of the specimen, the wave transmits to the transmission bar. The transmission bar then impacts a momentum trap that absorbs the residual energy of the experiment. During the experiment, the three waves (incident, reflected, transmission) propagating in the bars are measured using the strain-gauges mounted on the surface of the bars. The analysis of the waves allows for the evaluation of the stress-strain diagrams as well as the strain-rate diagrams of the tested material (see Section 4.2.1). The fundamental principle of the SHPB is shown in Fig. 4.6. In the case of this study, an SHPB apparatus with a striker bar accelerated using a gas-gun was developed and optimized for the testing of cellular meta-materials. In its initial version, the setup was based on the classical design introduced by Kolsky [11] in 1949.

4.2.1 1-D elastic strain wave propagation

One-dimensional wave propagation theory is the simplest theory for the evaluation of the SHPB experiment. It is based on the assumption that the elastic strain waves in the bars propagate at a constant velocity without any

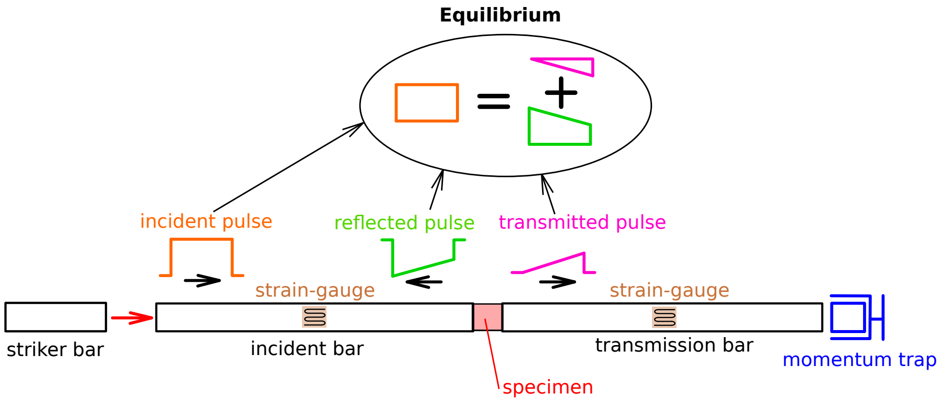

Figure 4.6: The fundamental principle of the SHPB method.

attenuation and their nature is non-dispersive. Moreover, the theory is valid only when the so-called dynamic force equilibrium is achieved, and neglects the effects related to the inertia and friction. Dynamic force equilibrium is a state when the forces in the specimen are equal to the forces on the respected faces of the bars. In the following text, it is assumed, for simplicity, that the diameters and material properties of all the bars in the setup are identical. If this assumption is not valid, the respected formulas can be modified to reflect the parameters of the actual setup. According to the one-dimensional wave propagation theory, the stress distribution in the specimen in the dynamic equilibrium state is uniform and, thus, the forces, stresses, and strains can be calculated based on the fundamental relationship between the strain waves

$$\epsilon_{\mathrm{I}} + \epsilon_{\mathrm{R}} = \epsilon_{\mathrm{T}}, \tag{4.1}$$

where ϵ_{I}, ϵ_{R}, ϵ_{T} refer to the incident, reflected and transmitted strain pulses measured by the strain-gauges. The nominal strain-rate in the specimen $\dot{\epsilon}_{\mathrm{s}}$ can be then expressed using the wave propagation velocity in the bar c_0 and the initial specimen length l_0

$$\dot{\epsilon}_{\mathrm{s}}(t) = -\frac{2 \cdot c_0}{l_0} \cdot \epsilon_{\mathrm{R}}(t). \tag{4.2}$$

Using integration of the nominal strain-rate, one can evaluate the nominal strain of the specimen by

$$\epsilon_{\mathrm{s}}(t) = \int_0^t \dot{\epsilon}_{\mathrm{s}}(t)\mathrm{d}t. \tag{4.3}$$

The average nominal stress in the specimen can be calculated from the measured transmission pulse using

$$\sigma_{\mathrm{s,T}}(t) = \frac{E_{\mathrm{b}} \cdot A_{\mathrm{b}}}{A_{\mathrm{s}}} \cdot \epsilon_{\mathrm{T}}(t), \tag{4.4}$$

where E_{b} is the Young's modulus of the bar, A_{b} is the cross-sectional area of the bar, and A_{s} is the cross-sectional area of the specimen. To analyze the dynamic equilibrium in the specimen, the stress in the specimen is evaluated from the incident bar pulses

$$\sigma_{\mathrm{s,I}}(t) = \frac{E_{\mathrm{b}} \cdot A_{\mathrm{b}}}{A_{\mathrm{s}}} \cdot \left[\epsilon_{\mathrm{I}}(t) + \epsilon_{\mathrm{R}}(t)\right]. \tag{4.5}$$

The dynamic equilibrium state is achieved when the stress in the specimen $\sigma_{\mathrm{s,I}}(t)$ evaluated from the incident bar converges with the average stress $\sigma_{\mathrm{s,T}}(t)$ calculated from the transmission bar. Detailed information about the 1D wave propagation theory is given in the literature [11, 32].

Real strain wave propagation in SHPB

In the real SHPB experimental setup, the aforementioned theoretical assumptions and equations are affected by a number of effects. In reality, strain wave propagation has a dispersive character. The wave dispersion is caused by the fact that the wave propagation velocity is not constant for the whole frequency spectrum [32, 111] of the strain pulse. In principle, higher frequencies propagate (commonly) with lower velocities and, because of the Poisson's ratio effects, higher frequencies also have higher attenuation. Thus, with the increasing distance from the impacted face of the bar, more dispersion related to the Pochhammer-Chree oscillations [111] are observed in the strain pulse. Moreover, the material of the bars can exhibit visco-elastic behavior with significant wave attenuation and wave shape changes that cannot be simply neglected. In this case, advanced methods of the setup calibration and the time shifting of the measured waves have to be employed [112–118] (see Section 4.7.3).

The amplitude of the incident strain pulse in the classical Hopkinson bar experiment is proportional to the impact velocity of the striker bar v_{st} according to the relation

$$\epsilon_{\mathrm{I}} = \frac{v_{\mathrm{st}}}{2 \cdot c_0}, \tag{4.6}$$

and the wavelength of the pulse l_{p} is double the length of the striker l_{st}

$$l_{\mathrm{p}} = 2 \cdot l_{\mathrm{st}}. \tag{4.7}$$

Therefore, in the conventional Kolsky setup, the length of the bars should be at least double the length of the striker bar with a strain-gauge measurement point in the middle of the bar. This arrangement is used to prevent the superposition of the forward-propagating incident pulse with the backward-propagating reflected pulse. However, in reality, the ramp-in sections of the pulses are always longer - requiring longer bars. Moreover, the use of any wave shaping technique (method for changing the shape of the strain wave by, e.g., plastic deformation of the soft material, see Section 4.7.5) usually increases the wavelength of the pulse. As the traveled distance through the very long bars negatively affects the precision of the measurement, more advanced methods for the wave decomposition and analysis have to be employed when long striker bars are used. Note that the maximum strain in the specimen is dependent on both the striker impact velocity as well as on the pulse duration.

These parameters have to be carefully tuned to get the required performance and outcome of the experiment.

Friction effects on the interface of the specimen with the bar and the inertia of the specimen can also play an important role. The recommended length to diameter (cross-section) ratio of the specimen should be used to minimize these effects and hold applicable the one-dimensional strain wave propagation theory. Further reading regarding the effects affecting the validity of the one-dimensional strain wave propagation theory can be found in the literature [32].

4.3 SHPB and low impedance materials

Although the SHPB is a well established method for the testing of bulk materials with relatively high mechanical impedance, it has a number of serious limitations for testing low impedance (soft) materials. In a simplified view, high impedance materials, well suitable for the SHPB method, produce high transmission signals, have high wave propagation velocities with low attenuation of the strain wave and are able to deform plastically up to considerably high strains [32]. It can be demonstrated that the time required to achieve steady dynamic equilibrium is equal to π reflections of the strain wave in the specimen [32]. Thus, the required time is proportional to the wave propagation velocity in the specimen. The wave propagation velocity is dependent, not only on the material of the specimen, but also on many other parameters like the dimensions, geometry and shape of the specimen [11, 32]. Moreover, the time necessary to achieve dynamic equilibrium is also dependent on other factors, e.g., the quality of the contact between the specimen and the bars, impedance mismatch between the specimen and bars [32], or applied shaping method of the incident pulse. The low amplitude of the transmission signal, in the case of the low impedance specimen, is also a problem as the signal-to-noise ratio of the measured transmission strain wave is very low. In the worst case, the transmission signal can be even hidden in the noise of the strain-gauge circuitry or severely attenuated and distorted by its travel from the specimen to the measurement point. Testing the low impedance materials requires a set of modifications to the experimental setup to overcome the aforementioned problems [119, 120].

- The position of the measurement sensors should be as close to the specimen as possible and the wave superposition effects have to be taken into account.
- Direct measurement of the force on the specimen boundaries using the embedded high frequency bandwidth load-cell (e.g., piezoelectric force sensor) should be used for the evaluation of the specimen's response. However, in this case, the calibration of the setup is required to know the wave propagation characteristics through the sensors.
- The specimen length should be reduced to a minimum to reduce the wave travel time as much as possible. This should be done even with the violation of the length to diameter ratio that is recommended to minimize the friction and inertia effects during the experiment.
- The specimen diameter should be maximized to maximize the impedance of the specimen and to achieve as high amplitude of the transmission signal as possible.
- The pulse-shaping technique should be used to prolong the ramp-in period of the incident pulse and to better tune the incident wave shape with the response of the specimen. The pulse-shaping technique is based on the mounting of a small piece of a soft material (pulse-shaper) on the impact face on the incident bar [121, 122]. During the impact of the striker bar on the incident bar, the pulse-shaper modifies the base shape of the strain wave (theoretically, a rectangular pulse) to a more smoothed shape and serves as a high-frequency filter for the reduction of the Pochhammer-Chree oscillations.
- The strain wave amplitude should be proportionally optimized for the impedance of the actual specimen.

4.3.1 SHPB and cellular materials

Unfortunately, many of the solutions, approaches and recommendations summarized in the aforementioned section cannot be adopted for the testing of cellular materials in the SHPB as the requirements for the cellular materials are contradictory to the general rules for the testing of low impedance materials. The main problems can be summarized in the following points:

- Application of the direct force measurement sensors is very limited as high impact velocities of the striker are usually required to compress the specimen to the required strain with a reasonably long striker. High strain waves amplitudes require sensors with a sufficient load capacity to withstand the high stresses in the system and with a sufficient mechanical impedance not to produce any unwanted wave reflections. With the increasing load capacity, the precision of the load-cell decreases to the values comparable with the strain-gauges.
- The length of the specimen cannot be minimized to reduce the wave travel time as the specimen has to contain a certain number of layers (pores) for the relevant testing.
- The strain wave amplitude cannot be optimized for the impedance of the actual specimen as it would result in a very low compressive strain in the specimen or would require a very long striker bar.

4.3.2 Selected approach for the testing using SHPB

In the thesis, the following approach was selected to overcome the problems with the cellular and low impedance nature of the tested specimens:

- A high-strength aluminum alloy was used as the material of the bars (higher strain signals in comparison to steel).

- Visco-elastic polymethyl metacrylate (PMMA) bars were used as the material of the bars for the testing of very low impedance materials.
- The length of the striker was optimized to achieve the requested strain at a given strain-rate.
- A gas-gun with long barrel and high pressure capacity was used for the acceleration of the long striker to the high impact velocities (high relatively in terms of the SHPB method).
- The specimen dimensions and stiffness were optimized to achieve an acceptable trade-off between the maximum strain, strain-rate, strain wave amplitudes, inertia, friction effects and producibility.
- The pulse-shaping technique was employed for the modification of the incident pulse to filter-out the Pochhammer-Chree dispersion related oscillations and to shape the strain wave for a better fit with the specimen and for the dynamic equilibrium with better quality.
- Noise reduction techniques and careful pre-processing of the signals from the strain-gauges were employed for the high precision measurement data.
- Advanced methods for the setup calibration were introduced.
- An evaluation using the multi-point measurement of the strain waves was applied for the higher precision and relevancy of the results.
- An optical inspection of the experiments using high-speed camera imaging was performed in all the experiments.
- An advanced analysis and verification of the measured signals with the DIC were used in the evaluation of the results.

4.4 Simple analytical model of the gas-gun and SHPB

Based on the aforementioned assumptions, a simple analytical model for the prediction of the experiment output was created with the given experimental setup parameters [2]. The model is based on the previously published relations related to the gas-gun design [123–125] and the Hopkinson bar theory [11,126]. The existing models are used to derive a modified solution for our design, in which the SHPB striker is propelled using compressed air. The model can be used inversely also for the calculation of the required SHPB gas-gun performance needed for the desired strain and strain-rate values in the specimen.

The literature-based analytical model of the gas-gun [123–125] working according to the adiabatic process with drag effects, and the analytical model of the SHPB based on linear one-dimensional wave propagation theory in cylindrical slender bars [11, 126] (see Section 4.2.1) were used as the basis for the derivation of the presented model.

4.4.1 Model definition

The nomenclature used in the description of the model is summarized in Tab. 4.1. Based on the adiabatic model of the gas-gun, the following equation can be used for the calculation of the striker impact velocity including the drag effects represented by the pressure loss coefficient C_P and by the striker bar friction force F_f,

$$v_\mathrm{st} = \sqrt{\frac{2}{m_\mathrm{st}}\left\{\frac{C_\mathrm{P}\cdot P\cdot V}{\gamma-1}\left[1-\left(\frac{V}{A_\mathrm{st}\cdot l_{\mathrm{br}_\mathrm{ef}}+V}\right)^{(\gamma-1)}\right]-F_\mathrm{f}\cdot l_{\mathrm{br}_\mathrm{ef}}\right\}}. \tag{4.8}$$

P	gas-gun pressure
l_{st}	striker bar length
l_{sp}	specimen length
$A_{[\mathrm{sp,st,in,tr}]}$	cross-section area (sp - specimen, st - striker bar, in - incident bar, tr - transmission bar)
σ_{sp}	effective stress in the specimen (ideal plastic material model)
E	Young's modulus of the bars
ρ	density of the bars and the striker
c_0	nominal wave velocity in the bars ($\sqrt{E/\rho}$ for an ideal linear elastic material)
l_{br}	barrel length
C_{P}	pressure loss coefficient $C_{\mathrm{P}} \in \langle 0; 1 \rangle$
C_{f}	friction coefficient $C_{\mathrm{f}} \geq 0$
V	volume of the gas-gun reservoir
γ	specific heat ratio ($\frac{7}{8}$ for the compressed air gas-gun)
m_{st}	mass of the striker bar
β	geometrical relation of the striker and the incident bar $\left(\beta = \dfrac{A_{\mathrm{st}}}{A_{\mathrm{in}}}\right)$
$l_{\mathrm{br_{ef}}}$	barrel effective length ($l_{\mathrm{br_{ef}}} = l_{\mathrm{br}} - l_{\mathrm{st}}$)
F_{f}	friction force ($F_{\mathrm{f}} = m_{\mathrm{st}} \cdot \mathrm{g} \cdot C_{\mathrm{f}}$)
t_{ps}	pulse duration
l_{ps}	pulse length
v_{st}	striker impact velocity
$\dot{\epsilon}_{\mathrm{sp}}$	specimen strain-rate
ϵ_{sp}	maximum strain in the specimen
g	gravitational acceleration constant
$\sigma_{[\mathrm{in,ref,tr,st}]}$	stress (in - incident pulse, ref - reflected pulse, tr - transmission pulse, st - striker bar)
$\epsilon_{[\mathrm{in,ref}]}$	pulse amplitude (in - incident pulse, ref - reflected pulse)

Table 4.1: The gas-gun and SHPB model nomenclature

From the value of the striker bar velocity v_{st}, the nominal strain-rate in the specimen can be determined according to the relation

$$\dot{\epsilon}_{\mathrm{sp}} = \frac{2c_0 \cdot (v_{\mathrm{st}} \cdot A_{\mathrm{in}} \cdot \rho \cdot c_0 \cdot \beta - A_{\mathrm{sp}} \cdot \sigma_{\mathrm{sp}} - A_{\mathrm{sp}} \cdot \sigma_{\mathrm{sp}} \cdot \beta)}{A_{\mathrm{in}} \cdot E \cdot l_{\mathrm{sp}}\,(1+\beta)}. \tag{4.9}$$

The parameters of the initial incident pulse and stresses in the bars and the striker can be derived from the one-dimensional wave propagation theory according to

$$\begin{aligned}
l_{\mathrm{ps}} &= 2l_{\mathrm{st}}, && (4.10)\\
t_{\mathrm{ps}} &= \frac{2l_{\mathrm{st}}}{c_0}, && (4.11)\\
\sigma_{\mathrm{in}} &= \frac{A_{\mathrm{sp}}}{A_{\mathrm{in}}} \cdot \sigma_{\mathrm{sp}} + \frac{E \cdot l_{\mathrm{sp}}}{2c_0} \cdot \dot{\epsilon}_{\mathrm{sp}}, && (4.12)\\
\sigma_{\mathrm{ref}} &= -\frac{E \cdot l_{\mathrm{sp}}}{2c_0} \cdot \dot{\epsilon}_{\mathrm{sp}}, && (4.13)\\
\sigma_{\mathrm{tr}} &= \frac{A_{\mathrm{sp}}}{A_{\mathrm{tr}}} \cdot \sigma_{\mathrm{sp}}, && (4.14)\\
\sigma_{\mathrm{st}} &= \frac{\rho \cdot c_0 \cdot v_{\mathrm{st}}}{1+\beta}. && (4.15)\\
& && (4.16)
\end{aligned}$$

The strain amplitudes of the pulses in the incident bar and the maximum strain in the specimen can be derived from the aforementioned equations yielding

$$\begin{aligned}
\epsilon_{\mathrm{in}} &= \frac{v_{\mathrm{st}}}{2c_0}, && (4.17)\\
\epsilon_{\mathrm{ref}} &= -\frac{\dot{\epsilon}_{\mathrm{sp}} \cdot l_{\mathrm{sp}}}{2c_0}, && (4.18)\\
\epsilon_{\mathrm{sp}} &= -\frac{2l_{\mathrm{ps}} \cdot \epsilon_{\mathrm{ref}}}{l_{\mathrm{sp}}}. && (4.19)
\end{aligned}$$

4.4.2 Comparison of the model with experimental results

To show the quality and applicability of the model, a comparison between the results predicted by the model and the actual results of the selected real experiments are shown in the following paragraphs. The predicted values calculated using this analytical model were compared with the measured values for the experiments conducted with the two types of bars (aluminum and PMMA) at the different strain-rates. Note that the model was used, not only in the design phase of our SHPB setup, but also has been used to estimate the output of the experiments. Thus, the following results were produced during the whole period of the work on the study and are shown here for demonstrative purposes only.

Experimental setup

The model was used for the prediction of the output of the real experiments carried out in the laboratory. The results of the model were compared with the measured values. A modified Kolsky SHPB setup was used for the experiments with both high-strength aluminum alloy bars (EN-AW-7075-T6) and the PMMA bars at two different impact velocities (see Section 4.5). In all the experiments, the measurement bars with a nominal diameter of 20 mm and length of 1600 mm were used.

Gas-gun muzzle velocity measurement

The muzzle velocity of the gas-gun was experimentally measured using photo-electric sensors mounted at the end of the gas-gun barrel (see Section 4.5). The calculated and measured muzzle velocity of the aluminum alloy striker with a length of 300 mm accelerated using the reservoir pressure of $0.1-0.6$ MPa is shown in Fig. 4.7. In the analytical model, no pressure losses and friction were used as these effects were experimentally found to be negligible for the used striker material and the reservoir pressures. The results of the impact velocity calculated by the model are in very good agreement with the measured values (see Fig. 4.7).

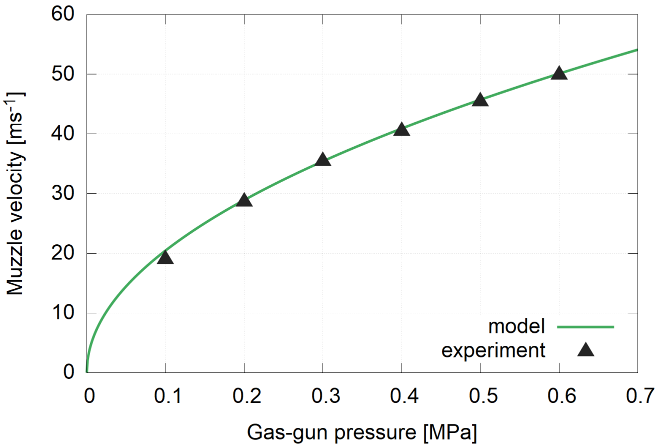

Figure 4.7: The gas-gun muzzle velocity - a comparison of the model and the experiment.

Elastic bars - aluminum alloy

An additively manufactured 2D re-entrant auxetic lattice (see Section 4.1.1) is presented here as an example of the model functionality for the linear-elastic aluminum alloy bars at two different impact velocities. It was experimentally proven that, in case of the aluminum alloy bars, it is not necessary to take friction and pressure losses into account as the effects can be considered negligible in the used velocity range. Two different stresses σ_{sp} for the ideal plastic model of the specimen were used as a strain-rate sensitivity effect was expected based on the previous experiments. The comparison of the results of the model and the experiment is summarized in Tab. 4.2. The values predicted by the model are in very good agreement with the measured values.

	$P = 0.1\,\mathrm{MPa}$			$P = 0.8\,\mathrm{MPa}$		
	mod.	exp.	rel. diff.	mod.	exp.	rel. diff.
v_{st} [ms^{-1}]	21.73	20.95	4 %	43.45	42.64	2 %
ϵ_{sp} [$-$]	0.28	0.27	4 %	0.61	0.52	17 %
$\dot{\epsilon}_{\mathrm{sp}}$ [s^{-1}]	1436	1374	5 %	3135	3015	4 %
ϵ_{in} [$\mu\epsilon$]	2104	2122	1 %	4208	4311	2 %

Table 4.2: The comparison of the experiment output estimated by the model with the values measured in the experiment - the SHPB aluminum bars. The specimen - the auxetic 2D re-entrant. Model parameters: $\sigma_{\mathrm{sp}} = 60\,\mathrm{MPa}$ (low pressure), $\sigma_{\mathrm{sp}} = 75\,\mathrm{MPa}$ (high pressure), $C_{\mathrm{P}} = 1$, $C_{\mathrm{f}} = 0$.

Visco-elastic bars - PMMA

A specimen of ordnance gelatin is presented as an example of the model functionality for the visco-elastic PMMA bars at two different impact velocities. The attenuation and dispersion effects were corrected in the model using two different pressure loss coefficients C_P based on the wave propagation functions for the PMMA. Two different stresses σ_sp for the ideal plastic model of the specimen were used as a strain-rate sensitivity effect was expected based on the previous results. The comparison of the results of the model and the experiment is summarized in Tab. 4.3. The values predicted by the model are in very good agreement with the measured values.

	$P = 0.1\,\mathrm{MPa}$			$P = 0.8\,\mathrm{MPa}$		
	mod.	exp.	rel. diff.	mod.	exp.	rel. diff.
v_st $[\mathrm{ms}^{-1}]$	11.11	11.72	5 %	21.91	24.51	11 %
ϵ_sp $[-]$	0.37	0.37	0 %	0.67	0.65	3 %
$\dot{\epsilon}_\mathrm{sp}$ $[\mathrm{s}^{-1}]$	1985	2084	5 %	3767	3926	4 %
ϵ_in $[\mu\epsilon]$	2585	2847	9 %	5097	5231	3 %

Table 4.3: The comparison of the experiment output estimated by the model with the values measured in the experiment - the SHPB PMMA bars. The specimen - the ordnance gelatin. Model parameters: $\sigma_\mathrm{sp} = 0.3\,\mathrm{MPa}$ (low pressure), $\sigma_\mathrm{sp} = 4\,\mathrm{MPa}$ (high pressure), $C_\mathrm{P} = 0.9$ (low pressure), $C_\mathrm{P} = 0.8$ (high pressure), $C_\mathrm{f} = 0$.

4.4.3 Model summary

The model allows for the calculation with the elementary drag effects or with a simple correction of the wave dispersion effects in the bars. The model functionality was evaluated on the real SHPB experiments carried out with both the linear-elastic and visco-elastic bars at two different impact velocities. In all the cases, the model predicted values were close to the output of the real experiments. The presented model can be used as a simple tool for the prediction of the SHPB experiment output or, inversely, as a tool for designing an SHPB with a required performance.

4.5 Design of the SHPB

In the following paragraphs, the design of our SHPB setup is described. An overview of the general arrangement, technical solutions adopted in the setup and the detailed technical description is summarized in the text. Note that the design is always a trade-off between many design parameters that are often contradictory to each other. Therefore, the setup was modified, optimized or tailored better for the desired application several times during the study. When important, the development stages are discussed in the study. Otherwise, the latest (and the most advanced - after 5 years of development) version of the setup is described in the text.

4.5.1 General arrangement

The conventional arrangement with three bars (striker bar, incident bar, transmission bar) and a momentum trap was selected as the setup suitable for testing cellular meta-materials. The acceleration of the striker is provided using a gas-gun. The gas-gun was designed with a long barrel to get high impact velocities of the striker and, thus, to achieve a representative strain (sufficiently high - in the ideal case, up to the densification of the structure) in the cellular specimens. For simplicity, all the bars were selected to have a cylindrical shape of the same diameter, to be manufactured with the same material and to be mounted co-axially in the setup. A high performance aluminum alloy was selected as the material for the bars as it has a relatively low mechanical impedance in comparison with other materials such as steel or titanium alloys. Magnesium alloys, with even lower mechanical impedance, were also considered as a material suitable for the application. However, this material was not selected because of its low yield strength (in comparison with the high-performance aluminum alloy), complications in machining and a high cost.

Analyzing the results of the representative volume element (RVE) for similar cellular specimens [63, 127] and the estimated performance of the setup, the diameter of the bars was initially constrained to 20 mm. This value was accepted as a reasonable trade-off between the size of the specimen, the achievable strain and strain-rate, the complexity of the setup and the manufacturing cost of the specimens. During the finalization period of this thesis, a modular upgrade to fit-in bars with a diameter of up to 40 mm is currently finishing.

According to the design calculations, dimensions and expected properties of the specimens, the setup has to be able to accelerate a striker with a length of 500 mm up to the maximal impact velocity of around 50 $\mathrm{ms^{-1}}$. Thus, the required length of the bars is approx. 1500 mm and the residual kinetic energy can be as high as approx. 2000 J.

4.5.2 Technical description

The SHPB setup was designed as the assembly of a modular frame accommodating the gas-gun apparatus, measurement bars and the damping elements. The overall length of the default arrangement is approx. 7000 mm, however, due to its modular design, it can be easily extended up to the required length (limited by the size of the room, currently approx. 15000 mm). Commonly, high performance aluminum alloy EN-AW-7075-T6 or PMMA are used as the materials for the bars. All the technical documentation and drawings of the

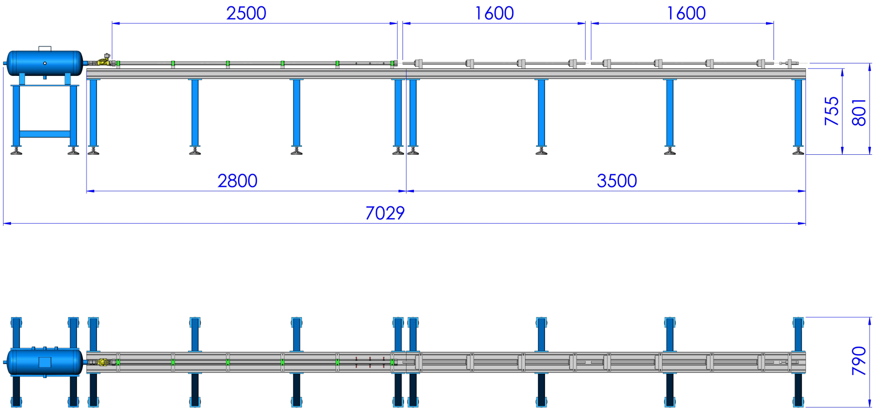

Figure 4.8: The SHPB setup dimensional drawing.

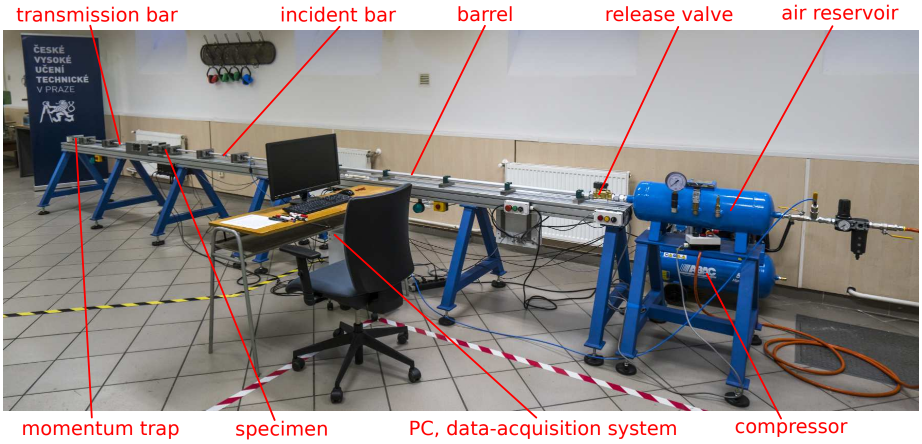

Figure 4.9: The overview of the SHPB setup.

SHPB setup are included as an attachment to this thesis (see Appendix B). The dimensional drawing of the setup is shown in Fig. 4.8. The overview of the setup is shown in Fig. 4.9.

Frame

The modular frame consists of an aluminum alloy profile with a cross-sectional dimension of 180 mm × 90 mm mounted on adjustable steel supports. The aluminum profile is used for the mounting of all the other parts of the setup, e.g., the gas-gun barrel, damping elements, etc. In the default arrangement, the setup is mounted on two aluminum profiles (length of 2800 mm and 3500 mm) that are screwed together using specialized interconnection elements.

Gas-gun

The gas-gun system consists of a compressed air reservoir with a volume of 20 l, a steel barrel with an internal diameter of 20 mm, an external diameter of 40 mm and a length of 2500 mm, control valves, safety elements and accessories. Five valves are connected to the reservoir: (i) a manually operated intake valve (type BVG4-1/2L, Parker, USA), (ii) a fast-release valve (type 366531, Parker, USA), (iii) an emergency over-pressure draining valve (integrated in the air reservoir), (iv) an automatic safety draining valve (type 362720, Parker, USA), and (v) a manually operated draining valve (type 04910717, Parker, USA). The fast-release valve is directly operated in the electro-mechanical part that serves as the trigger of the gas-gun. It has a 1 inch bore and is directly and co-axially connected with the barrel to ensure a high through-flow of the air and transfer efficiency, that are crucial parameters for the gas-gun performance. The barrel is mounted and adjusted on the frame using universal tube clamps. All the parts of the gas-gun system are designed for the maximum pressure of 1.6 MPa. The gas-gun can accelerate the strikers made of different materials. The gas-gun system is shown in Fig. 4.10.

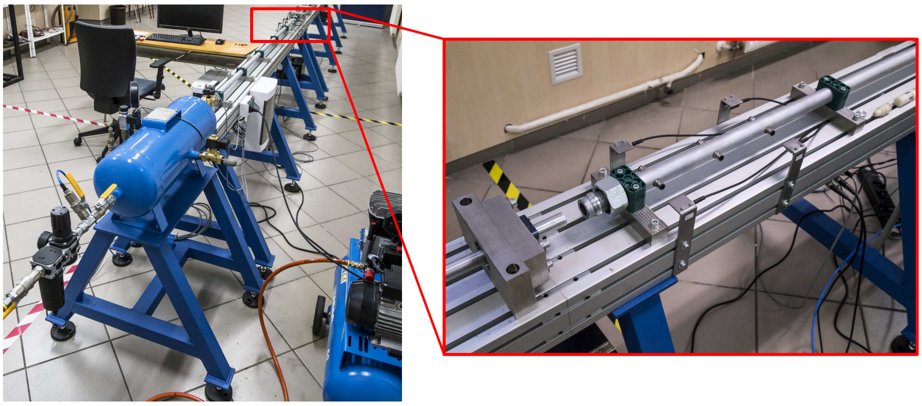

Figure 4.10: The gas-gun system.

Measurement bars

The measurement bars are mounted to the frame using universal bearing supports. The universal bearing supports are designed to accommodate the modular split-housing bearings (drylin TJUM, Igus, Germany) with diameters of 20 mm, 30 mm, and 40 mm respectively. The housings are designed in a way that the measurement bar can be inserted or removed from the setup without the removal of the strain-gauges. In the default arrangement, the overall length of both measurement bars can be approx. 3500 mm (commonly 2 × 1600 mm). The universal supports allow for the two-directional adjustment of the bar's axis. The co-axiality and straightness of the whole system are adjusted using a pair of cross line lasers. The measurement bar system with the universal bearing supports is shown in Fig. 4.11.

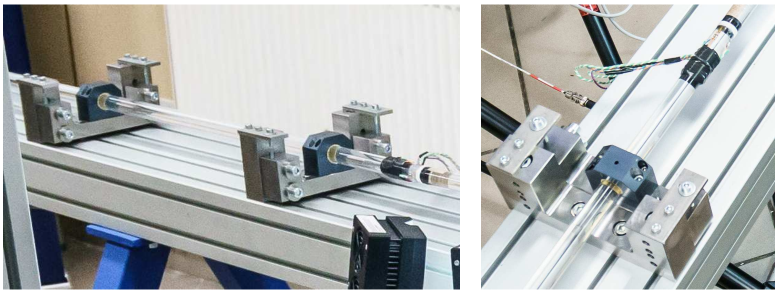

Figure 4.11: Bar with the universal bearing supports.

Momentum trap and damping elements

The momentum trap absorbs the residual energy of the experiment and is a key element for the safe and reliable operation of the setup. As the momentum trap has to withstand considerably high impact energy (typically hundreds of joules) it is designed as a system with several energy absorbing elements. The momentum trap consists of a short bar clamped in the holders, an expendable wooden insert and an industrial hydro-pneumatic damper (type MA4550EUM, ACE Controls, USA). At first, the energy is dissipated during the friction contact of the clamped bar, then in the crushing or destruction of the wooden insert and finally in the hydro-pneumatic damper. The momentum trap with the damper is shown in Fig. 4.12.

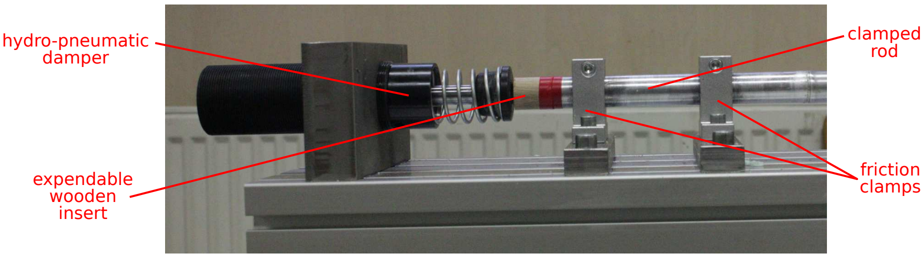

Figure 4.12: The momentum trap with the hydro-pneumatic damper.

Accessories and peripherals

The system is equipped with a number of accessories and peripherals, namely, e.g., an air compressor for the production of compressed air, an air filter and air conditioning devices, a striker loading system, cabinets for the instrumentation, polycarbonate safety shields, a compressed air control system, pressure gauges, control electronics and the circuitry.

4.6 Instrumentation

The instrumentation of the setup is used for the data acquisition during the experiment and is a crucial part for the reliable and precise evaluation of the results. The instrumentation consists of many parts and sub-systems. All the parts of the instrumentation are described in detail in the following paragraphs.

4.6.1 Parameters and quantities

The minimal set of parameters and quantities that have to be measured or calculated for the relevant evaluation of the Hopkinson bar experiment are summarized in Tab. 4.4.

Quantity	**Sensor**	**Unit**
Directly measured quantities		
Time	high-speed digitizer	[s]
Striker bar impact velocity	optical gate	[ms^{-1}]
Strain pulses	strain-gauge	[$-$]
Air pressure	pressure-gauge	[Pa]
Bar's ends displacement	DIC	[m]
Specimen geometry	-	[m]
Bar length and diameter	-	[m]
Calculated quantities		
Bar's ends velocity	strain-gauge	[ms^{-1}]
Bar's Young's modulus	strain-gauge	[Pa]
Bar's wave propagation velocity	strain-gauge	[ms^{-1}]

Table 4.4: The directly measured and calculated quantities in the Hopkinson bar setup.

4.6.2 System overview

The instrumentation system consists of several sub-systems, namely: a strain-gauge measurement system, an experiment triggering and data acquisition system, a high-speed imaging system, a striker impact velocity measurement system, and a main control system. The strain-gauge measurement system contains a power supply, the individual strain-gauges with the related circuitry and amplifying electronics. The experiment triggering and data acquisition system consists of a high speed digitizer interconnected with optical gates from the impact velocity measurement system for the synchronization of the acquired data with the high-speed camera images. The high-speed camera is a part of the high-speed imaging system that captures and recovers a set of high speed images to the PC. The main control system consists of a PC with a LabView interface (National Instruments, USA) together with high-speed camera control software. When the experiment was triggered, all the data are recorded synchronously by the individual components (high speed digitizer, high-speed camera) and are automatically uploaded to the PC after the experiment. An overview of the Hopkinson bar instrumentation is shown in Fig. 4.13. The system is controlled by an in-house developed virtual instrument in the LabView interface. The design and commissioning of the whole instrumentation system was the teamwork of a few researchers and students working on the individual parts. A more detailed description of the instrumentation system is provided in the relevant publications [7, 128, 129].

4.6.3 Strain-gauges

Strain-gauges are devices for the direct measurement of strain, typically in a mechanically loaded object. They are the most important part of the instrumentation as they represent an irreplaceable tool for the evaluation of the experiment output (see Tab. 4.4). The strain-gauges are mounted directly on the surface of the measurement bars and measure the elastic strain waves propagating in the bars. In this thesis, two types of strain-gauges were tested: (i) foil strain-gauges and (ii) semiconductor strain-gauges.

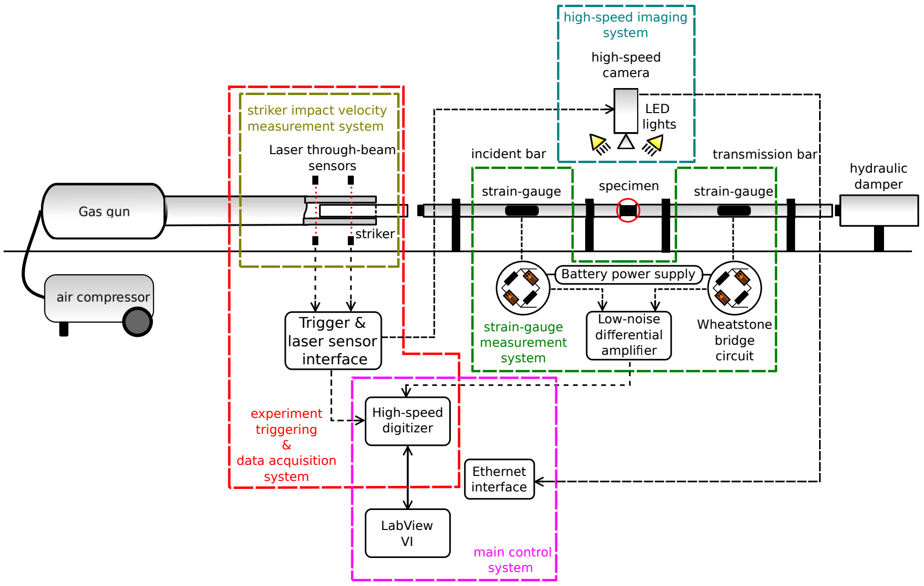

Figure 4.13: The overview of the Hopkinson bar instrumentation.

Foil strain-gauges

The foil strain-gauge consists of a thin flexible insulating backpacking that holds a conductive metallic foil pattern. The strain-gauge is attached to the surface by an adhesive, in our case - cyanoacrylate bonding (Z70, HBM, Germany). As the bar deforms during the propagation of the elastic strain wave in the setup, the foil strain-gauge is also deformed. The metallic pattern changes its electrical resistance that affects the voltage signal measured by the high-speed digitizer. For the higher output and compensations of the errors, the gauges are connected to a Wheatstone bridge (see Section 4.6.3). With the known properties of the strain-gauge, the strains can be calculated using the recorded voltage signal. The length of the strain-gauge affects its frequency bandwidth, therefore, in the Hopkinson bar apparatus, short strain-gauges with a high frequency bandwidth should be used. For our purposes, foil strain-gauges with an active length of 3 mm (3/120 LY61, HBM, Germany) were commonly used and exhibited very good results. The main advantages of the foil strain-gauges are the almost ideal linearity, the high strain capacity, mechanical durability, low cost, and relatively simple manipulation and mounting. The main disadvantage is the low gauge factor and, thus, worse sensitivity and small changes of the output signal (lower signal-to-noise ratio). For more information about the bonding process, circuitry and noise reduction techniques, please refer to contribution [7]. The foil strain-gauge mounted on the bar is shown in Fig. 4.14.

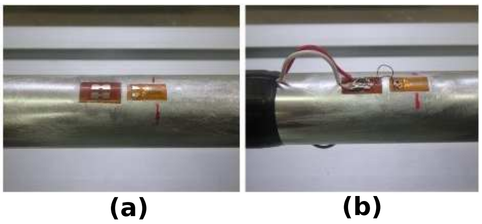

Figure 4.14: The foil strain-gauge mounted on the bar: (a) strain-gauge after bonding, (b) strain-gauge with wiring.

Semiconductor strain-gauges

The principle of the semiconductor strain-gauge is based on a change in the electrical resistance of the semiconductor material in the sensor. The main advantage of the semiconductors is the higher gauge factor (higher sensitivity, higher output signal and higher signal-to-noise ratio) and the possible application without a signal amplifier. However, they have several major disadvantages limiting their application in the Hopkinson bar setup, particularly for testing the cellular meta-materials. The main disadvantage is the significant non-linearity, the asymmetric response of the sensor in tension and compression, the very limited strain capacity, the higher sensitivity to temperature changes, the higher cost and the more complicated manipulation. A semi-conductor strain-gauge is shown in Fig. 4.15.

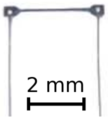

Figure 4.15: The semiconductor strain-gauge.

For our purposes, two types of semiconductor strain-gauges were tested: (i) AP170-3-100/BP/CuSn N-sort (VTS Zlin, Czech Republic), (ii) AFP-500-090 (Kulite, USA), however, none of them were used in any experimental campaign with the meta-materials as their applicability in the Hopkinson bar setup was found to be very limited. One of the key problems was the strongly non-linear response of the sensor starting from the very low values of the strain (typically $500 - 1000\,\mu\epsilon$). Although the manufacturers allow for applications with maximal strains of up approx. $2000\,\mu\epsilon$, in the Hopkinson bar, the strain-gauges started to indicate unreliable values at much lower strains. Moreover, the response of the gauge in tension and compression was not symmetric. Calculation of the strain using a formula corresponding to the non-linear behavior of the sensor did not produce better results than those of the foil strain-gauges. The difference between the recorded signals of the foil strain-gauge and semiconductor strain-gauge mounted in two pairs at the same measurement point on the bar is shown in Fig. 4.16. Note, that because of its non-linearity, the semiconductor strain-gauge started to exhibit invalid strain-values at very low strains. Unfortunately, the possible application of the semiconductor strain-gauges as a sensor for the measurement of the low transmission signals is also practically impossible. As high strain amplitudes (much higher than the allowed capacity of the semiconductor) propagate in the setup many times during the experiment (until they are captured by a momentum trap), the semiconductor strain-gauges are repetitively stressed beyond their limits. Usually, the strain values started to be unreliable after a few experiments (often after a single experiment only). Together with their limited lifetime (typically approx. 10 experiments) in comparison with the foil strain-gauges (typically approx. 50-100 experiments), their use in our setup was abandoned. Although some authors recommend semiconductor strain-gauges for the application in the Hopkinson bar [130–133], we have not been able to successfully employ them for our purpose and we consider their applicability unsuitable for such type of experiments.

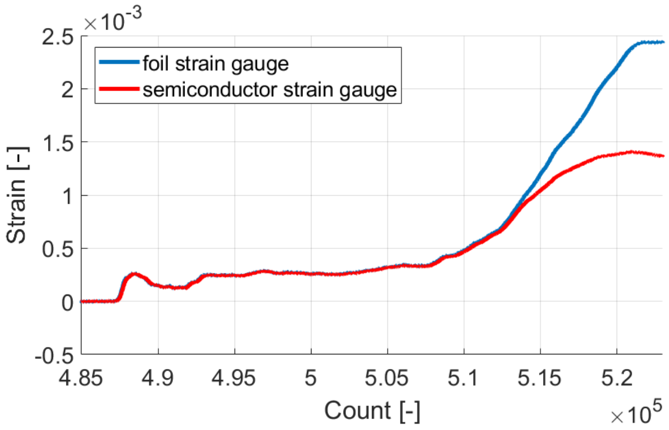

Figure 4.16: The difference between the recorded signals of the foil strain-gauge and the semiconductor strain-gauge mounted in two pairs at the same measurement point.

Wheatstone bridge arrangement

The principle of the strain-gauge is based on the change of its electrical resistance with its deformation. However, the change in the resistance is very small and cannot be detected directly. Instead, the value of the resistance is determined indirectly by the measurement of the voltage unbalance (the unbalance is caused by the change of the electrical resistance of the stressed strain-gauge) of the special circuit. One of the most used circuit for this purpose is the Wheatstone bridge. The Wheatstone bridge is an electrical circuit used to measure an unknown electrical resistance by the measurement of the voltage balance of the circuit. The bridge circuit is very precise and allows for the detection of very small changes in the resistance. The electrical scheme of the Wheatstone bridge is shown in Fig. 4.17. The behavior of the circuit can be described by the formula [129]

$$\frac{U_{\mathrm{exc}}}{U_{\mathrm{out}}} = \frac{1}{4} \cdot \left(\frac{\Delta R_1}{R_1} - \frac{\Delta R_2}{R_2} + \frac{\Delta R_3}{R_3} - \frac{\Delta R_4}{R_4} \right), \tag{4.20}$$

where the individual variables correspond with the scheme in Fig. 4.17.

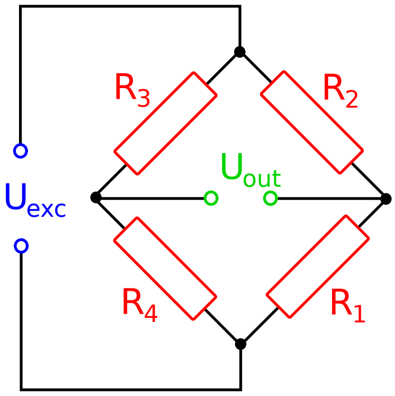

Figure 4.17: Scheme of the Wheatstone bridge.

In the application with the strain-gauges, many variants of the Wheatstone bridge connections are possible [129]. In our case, the so-called half-bridge arrangement was used at the individual measurement points. In the half-bridge arrangement, a pair of strain-gauges is mounted at the same distance from the impact face of the bar with a half-revolution angular separation.

The gauges are connected to the Wheatstone bridge to compensate for the eventual minor bending of the bar during the experiments (as the positive and negative values from the strain-gauges are subtracted) and to amplify the pure tensile or compression loads (as the positive or negative values from the strain-gauges are summed to produce the doubled output). Use of the half-bridge arrangement was a reasonable trade-off between a number of strain-gauges, the error compensation and signal amplitudes. Moreover, in the case of the failure of one strain-gauge in the pair, the arrangement could be immediately modified for the quarter-bridge (producing a lower quality output, but keeping the operability of the setup).

For the modular wiring and reliable operation of the strain-gauges, in-house designed electronics were produced for the simple ad-hoc connection and the conditioning of the strain-gauges. The quality of the cables used for the wiring and stability of the power supply was found to be a crucial point in the noise reduction. Therefore, an in-house designed battery power supply and an in-house technique for the production of the twisted pair wires were developed. The progress in the noise reduction between the initial and the current version of the setup is shown in Fig. 4.18. Prior to the digitization, the strain-gauge signals are amplified using a differential low noise amplifier (EL-LNA-2, Elsys AG, Switzerland) with a gain of 100. The development of the electronics and instrumentation of the strain-gauges were primarily undertaken by team member Jan Falta. For more information, refer to our papers [7, 128, 129].

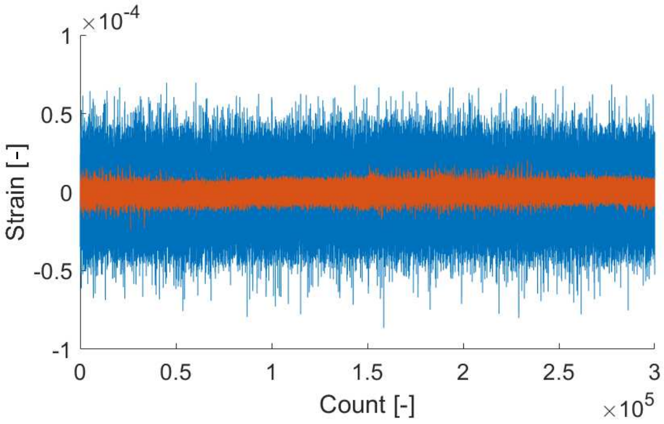

Figure 4.18: The progress in the noise reduction between the initial (blue) and the current (red) version of the setup.

Arrangement of the foil-gauges on the bars

Strain-gauges can be mounted on the measurement bars in a variety of arrangements. The fundamental arrangement has a single measurement point (a pair of strain-gauges connected in a half-bridge) in the middle of each bar. This arrangement is the optimal trade-off between the complexity of the system (the number of strain-gauges), the prevention of the wave superposition at the measurement point and the quality of the signal. This version was used in several experimental campaigns because of its simplicity and fast commissioning. However, as the specimen geometry was rather complex, the high impact velocities, required for the testing of the cellular materials, produced strain waves with high amplitudes, and the pulse-shaping technique prolonged the wavelength of the pulse, thus, more advanced arrangements of the strain-gauges were adopted. Using multiple measurement points on the bars allowed for the higher reliability, data redundancy (backup signals), and for the application of the advanced methods of the setup calibration [112], wave decomposition techniques [116, 118], and longer duration of the measurement [115, 117] (see Section 4.7.3 for more information). The following rules for the position of the strain-gauges were drawn based on the aforementioned literature and calibration measurements:

- The strain-gauges have to be placed at a distance of at least 10× the diameter from the bar's face.
- One transmission strain-gauge should be placed as close to the specimen as possible to get the most reliable record of its behavior and to prevent the wave superposition with the backward-propagating wave at the latter stage of the experiment.
- As the attenuation and wave dispersion are negligible when the aluminum alloy bars with an optimal pulse-shaper are used, the travel distance of the pulses can be relatively long (units of meters).
- In the case of the visco-elastic PMMA bars, the travel distance of the pulses has to be as short as possible ($< 1000\,\mathrm{mm}$). Otherwise, the wave dispersion correction methods [112] (see Section 4.7.3) produce unreliable results, particularly with high strain amplitudes.

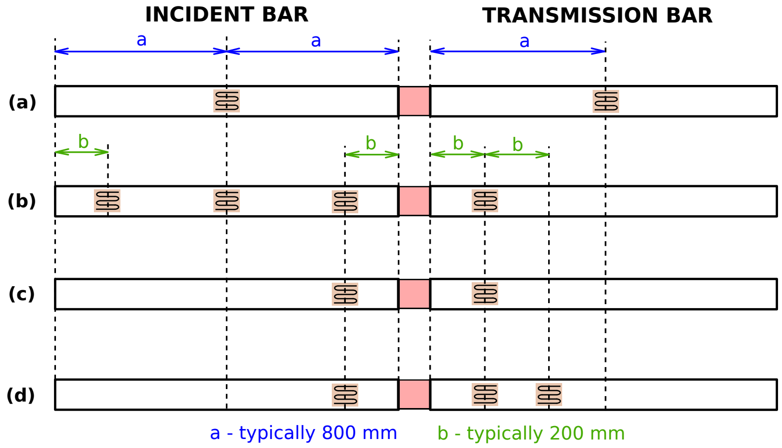

Figure 4.19: The variants of the strain-gauges arrangement used in the thesis: (a) standard Kolsky bar with strain-gauges in the middle of the bars, (b) multi-point measurement with SHPB, (c) direct impact OHPB bar, (d) direct impact OHPB with visco-elastic bars.

The variants of the strain-gauges arrangement used in the thesis are shown in the scheme in Fig. 4.19.

Quasi-static force calibration

The quasi-static force calibration of the strain-gauges is a key task for the evaluation of the setup precision and has been conducted prior to every experimental campaign. During the quasi-static calibration, the measurement bars of the setup are subjected to an uni-axial compression using a piston mounted on the end of the experimental setup. A conventional membrane load-cell (U9B, HBM, Germany) is mounted co-axially between the bars (as the specimen). The values of the force calculated from the strain-gauges (and the known material properties of the bars) are compared with the force indicated by the load-cell. Using the quasi-static calibration, the proper functionality and precision of the strain-gauges are verified. Typically, the error of the individual pair of foil strain-gauges is up to $2-4\,\%$ of the measured value. A typical output of the force calibration is shown in Fig. 4.20.

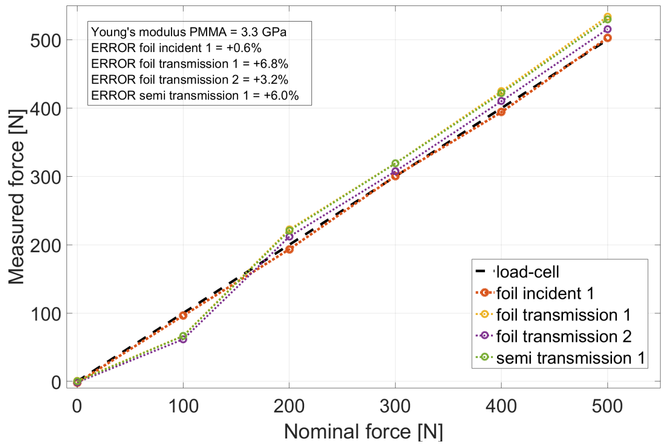

Figure 4.20: The result of the quasi-static force calibration - the comparison between the strain-gauges and the load-cell.

4.6.4 Impact velocity measurement

The measurement of the impact velocity of the striker bar (or muzzle velocity) is important for the estimation of the strain wave amplitude and, thus, for the rough estimation of the output of the experiment (ad-hoc detection of non-valid data). According to Eq. 4.6, the strain wave amplitude is directly proportional to the impact velocity. Therefore, impact velocity can be used for the initial estimation of the experiment validity. In the case of the aluminum alloy elastic bars, where the attenuation over a short travel distance can be neglected, the maximum strain measured using the strain-gauge can be directly compared with the value calculated using the measured impact velocity. The difference is usually in the range of a few percent. The estimated value and measured incident strain pulse are compared in Fig. 4.21.

Physically, the measurement of the impact velocity is performed using a pair of through-beam photoelectric sensors (FS/FE 10-RL-24 PS-E4, Sensopart, Germany) with a short reaction time ($125\,\mu$s) mounted on the gas-gun barrel. These sensors serve as an optical gate. The complete sensor consists of a transmitter of the laser beam and its receiver. When the laser beam is interrupted by a foreign object in its path, the voltage signal instantly changes. The path of the laser, oriented perpendicularly to the barrel, is interrupted by the striker bar moving through the barrel. Two optical gates output is connected to the same high-speed 16-bit digitizer (PCI-9826H, ADLINK

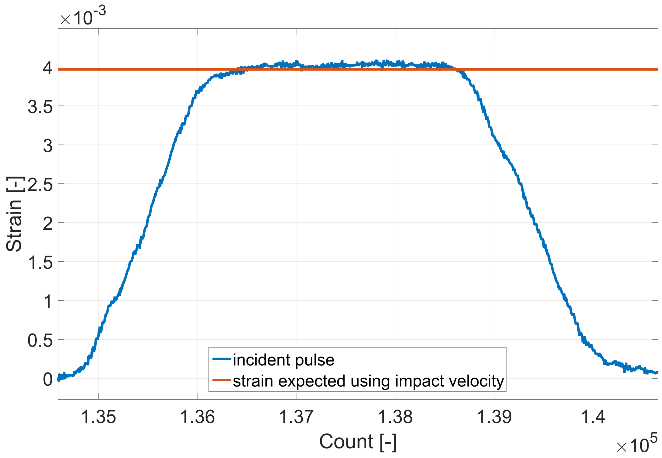

Figure 4.21: The estimated strain amplitude calculated from the impact velocity compared with the measured pulse.

Technology, Taiwan) that is able to measure the time with a high precision (constant sampling rate of 20 MHz in our case). Using the known distance between the optical gates and the measured travel time, it is possible to calculate the velocity of the striker. As the striker bar is accelerated through the whole length of the gas-gun barrel, the calculated striker velocity is averaged per distance between the optical gates. Therefore, it is important to mount the optical gates as close as possible to each other. In our case, we have also used an approach with three optical gates where the acceleration of the striker is taken into account using a simple constant acceleration analytical model. This approach has allowed for the even higher precision of the estimated strain amplitude. The system of the optical gates is also used for the triggering of the data-acquisition during the experiment (as the memory capacity of both high-speed digitizer and the high-speed camera are limited to a short period of time) and for the synchronization of the strain-gauges data with the high-speed camera images using the synchronization TTL pulse train. In the case when the transparent PMMA bar is used as a striker, the frontal part of the striker has to be painted or matt-brushed to prevent the laser beam passing through. The scheme of the experiment triggering and impact velocity measurement system is shown in Fig. 4.22. The optical gates mounted on the barrel are shown in Fig. 4.23. For more information, refer to [7, 128, 129, 134].

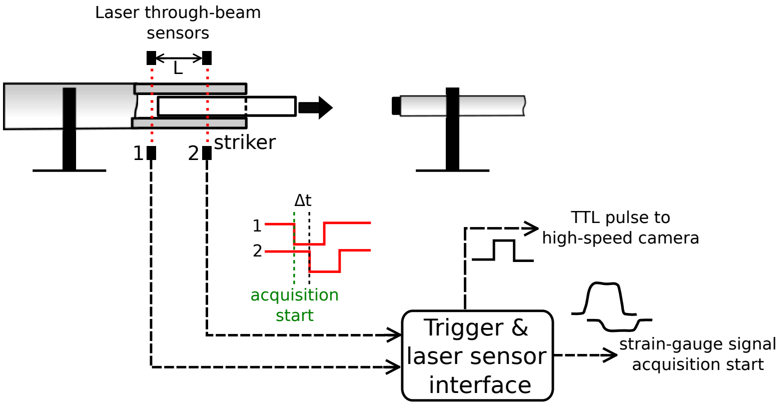

Figure 4.22: The scheme of the experiment triggering and impact velocity measurement system.

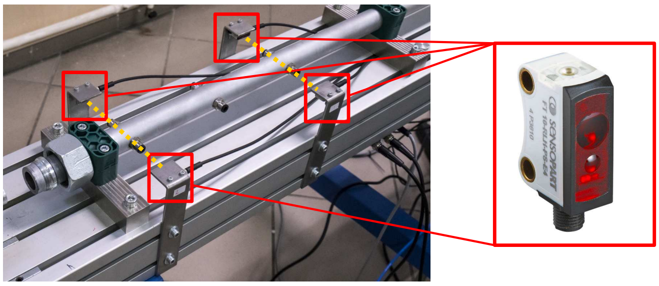

Figure 4.23: Optical gates mounted on the barrel.

4.6.5 High-speed imaging system

In our setup, high-speed imaging of the impact experiments is used not only as an inspection technique, but also for the advanced analysis of the experiments using DIC. The high-speed imaging system consists of a high-speed camera, a high performance illumination system, a camera positioning stage, a control PC and the interconnecting circuitry for the time synchronization. A block scheme of the high-speed imaging system is shown Fig. 4.24.

The high-speed camera is, by definition, a device capable of capturing images with an exposure of less than 1 ms with a frame rate in excess of 250 fps [135]. Nowadays, digital high-speed cameras are equipped with an internal memory for the immediate temporary storage of the captured images, a high-resolution image CMOS sensor and advanced internal control electronics. In our case, two types of state-of-the-art digital high-speed cameras with an internal

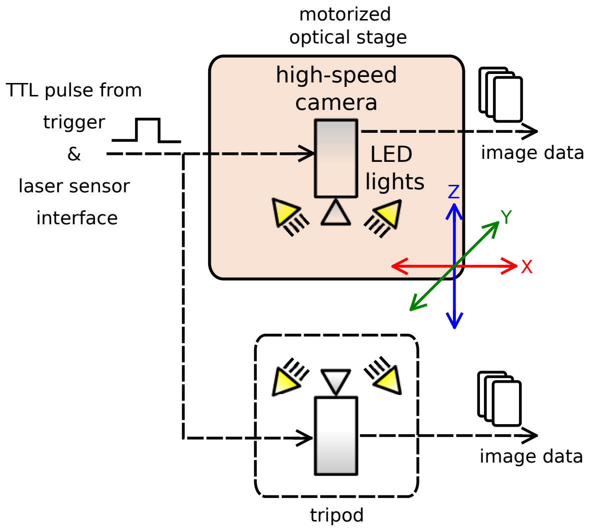

Figure 4.24: The scheme of the high-speed imaging system.

recording memory were used: (i) Fastcam SA-5, (ii) Fastcam SA-Z (Photron, Japan). Both cameras are capable of capturing an SHPB experiment with a sufficient frame-rate in the range of 50 − 300 kfps. Typically, the amount of the captured images during the experiment varies between a few images (10-20) to hundreds (< 300) of images depending on the strain-rate. The main parameters of the cameras used in the study are summarized in Tab. 4.5. In the initial stage of the study, only one SA-5 camera was available. In the latter stage of the study, two SA-Z cameras were available for the experiments. Both types of used cameras are shown in Fig. 4.25.

Parameter	**Fastcam SA-5**	**Fastcam SA-Z**	**Unit**
Max. frame rate	$1 \cdot 10^6$	$2.1 \cdot 10^6$	fps
Max. resolution	1024×1024	1024×1024	px
Max. full-frame speed	7000	20000	fps
Light sensitivity	10000	50000	–
Sensor type	12-bit ADC	12-bit ADC	–
Pixel size	20×20	20×20	μm
Min. shutter speed	1000	159	ns
Internal storage	16	16	GB

Table 4.5: The main parameters of the cameras used in the study.

(a) **(b)**

Figure 4.25: The high-speed cameras used in the study: (a) Photron Fastcam SA-5, (b) Photron Fastcam SA-Z.

As very short shutter speeds (typically units of μs) are used in the high speed imaging, the observed scene has to be very well illuminated. In our case, two high performance LED illumination systems were used: (i) Constellation 60 (Veritas, USA), (ii) Multiled QT (GS Vitec, Germany). Both types were able to deliver sufficient luminous flux to illuminate the scene for the imaging at frame rates of approx. 300 kfps. Even during the experiments at the highest possible strain-rate of our setup, the performance of the illumination system was not a limiting factor for the imaging. The illumination system was mounted directly on the main aluminum profile of the setup. Both illumination systems are shown in Fig. 4.26.

Stationary tripods or an in-house motorized remote-controlled hybrid optics positioning system (HOPS) [136] were used to carry the high-speed cameras. To protect the operators, the high-speed cameras, optics, illumination system and other costly parts of the experimental setup, the area of the specimen was

(a) **(b)**

Figure 4.26: The LED illumination systems used in the study: (a) Constellation 60, (b) Multiled QT.

insulated using a single-piece of a transparent shield made of high performance non-shattering polycarbonate with a thickness of 5 mm. The overall high-speed imaging system with all the parts mounted is shown in Fig. 4.27. The safety shield with the illumination system during testing is shown in Fig. 4.28.

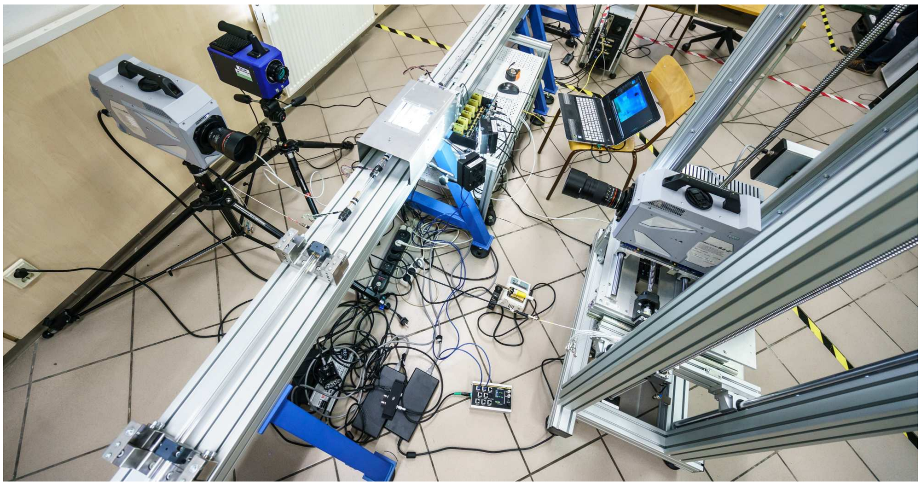

Figure 4.27: The high-speed imaging system with all of the mounted parts.

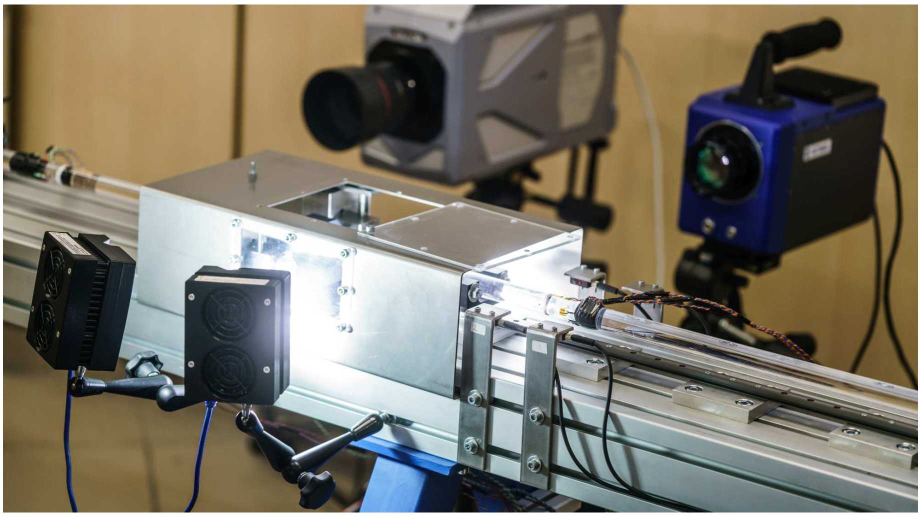

Figure 4.28: The safety shield with the illumination system during the testing. Here, the older version of the shield made of stainless steel with the plexiglass windows is shown. The actual version of the shield is shown, e. g., in Fig. 5.45.

4.7 Evaluation of the SHPB experiments - strain-gauges

In this part, the evaluation of the strain-gauges data is described in detail. The evaluation of the data is, in principle, based on the one-dimensional strain wave propagation theory described in Section 4.2.1. However, more complex and advanced techniques based on the relevant literature [112, 117] were adopted in the evaluation process to account for the effects connected with the superposition of the waves, wave dispersion, non-ideal setup geometry, imperfect contacts, and sensor errors.

4.7.1 Software tools

A series of MATLAB software (MathWorks, USA) scripts and functions for the evaluation of the data recorded during the experiment was created. This simple toolbox can be used for the complete analysis of the data from both the SHPB and OHPB (direct-impact method, see Section 4.9) experiments and for the processing of the data evaluated using the DIC (see Section 4.8). Namely, the following functions have been included in the toolbox:

- Data loading and conversion to the MATLAB compatible format.
- Evaluation of the striker impact velocity.
- Strain-gauge signal conditioning (various types of filtering, tare, offsetting).
- Calculation of the strain from the strain-gauge signals (various types of bridge connections, foil linear types, semiconductor linear and non-linear types).
- Selection of the strain wave pulses.
- Simple or advanced (frequency domain based) time shifting of the pulses.

- Analysis of the wave dispersion effects.
- Calculation of the dynamic material properties of the bars.
- Basic wave decomposition techniques for multi-point measurements.
- Calculation of the SHPB results (various techniques - with nominal bar properties, linear elastic experimental based properties, visco-elastic bar properties, etc.).
- Calculation of the OHPB results (various techniques - with nominal bar properties, linear elastic experimental based properties, visco-elastic bar properties, etc.).
- Basic comparison of the strain-gauge data with the DIC data.
- Data and results export.

The toolbox is a set of scripts and functions that can be independently connected together to produce more sophisticated software interfaces or scripts tailored for the particular experimental setup or campaign. The basic toolbox has been expanded by other team members to include some other features such as an automatic data import or an assisted plotting and data export. Refer to the [134] for more details. The basic toolbox developed by the author is available as an attachment (see Appendix B) to this thesis.

4.7.2 Simple evaluation

The experimental data are loaded in the MATLAB software and all the variables are automatically imported. Depending on the type of the experiment, the striker impact velocity is calculated using the signals from the optical gates or the DIC. The strain-gauge signals are conditioned (tared and filtered if necessary) and the measured voltages are converted to the strains using the formula reflecting the type of the Wheatstone bridge and strain-gauge. A variety of filters can be used to clean the strain-gauge signals. Commonly, an IIR Butterworth filter or a Savitzky-Golay digital filter are used to reduce the noise, while, in the case of the well pulse-shaped experiments, no filtration is necessary - for more information, refer to the contributions [3, 137, 138]. After the signal conditioning, the relevant strain wave pulses are selected. The nominal linear elastic material properties or experimentally evaluated linear elastic or visco-elastic properties of the bars can be used for further processing. After the precise time shifting of the pulses and the correction of the wave dispersion effects (see Section 4.7.3), the results are evaluated according to the one-dimensional wave propagation theory (see Section 4.2.1). The strain of the specimen is calculated by the integration of the strain-rate according to Eq. 4.3 while the stresses (or forces) at the specimen boundaries are calculated using Eq. 4.4 and 4.5. Then, the dynamic equilibrium can be checked and the validity of the experiment evaluated. The typical strain-gauge data of the experiment are shown in Fig. 4.29. The results of the experiment with both poor and good dynamic equilibrium are shown in Fig. 4.30, the representative stress-strain curves are shown in Fig. 4.31.

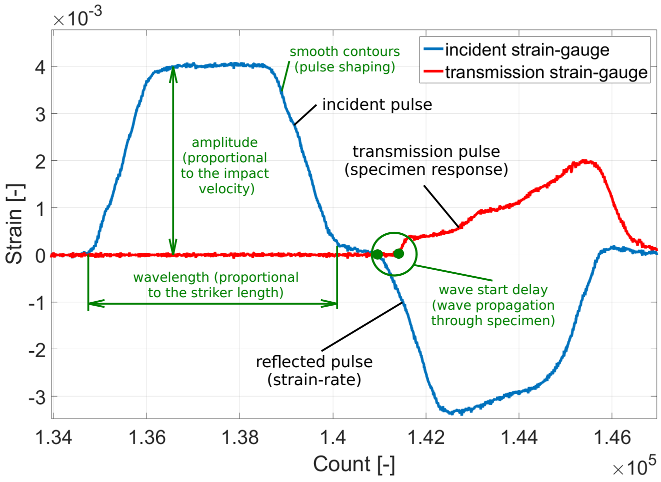

Figure 4.29: The typical strain-gauges data of the SHPB experiment. Experiment with an additively manufactured auxetic lattice.

4.7.3 Wave dispersion effects, analysis and corrections

The effects of the imperfections and wave dispersion are always included in the real data. To minimize these effects and to get precise and relevant results, one has to analyze the wave dispersion effects and imperfections of the setup and experimentally evaluate its dynamic mechanical properties. Techniques based on the signal decomposition in the frequency domain published by

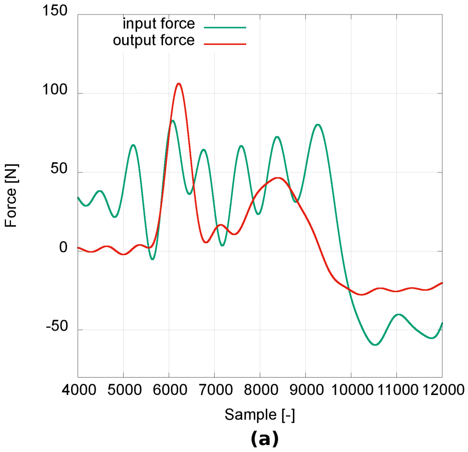

Figure 4.30: The results of the experiment with poor (a) and good (b) dynamic forces equilibrium. The specimen (a) was an ordnance gelatin, the specimen (b) was a poly-propylene putty. Both were tested in the SHPB with the PMMA bars.

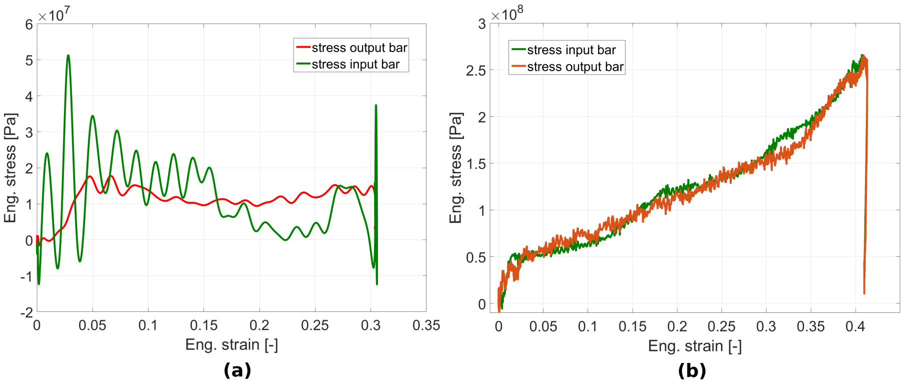

Figure 4.31: The stress-strain diagram with poor (a) and good (b) dynamic forces equilibrium. The specimen (a) was the hybrid Ni/Pu open-cell foam, the specimen (b) was an additively manufactured auxetic lattice. Both were tested in the SHPB with the aluminum alloy bars.

Bacon [112, 118] and others [115, 117] were adopted for the evaluation of the actual mechanical properties of the bars and for the correction of the wave dispersion effects. The method, introduced by Bacon [112], applies the theory of linear visco-elasticity represented by a complex modulus of the material. For such a model, the propagation coefficient γ (a function of the angular velocity/frequency in Fourier domain, $\gamma(\omega)$) can be written as

$$\gamma^2 = -\frac{\rho\omega^2}{E^*}, \tag{4.21}$$

where ρ is the density of the bar and E^* is its complex modulus. The one-dimensional equation of the wave axial motion can be written as

$$\left(\frac{\partial}{\partial x^2} - \gamma^2\right)\widetilde{\epsilon}(x,\omega) = 0, \tag{4.22}$$

where x is the position and $\widetilde{\epsilon}$ is the Fourier representation of the longitudinal strain. The general solution of Eq. 4.22 is represented by

$$\widetilde{\epsilon}(x,\omega) = \widetilde{P}(\omega)e^{-\gamma x} + \widetilde{N}(\omega)e^{\gamma x}, \tag{4.23}$$

where $\widetilde{P}(\omega)$ and $\widetilde{N}(\omega)$ are the forward-propagating and backward-propagating strain waves at position $x = 0$, respectively. Using the aforementioned equations, the Fourier transforms of the axial particle velocity $\widetilde{v}(x,\omega)$ and normal force $\widetilde{F}(x,\omega)$ are given by

$$\widetilde{v}(x,\omega) = -\frac{i\omega}{\gamma}\left[\widetilde{P}(\omega)e^{-\gamma x} - \widetilde{N}(\omega)e^{\gamma x}\right], \tag{4.24}$$

$$\widetilde{F}(x,\omega) = -\frac{\rho A\omega}{\gamma^2}\left[\widetilde{P}(\omega)e^{-\gamma x} - \widetilde{N}(\omega)e^{\gamma x}\right], \tag{4.25}$$

where A is the cross-sectional area of the bar. The propagation coefficient $\gamma(\omega)$ is related to the attenuation coefficient $\alpha(\omega)$ and the phase velocity $c(\omega)$ by relation

$$\gamma(\omega) = \alpha(\omega) + i\frac{\omega}{c(\omega)}. \tag{4.26}$$

When two subsequent strain wave pulses are measured, one can experimentally evaluate the propagation coefficient of the visco-elastic (or linear elastic) bar as well as its mechanical properties. The transfer function H^* between two subsequent pulses and the propagation coefficient can be found according to the relation (the formula depends on the arrangement, in this case - the returning wave from the free end of the bar)

$$H^* = -\frac{\widetilde{\epsilon_2}(\omega)}{\widetilde{\epsilon_1}(\omega)} = e^{-\gamma 2d}, \tag{4.27}$$

where $\widetilde{\epsilon_1}(\omega)$ and $\widetilde{\epsilon_2}(\omega)$ are the measured strain pulses and d is the distance from the strain-gauge to the free end of the bar.

An example of the angular frequency dependent material properties experimentally evaluated for the high strength aluminum alloy EN-AW-7075-T6 bars using the aforementioned method is shown in Fig. 4.32. Note that real part of the complex modulus is very close to the chart value of approx. 70 GPa, whereas the imaginary part is close to zero exhibiting, thus, almost an ideal linear elasticity of the material. The wave propagation velocity is also close to the nominal value of 5100 ms^{-1} while the frequency dependent approach shows decrease in the velocity with the increasing frequency.

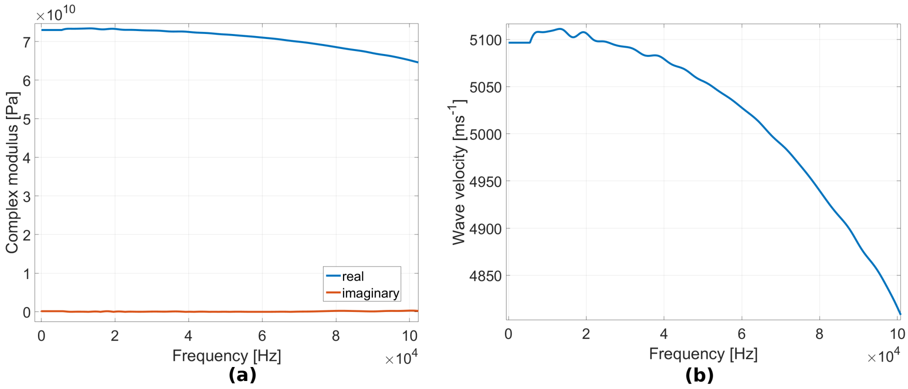

Figure 4.32: The angular frequency dependent material properties of the EN-AW-7075-T6 aluminum bars: (a) the real and imaginary part of the complex modulus, (b) the wave propagation velocity.

Using the aforementioned method, it is possible to compare the experimentally evaluated properties, valid for the actual setup, with the chart values. For the aluminum alloy, in our case, the difference between the calculated and chart values is always in the range of a few percent. Otherwise, there is a serious problem in the setup - error of the strain-gauge, poor geometry alignment, imperfect contact on the bars, etc. The experimentally evaluated values are very precise and can be used for the advanced time-shifting of the individual strain pulses. Analogically, the evaluation of the experiment can be made solely in the frequency domain, to account for the frequency dependent properties, and then transformed back to the time domain. In the propagation coefficient, all the errors related to the wave dispersion and geometrical imperfections are included and, thus, the waves can be corrected for such effects (to a certain point). During the research, it was found to be beneficial to use this method of time-shifting in combination with other methods (like pulse-shaping) further reducing the wave dispersion and other negative effects. Details concerning the actual technical realization of the forward and backward Fourier transformation, signal treatment, processing and analysis in the frequency domain can be found in the appropriate commented MATLAB functions in attachment (see Appendix B).

4.7.4 Wave superposition treatment

If the wavelength of the strain pulse is longer than the doubled distance to the free end of the bar, wave superposition will occur on the strain-gauge. The strain values of the forward-propagating pulse are summed up with the backward-propagating pulse and the measured signal is a result of the superposition providing wrong information of the actual strain on the boundary of the specimen. Some methods for the treatment of the wave superposition are available in the literature [115, 117, 118]. In the latter experimental campaigns of this study, a multi-point strain-gauge measurement was applied to maximize the strain of the specimen. However, the length of the used striker bar was always carefully selected not to produce longer wavelengths than a doubled distance between the first incident strain-gauge and the end of the bar. Thus, the method introduced by Zhao and Gary [117] could be adopted. The measured strain signal $\epsilon(t)$ can be decomposed on the individual forward-propagating $\epsilon_{\mathrm{F}}(t)$ and backward-propagating $\epsilon_{\mathrm{B}}(t)$ strain pulses using a simple relation

$$\epsilon(t) = \epsilon_{\mathrm{F}}(t) + \epsilon_{\mathrm{B}}(t). \tag{4.28}$$

If the whole initial incident pulse is measured somewhere on the incident bar without superposition, the method of time-shifting described in Section 4.7.3 can be used to decompose the signal of the other strain-gauge. The initial forward-propagating strain-pulse $\epsilon_{\mathrm{FA}}(t)$ measured at point A is time-shifted to the position of the other sensor B using the shifting function

$$\epsilon_{\mathrm{FB}}(t) = f_{\mathrm{shift}}\left[\epsilon_{\mathrm{FA}}(t)\right]. \tag{4.29}$$

Then, the backward-propagating pulse $\epsilon_{\mathrm{BB}}(t)$ can be calculated using the strain-gauge signal $\epsilon_{\mathrm{B}}(t)$ measured at point B according to formula

$$\epsilon_{\mathrm{BB}}(t) = \epsilon_{\mathrm{B}}(t) - \epsilon_{\mathrm{FB}}(t). \tag{4.30}$$

The known forward-propagating pulse $\epsilon_{\mathrm{FA}}(t)$ and backward-propagating pulse $\epsilon_{\mathrm{BB}}(t)$ can be time-shifted to the specimen boundary and the results of the experiment can be calculated conventionally using the techniques described in the aforementioned sections. This method can be also used repetitively to decompose the latter reflections and prolong the window of the experiment (to a certain point). However, in such an application, this method requires well-defined boundary conditions and a high-speed camera has to be used to inspect the behavior of the specimen in the subsequent pulses. Otherwise, it can produce invalid results. This approach has been tested, but the results are not shown in the thesis. The data of the experiment with the superposed strain-gauge signal is shown in Fig. 4.33 using red color. In this case, the strain-gauge in the position without superposition (note the blue curve in Fig. 4.33) was also mounted. The separated pulses from the strain-gauge with the superposition and the pulses from the strain-gauge without the superposition are compared in Fig. 4.34.

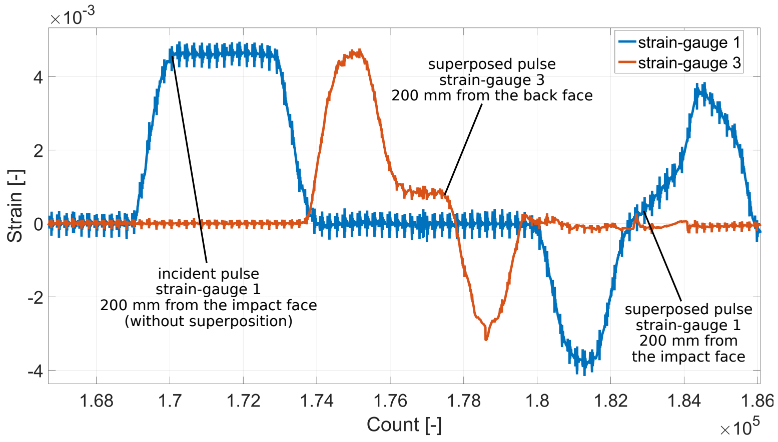

Figure 4.33: The data of the experiment with the superposed strain-gauge signal.

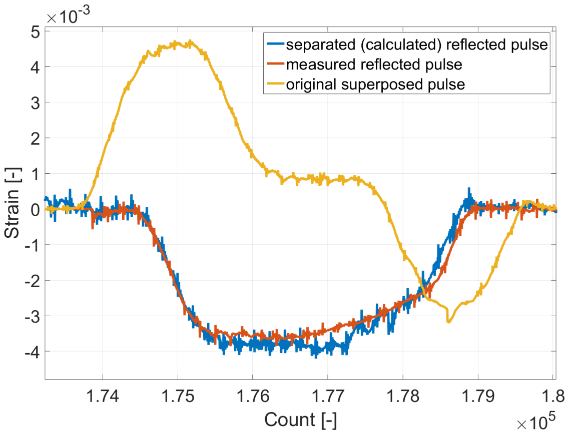

Figure 4.34: The separated pulses from the strain-gauge with the superposition compared with the pulses from the strain-gauge without the superposition.

4.7.5 Pulse-shaping

A pulse-shaper [121, 122] is a small piece of soft material that is put on the impact face of the incident bar. During the impact of the striker bar, the pulse-shaper plastically deforms that affects the strain pulse developed in the incident bar. The pulse-shaper serves as a low-pass frequency filter as it effectively prevents the transfer of high frequency oscillations to the incident bar. Moreover, the pulse-shaper modifies the shape of the incident pulse as the strain wave does not develop abruptly, but rather gradually and smoothly. Pulse-shaping can be used for the reduction of the "ringing" effects on the specimen's boundary and for the extension of the ramp-in period of the pulse to provide more time to establish dynamic equilibrium in the specimen.

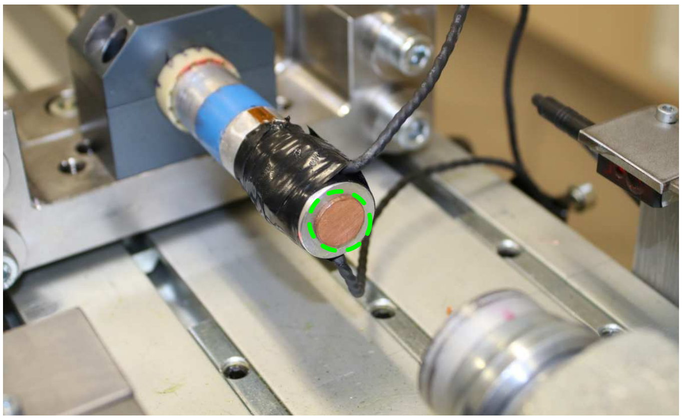

Figure 4.35: The pulse shaper mounted on the impact face of the incident bar.

In this study, small diameter thin pure soft copper cylinders (Cu-ETP R220) were used as pulse-shapers. The diameter and thickness of the shaper had to be optimized for the given specimen and strain. In general, pulse-shapers with a diameter in the range of $4 - 10\,\mathrm{mm}$ and a thickness in the range of $0.5 - 1.5\,\mathrm{mm}$ were used. The pulse-shaping technique was found to be very effective, as for the aluminum alloy bars, it can produce smooth pulses almost without any dispersion. For instance, in the latter experimental campaigns when the in-house low noise wiring was used for the strain-gauges and the wave was well pulse-shaped, no filtration of the strain-gauge signals was necessary. The pulse-shapers were fixed on the impact face of the incident bar using a small amount of grease. Both faces of the pulse-shaper have to be lubricated to reduce friction with the bar during the extensive plastic deformation. The diameter of the pulse-shaper has to be small to achieve the

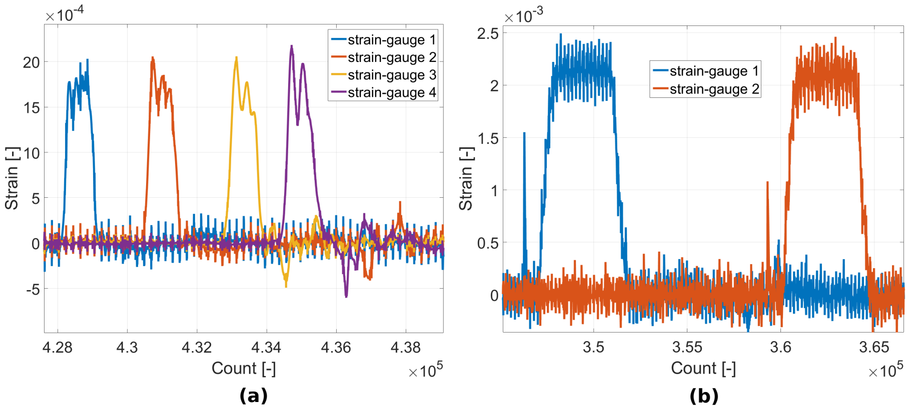

Figure 4.36: The comparison between the propagation of the pulse without any shaping (a) and the shaped pulse (b).

high stresses in the shaper to keep the flow of the plastic deformation. An extensive study covering the pulse-shaper design and simulation can be found in [139]. The pulse shaper mounted on the impact face of the incident bar is shown in Fig. 4.35. The comparison between the propagation of the pulse without any shaping and the shaped pulse is shown in Fig. 4.36.

4.7.6 Calibration of the setup

The calibration of the setup has to be carried out prior to the experimental campaign and consists of the geometry calibration and a series of void tests which is the last part prior to the commissioning of the setup. A void test is, in principle, a Hopkinson bar experiment without any specimen. Two variants of the void tests are performed: (i) the bars apart void test, (ii) the bars together void test.

Geometry calibration

The geometry calibration includes adjustment of the setup to pass the requirements on the straightness, co-axiality and precise contact between the bars. During the geometry calibration, a pair of cross line lasers mounted on tripods are used to indicate the straightness in both the vertical and horizontal direction. The first cross line laser is mounted in the axis of the main profile and indicates the longitudinal axis of the setup in the horizontal direction while the second cross line laser is mounted perpendicularly to the main profile and indicates the longitudinal axis of the setup in the vertical direction. The gas-gun barrel and all the measurement bars are adjusted to be co-axial with both lasers. Using this method, it is possible to achieve the straightness of the setup better than approx. 0.3 mm/m. During the calibration of the setup axis, the contact of the bars has to be also adjusted. A feeler gauge is used to check the quality of the contact between the bars. A feeler gauge with a thickness of maximally 0.05 mm has to tightly fit between the bars. A part of the geometry calibration procedure is shown in Fig. 4.37.

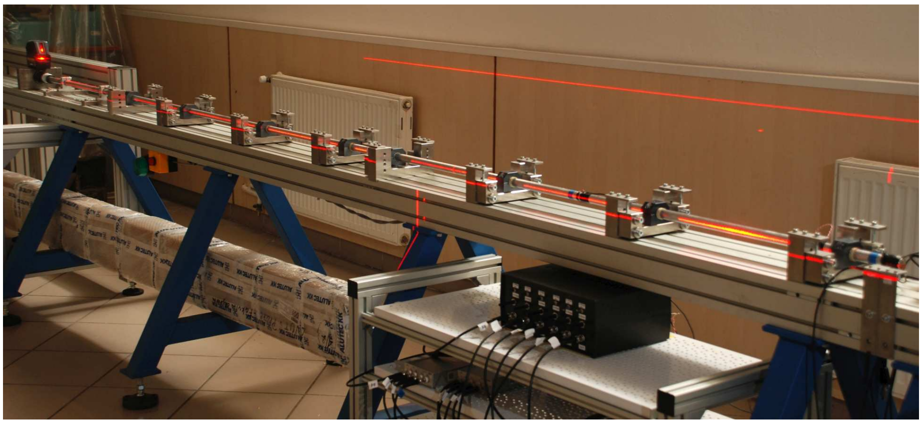

Figure 4.37: Part of the geometry calibration procedure. Two cross-line lasers are used to calibrate the longitudinal and lateral axis of the setup.

Bars apart void test

In the bars apart void test, the striker bar impacts the incident bar that is not in initial contact with the transmission bar. As the first incident wave is always measured without any wave superposition (in our case), the forward-propagating wave is fully reflected on the free end of the bar. The incident and reflected wave are compared and should be almost identical (affected slightly by the wave dispersion effects). Using the bars apart test, the linearity and symmetric response of the incident strain-gauge is evaluated. It can be also used for the measurement of the propagation coefficient according to Section 4.7.3. The typical output of the bars apart void test is shown in Fig. 4.38.

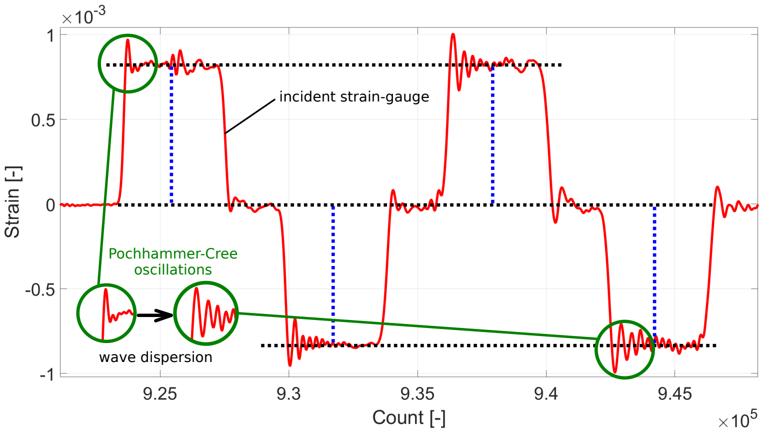

Figure 4.38: The typical output of the bars apart void test.

Bars together void test

During the bars together void test, the incident and transmission bar are in initial contact. By the impact of the striker bar, the forward-propagating incident wave is developed. The wave propagates through the incident bar. On the interface of the bars, a very small part of the incident wave is reflected back to the incident bar while the rest of the pulse propagates further to the transmission bar. As there is not any specimen between the bars, the wave measured by the transmission strain-gauge should be almost identical with the incident wave (affected slightly by the wave dispersion effects). If the pulse reflected on the interface of the bars is significant, the contact between the bars is not properly adjusted and the setup has to be re-assessed. If the incident and transmission pulses are significantly different, there is a serious problem in the setup - a strain-gauge error, poor geometry alignment, etc. Minor differences between the individual strain-gauges caused by the gauge alignment and different precision can be artificially eliminated using correction coefficients. However, this approach has to be carried out very carefully and the estimated coefficients have to be in agreement with both the void test and quasi-static calibration. This type of void test can be also used for the measurement of the propagation coefficient according to Section 4.7.3. The typical output of the bars together void test is shown in Fig. 4.39.

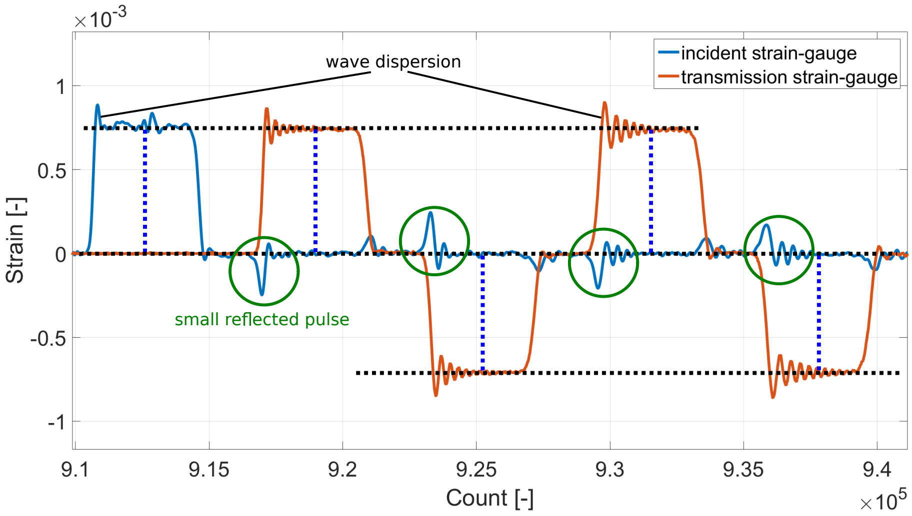

Figure 4.39: The typical output of the bars together void test.

4.8 Digital image correlation

DIC is an optical method that uses tracking and image registration techniques for the accurate measurements of the changes in the sequence of images [140]. In our case, DIC was employed for the evaluation of displacements of the individual correlation points on the surface of the specimen. The displacements of the correlation points were subsequently used to calculate the displacements of the selected parts of the image (e.g., the displacements of the bar's ends, the displacement of the individual cells in the specimens, etc.), strains, particle velocities or other quantities such as Poisson's ratio. DIC has been used for both the calibration of the setup as well as for the advanced analysis of the experiment.

4.8.1 Principle and custom software tool

The basic principle of DIC is based on the tracking of the selected correlation points (pixels) between two images (reference and deformed subset) recorded consecutively during a deformation process. The technique uses a maximization approach to find the correlation coefficient for the best fit between sub-images defined around the control points set in the reference (undeformed) image. Usually, a random speckle pattern is put on the surface of the object (using, e.g., air brush spraying technique) to improve the reliability of the tracking. This can be omitted in case of the samples with a distinctive pattern (structure). The scheme of the grid of the correlation points and the sub-images is shown in Fig. 4.40.

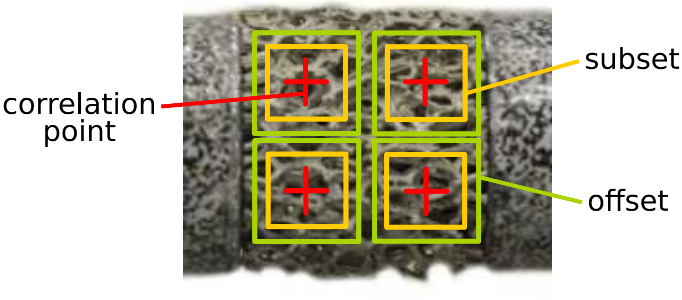

Figure 4.40: The scheme of the grid of the correlation points and the sub-images.

An in-house DIC toolkit developed by Ivan Jandejsek [141] was used. The DIC procedure works in two steps: the correlation is initially evaluated on the pixel level using the Lucas-Kanade algorithm [142] and, in the second step, the Newton-Raphson method is used to fit polynomial surface to enable the sub-pixel accuracy. In the first step (pixel accuracy), the normalized cross-correlation (NCC) method is used to calculate the integer value of the displacement. The deformation mapping function is extracted based on the correlation coefficient which is determined by examining the pixel intensity of the image subsets according to

$$r_{\mathrm{ij}}\left(u, v, \frac{\partial u}{\partial x}, \frac{\partial u}{\partial y}, \frac{\partial v}{\partial x}, \frac{\partial v}{\partial y}\right) = \tag{4.31}$$

$$= 1 - \frac{\sum_{\mathrm{i}} \sum_{\mathrm{j}} [I_0(x_{\mathrm{i}}, y_{\mathrm{j}}) - \bar{I}_0][I_1(x'_{\mathrm{i}}, y'_{\mathrm{j}}) - \bar{I}_1]}{\sqrt{\sum_{\mathrm{i}} \sum_{\mathrm{j}} [I_0(x_{\mathrm{i}}, y_{\mathrm{j}}) - \bar{I}_0]^2 \sum_{\mathrm{i}} \sum_{\mathrm{j}} [I_1(x'_{\mathrm{i}}, y'_{\mathrm{j}}) - \bar{I}_1]^2}},$$

where $I_0(x_{\mathrm{i}}, y_{\mathrm{j}})$ is the pixel intensity in the reference image at a point $(x_{\mathrm{i}}, y_{\mathrm{j}})$ and $I_1(x'_{\mathrm{i}}, y'_{\mathrm{j}})$ is the pixel intensity at a point $(x'_{\mathrm{i}}, y'_{\mathrm{j}})$ in the deformed image. $\bar{I}_0$ and $\bar{I}_1$ are the mean values of the intensity in the images I_0 and I_1, respectively. The maximum of the correlation coefficient is found using the steepest-gradient method and the new position of the point is localized where the current sub-image has the best correlation. The second step (sub-pixel accuracy) is performed by employing Gauss-Newton nonlinear optimization.

4.8.2 Conditions in impact testing

The correlation algorithm described in the previous subsection can be employed generally on any series of 2D images. However, the quality of correlation, its reliability and accuracy are strongly dependent on the quality of the image set. The randomness, contrast and quality of the random speckle pattern, rate of change between the images, image resolution and noise are particularly important parameters for the resulting reliability of the tracking by the correlation algorithm. While the application of the image correlation technique can be relatively straightforward in the quasi-static measurements [143,144], serious limitations and issues exist in the case of high strain-rate and impact testing [105]. The main problems can be summarized by the following points:

- A high frame-rate is necessary to capture the rapid changes and high deformations during the impact test.
- Using a high-speed camera, the higher frame-rates require a lower resolution of the images.
- During the rapid deformation, the random speckle pattern has to remain firmly attached to the surface of the sample.
- The scene has to be illuminated using a stable, non-fluctuating light source, preventing any changes in contrast.
- During the deformation of the specimen, no bright reflections on its surface and on the bars should occur.
- To compare the image data with other sensors (e.g., the strain-gauges), the precise timing and synchronization of the data-acquisition has to be achieved.
- As the specimens often disintegrate during the impact compression, reliable safety shield protecting the illumination, the optics and the camera itself has to be mounted. The shield has to be transparent and should not bring any significant optical distortion in the image.
- Lubrication by grease is commonly applied on the contact surface of the bars. During the impact, rapid escape and blow-out of the grease has to be prevented, otherwise the deformation of the specimen can be deteriorated by particles of flying grease.

In summary, the image sequence of the impact experiment has a lower number of frames per experiment leading to a more significant difference between the two subsequent images, a lower resolution, and a higher noise in comparison with the quasi-static measurements.

4.8.3 Data processing and evaluation

The high-speed camera images captured during the experiment are initially stored in the native camera data format enabling their post-processing in the standard manufacturer's software (Photron FASTCAM Viewer, Photron, Japan). Prior to the processing by the DIC algorithm, the image sequence is converted to PNG raster-graphics file-format using a loss-less conversion. Then, the image sequence is loaded in MATLAB software. Depending on the image quality and noise, the images are adjusted using pre-processing techniques (e.g., Gaussian blur, crop to the region-of-interest, zero padding on the edges of the image) to improve the image correlation convergence and accuracy. Then, a grid of correlation points is placed onto the surface of the object in the image. The grid is established in the representative and well defined points of the object, e.g., nodes of the lattice structure. Commonly, a pseudo-random artificial black and white speckle is mounted on the ends of the measurement bars. The artificial pattern is used to track the displacement of the bars at the boundaries of the specimen. Other correlation points are created in the well-defined parts of the specimen (e.g., nodes of the lattice structure, see Fig. 4.41). If necessary, the surface of the specimen is adapted for the image correlation by spraying the surface using a multi-color air brush or spray with a granite effect. After the creation of the grid of correlation points, the algorithm parameters (offset, size of the correlation subset) are set to the optimal values for the given experiment and the DIC is started.

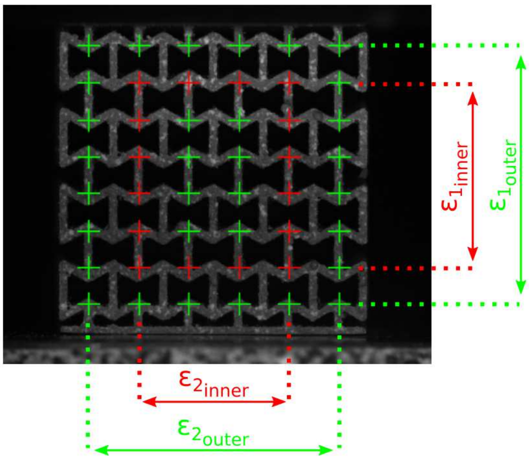

Figure 4.41: The grid of correlation points on the specimen's surface.

A set of MATLAB functions for the post-processing of the evaluated displacements was developed and can be used for the analysis of the results and comparison with the strain-gauges data [3]. The scripts can be employed for the direct synchronization of the image sequence with the strain-gauges data. The synchronization signal is produced by the experiment triggering system described in detail in Section 4.6. Therefore, the individual images can be directly paired with the strain-gauges signal with the precision of a few microseconds (see Fig. 4.42). Other scripts for evaluation of, e.g., image correlation based stress-strain diagram, strain-rate or Poisson's ratio have been developed, too.

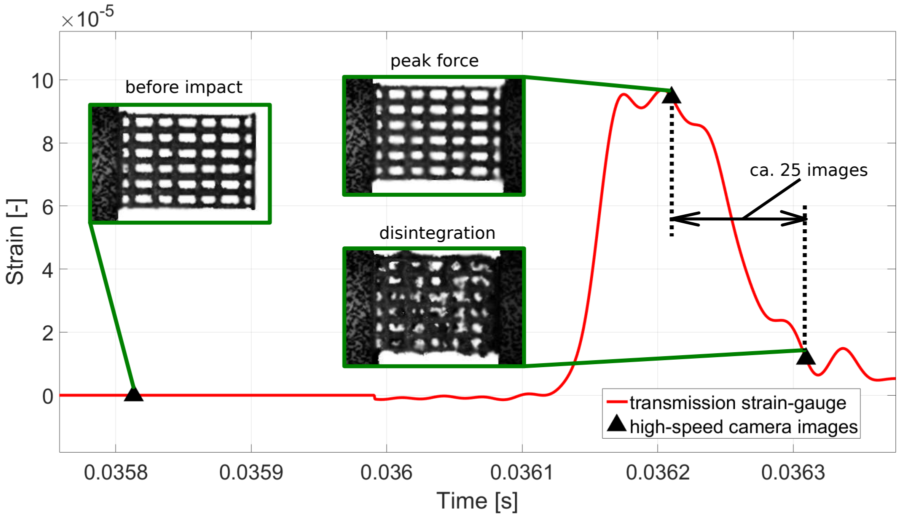

Figure 4.42: The high-speed camera images synchronized with the strain-gauge data. The images represent the important states during the impact compression of the brittle polymer auxetic structure (intact specimen, maximum force and undergoing disintegration).

4.8.4 DIC based calibration - comparison with strain-gauges

DIC can be effectively employed for the calibration of the experimental setup or can serve as a data redundancy for the experiment, during which a strain-gauge was lost (e.g., peeling off the strain-gauge during the experiment).

Displacement based calibration

For the calibration of the setup, the displacements of the bar's ends during a void test evaluated using the strain-gauges signals and by the DIC are compared. A straight line or grid of correlation points is defined in the pseudo-random pattern mounted on the bars. The longitudinal displacement $u_{\mathrm{sg}}(t)$ of the free bar's end using the strain-gauge signal is given by

$$u_{\mathrm{sg}}(t) = \int_0^t c_0 \cdot \epsilon_{\mathrm{end}}(t)\mathrm{d}t, \tag{4.32}$$

where c_0 is the wave propagation velocity and $\epsilon_{\mathrm{end}}(t)$ is the measured strain-gauge signal time-shifted to the end of the bar. The longitudinal displacement $u_{\mathrm{dic}}(t)$ of the free bar's end using the image correlation signal is given by

$$u_{\mathrm{dic}}(t) = PS \cdot x(t), \tag{4.33}$$

where PS is the effective pixel-size and $x(t)$ is the time series of the displacement averaged per all the relevant correlation points. Analogically, the method can be used for the comparison of the displacements and the nominal strain of the specimen during the experiment. The comparison of the strain-gauge and the DIC displacement (strain) in the selected experiment is shown in Fig. 4.43.

Velocity based calibration

The results can also be compared not in terms of displacement but rather particle velocity. This approach is beneficial and provides better precision when compared to the previous method as the particle velocity from the strain-gauge is compared with the differentiation of the DIC displacement.

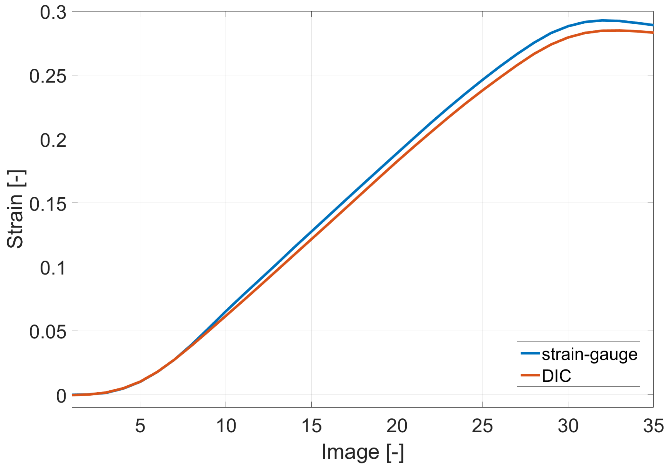

Figure 4.43: The comparison of the strain-gauge and the DIC strain in the selected experiment.

Therefore, the sensitivity of the method is rather high. Here, the particle velocity $v_{\text{sg}}(t)$ from the strain-gauge is given by

$$v_{\text{sg}}(t) = c_0 \cdot \epsilon_{\text{end}}(t). \tag{4.34}$$

The average particle velocity $v_{\text{dic}}(t)$ using DIC is defined as

$$v_{\text{dic}}(t) = PS \cdot \dot{x}(t), \tag{4.35}$$

where $\dot{x}$ is the differentiation of the time series of the displacement averaged per all relevant correlation points. For calibration purposes, the correlation results have to be of high quality with the reliable tracking of the correlation points. In this case, for both the aforementioned methods, the difference between the DIC and strain-gauges has to be maximally in range of a few percent. If it is not the case, this indicates a problem in the experimental setup or in the evaluation of the results. The comparison of particle velocity calculated using the strain-gauges and the DIC is shown in Fig. 4.44.

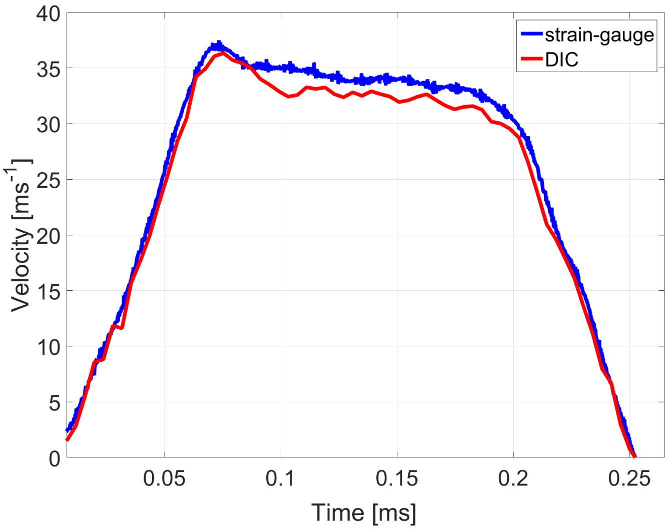

Figure 4.44: Comparison of particle velocity calculated using strain-gauges and DIC.

Striker bar impact velocity

Besides the displacement and strain evaluation in a deformed sample, DIC can be employed for the evaluation of the striker bar impact velocity. This method is fundamental for the evaluation of the direct-impact OHPB experiments as the initial impact velocity directly affects the calculated deformation of the specimen (further reading in Section 4.9, Eq. 4.40) and, therefore, it has to be evaluated with a high precision. Similarly, as in the case of the particle

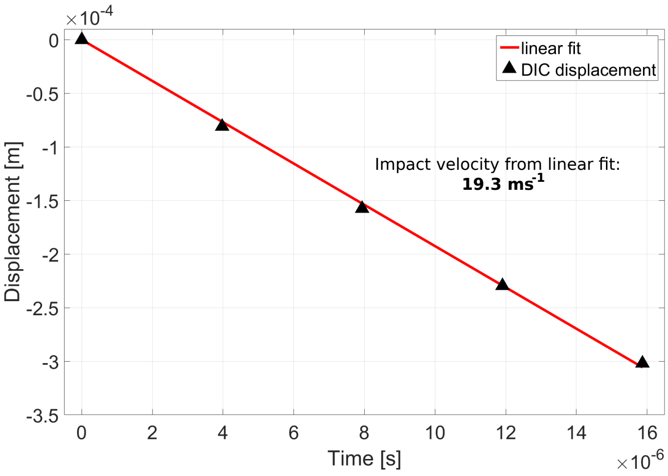

Figure 4.45: The striker bar impact velocity evaluated using the DIC.

velocity calculation, the striker impact velocity can be calculated from the DIC displacements. Here, a method of linear regression was found to be a good approach to evaluate the impact velocity (see Fig. 4.45).

4.8.5 DIC accuracy and reliability

A high degree of reliability of the DIC results was achieved in the majority of the quasi-static and dynamic experiments. The typical overall mean correlation coefficient was higher than 90 % representing the reliable tracking of the correlation points even for the large values of deformation (20 – 30 %). Moreover, the displacement paths of the individual tracked points were optically inspected to reveal a possible loss of correlation or a sudden change in the point's position. In all the cases, the vast majority of the grid points exhibited continuous displacement paths up to the densification of the specimen. A loss in the correlation occurred only in a limited extent and only for a few correlation points particularly located on the edges of the specimen. The typical values of the mean correlation coefficient throughout the grid plotted against the strain, and the example of the correlation grid in the representative states of deformation (no deformation, auxetic behavior, and densification) of the 2D re-entrant honeycomb are shown in Fig. 4.46. The tracking results started to be unreliable during the initial phase of the densification of the structure. Note that the mean correlation coefficient in Fig. 4.46 reached its minimum at the strain of approximately 38 %. From this point, it seemingly increased and reached values above 0.9 again. However, this effect was identified, not as the restoration of the tracking precision, but as the misidentification of the correlation points in the densified structure. The incorrectly identified positions of a limited number of points can be found even in the image corresponding to the strain of approximately 35 % (see Fig. 4.46, blue color frame). In some experiments, the mean correlation coefficient exhibited a different behavior and tended to oscillate after reaching the densification phase revealing the loss of the correlation in the crushed structure. This behavior was similar to the analysis performed on the hybrid nickel-polyurethane foams [137]. When DIC was used for the evaluation of Poisson's ratio (see Section 5.4 and 5.15.2), the values of Poisson's ratio in the very low strains (up to ca. 3 %) exhibited large numerical errors as the low values of the lateral strain were divided by the low values of the longitudinal strain. Moreover, in the dynamic experiments, the values were also affected by the ramp-in effects of the strain wave and by its propagation through the sample in the initial phase of impact. Thus, dramatic changes in Poisson's ratio at the low strain apparent in the graphs were caused by the aforementioned errors and were not connected with the deformation behavior.

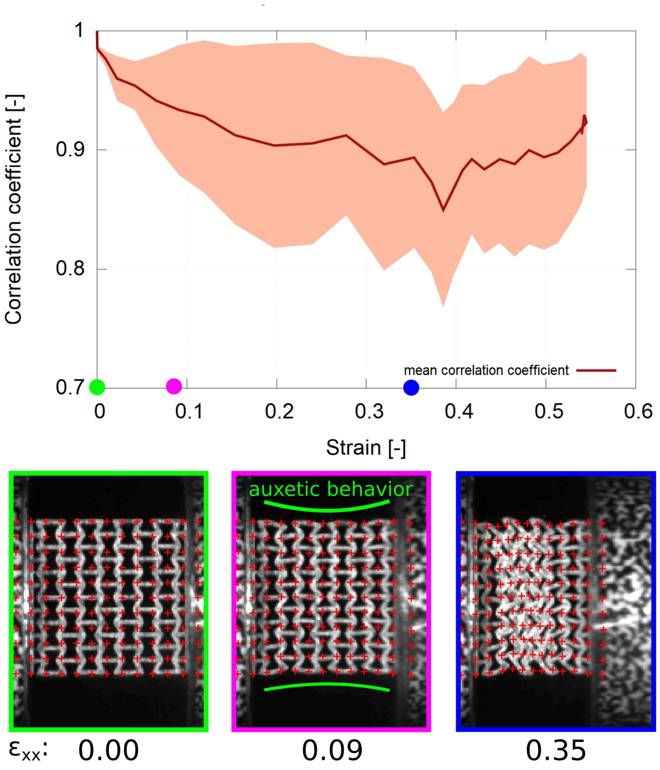

Figure 4.46: The mean correlation coefficient throughout the grid plotted against the strain with the highlighted representative states of deformation (no deformation, auxetic behavior, and densification) of the 2D re-entrant honeycomb structure.

4.9 OHPB - advantageous method for high strain-rate testing of meta-materials

The OHPB is a novel method for the high strain-rate testing based on the direct impact Hopkinson bar variants [145, 146]. It was first introduced by Govender [146] in 2016. However, the arrangement of the experimental setup published in the contribution exhibited limited performance. In our laboratory, a different physical representation of the OHPB method with a higher performance has been developed and tested. The results measured using the OHPB method are reliable, directly comparable with the SHPB method, and are of high quality. Therefore, the realized OHPB experimental setup is considered as one of the main achievements in this study.

4.9.1 SHPB limitations - why OHPB?

The SHPB has limited performance for testing of soft cellular materials, where high strains together with a wide spectrum of strain-rates is required for the relevant description of the deformation behavior. The main limitations are summarized in the following list:

- The strain in the specimen is directly proportional to the length of the striker and its impact velocity. Therefore, a high specimen strain has to be achieved using the high impact velocity (higher strain-rate) or long striker bar or by a combination of both. As the maximal striker bar length is physically limited by friction, the dimensional tolerances of the bar and performance of the gas-gun, the SHPB has its minimum strain-rate limit.
- The duration of the experiment is constrained by the wavelength of the strain wave pulse and the wave propagation velocity. Thus, the SHPB experiment has to fit into a short time window.
- In the case of the cellular materials, the amplitudes of the incident pulse, reflected pulse and transmission are highly disproportional as

the transmission pulse strain is often very low (many times lower than the pulses in the incident bar). The large disproportion between the amplitudes of the incident bar pulses and the transmission bar pulse can cause noisy oscillations hiding the true state of the force equilibrium or can even cause its violation.

- The wave superposition of the oppositely propagating strain waves makes the evaluation of the results from the strain-gauges mounted close to the specimen uneasy.
- According to the standard theory, the SHPB experiment is only valid during the period of the force equilibrium and the equations for the evaluation of the results are derived according to this assumption.
- Measurements using low-impedance visco-elastic bars require advanced correction method of the wave dispersion effects, while the corrections are still reliable and valid only under certain circumstances (this is discussed in more detail in Section 4.10).

The OHPB method has been designed to overcome the aforementioned problems. The technique exhibits several advantages and benefits over the SHPB, particularly in the testing of soft cellular materials. However, it is necessary to mention that the method is not, in general, superior to the other Hopkinson bar techniques and also has its disadvantages. As in the other cases, the experimental setup and parameters of the experiment have to be properly tuned and have to stand within the application envelope of the method.

4.9.2 OHPB principle

The principle of the OHPB method is directly derived from the direct impact Hopkinson bar methods. The scheme of both the forward and reverse direct impact Hopkinson bar methods [146] and the OHPB is shown in Fig. 4.47. Note that in the forward and reverse direct impact Hopkinson bar, only the transmission bar is instrumented with a strain-gauge.

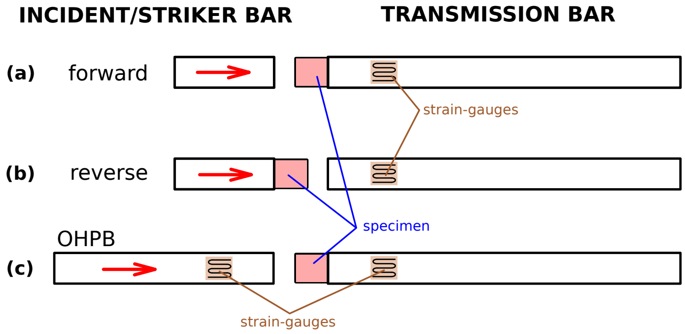

Figure 4.47: The principle of the (a) forward and (b) reverse direct impact Hopkinson bar method and (c) the OHPB.

The OHPB consists of two measurement bars (incident and transmission) both instrumented by strain-gauges. The incident bar is inserted in the barrel of the gas-gun and also serves as the striker bar. The specimen is mounted on the impact face of the transmission bar. During the experiment, the incident bar is accelerated using the gas-gun and directly impacts onto the specimen. By the compression of the specimen, the strain wave pulses are generated in both bars. Both pulses propagate from the specimen to the free ends of the bars. Then, the pulses are reflected on the free ends and propagate back to the specimen. The experiment ends (in the simplest representation) when the backward-propagating waves reach the strain-gauges, thus, producing superposed signals. As the waves propagate from the specimen, they have an approximately identical shape. The beginning of the transmission pulse is delayed in comparison with the incident pulse as the strain wave has to pass through the specimen (similarly to the SHPB).

Using the strain-gauge signals, one can calculate the forces and displacements on the respected faces of the measurement bars [146]. The time-shifting procedure of the signals is identical as in the case of SHPB (see Section 4.7). The forces on the incident face $F_{\mathrm{in}}(t)$ and on the transmission face $F_{\mathrm{out}}(t)$ can be calculated according to the relations

$$F_{\mathrm{in}}(t) = A_{\mathrm{in}} \cdot E_{\mathrm{in}} \cdot \epsilon_{\mathrm{in}}(t), \tag{4.36}$$

$$F_{\mathrm{out}}(t) = A_{\mathrm{out}} \cdot E_{\mathrm{out}} \cdot \epsilon_{\mathrm{out}}(t), \tag{4.37}$$

where A_{in}, A_{out} represent the cross-sectional area of the bars, E_{in}, E_{out} represent Young's modulus of the individual bars and $\epsilon_{\mathrm{in}}(t)$, $\epsilon_{\mathrm{out}}(t)$ are the measured strain-gauge signals. The particle velocities $v_{\mathrm{in}}(t)$, $v_{\mathrm{out}}(t)$ at the ends of the bars can be represented using the relations

$$\begin{aligned} v_{\mathrm{in}}(t) &= C_{0_{\mathrm{in}}} \cdot \epsilon_{\mathrm{in}}(t), && (4.38) \\ v_{\mathrm{out}}(t) &= C_{0_{\mathrm{out}}} \cdot \epsilon_{\mathrm{out}}(t), && (4.39) \end{aligned}$$

where $C_{0_{\mathrm{in}}}$ and $C_{0_{\mathrm{out}}}$ are the wave propagation velocities in the bars. By adopting the aforementioned formulas, the specimen's strain-rate $\dot{\epsilon}_{\mathrm{s}}$ and the distance between the bars (or actual specimen length) $l_{\mathrm{s}}(t)$ are given by

$$\begin{aligned} \dot{\epsilon}_{\mathrm{s}}(t) &= v_0 - C_{0_{\mathrm{in}}} \cdot \epsilon_{\mathrm{in}}(t) - C_{0_{\mathrm{out}}} \cdot \epsilon_{\mathrm{out}}(t), && (4.40) \\ l_{\mathrm{s}}(t) &= l_0 - \int_0^t \dot{\epsilon}_{\mathrm{s}}(t) \mathrm{d}t = && (4.41) \\ &= l_0 - \int_0^t \left[v_0 - C_{0_{\mathrm{in}}} \cdot \epsilon_{\mathrm{in}}(t) - C_{0_{\mathrm{out}}} \cdot \epsilon_{\mathrm{out}}(t)\right] \mathrm{d}t, \end{aligned}$$

where l_0 is the initial length of the specimen and v_0 is the initial impact velocity. Note that the evaluation of the actual length of the specimen (strain) is strongly dependent on the initial impact velocity v_0. Thus, in the OHPB, it is crucial to measure the velocity with high precision, unlike in the SHPB method, where the impact velocity serves as a secondary parameter useful for the verification of the results.

4.9.3 Evaluation of the OHPB experiment

The evaluation of the OHPB experiment is, in principle, similar with the SHPB method. The processing of the experiment can be summarized in the following points:

- Importing the variables and measured data.
- Conditioning the strain-gauge signals (filtration, offset etc.).
- Selection of the incident and transmission pulses.
- Time-shifting the pulses.
- Evaluation of the results using the theory described in the previous Section 4.9.2.

For most of the pre-processing steps, the existing MATLAB functions described in Section 4.7 are suitable and can be directly used. For the final evaluation of the OHPB experiments, the supplementary MATLAB functions have been developed and are included in the thesis as an attachment (See Appendix B).

Simplification - time-shifting

When the material, diameter and length of both the incident and the transmission bar are identical, the transmission and incident strain-gauges are mounted at exactly the same distances from the impact faces, and the specimen deforms plastically, a simplified approach for the time-shifting of the strain waves can be employed. In this case, the wave propagation time from the specimen's boundary to the strain-gauge is the same for both bars. Moreover, any wave dispersion effects can be considered negligible as the waves are smoothed and filtered by the plastic deformation of the specimen. Any superposition of the forward and backward-propagating waves would occur at the same time. Thus, it is not necessary to perform the time-shifting procedure nor the conditioning of the pulses and the experiment can be evaluated directly using the recorded signals. If necessary, the treatment of the signal noise (filtration) or a minor shift to correct the misalignment of the strain-gauges can be performed prior to the evaluation.

4.9.4 Design of the OHPB

A different arrangement of the OHPB method has been developed than the apparatus described in [146]. In our configuration, the incident bar is not fully loaded in the gas-gun, but its frontal part containing the mounted strain-gauges is always out of the barrel. The alignment of the bars is not performed by the axis of the gas-gun, but by a linear guidance system. The performance of the method has been increased by the maximization of the stroke of the gas-gun. The original SHPB experimental setup, described in detail in Section 4.5, has been adapted for the OHPB method and all the major parts of the SHPB setup are identical with the OHPB version. Therefore, the SHPB and OHPB experimental arrangements are compatible and one version of the setup can be relatively easily modified to the other version. Thus, one can use the version of the setup, optimal for a given type of specimen, on a single frame. The scheme of the OHPB setup including the major parts of the instrumentation is shown in Fig. 4.48. The overview of the OHPB experimental setup is shown in Fig. 4.49.

Gas-gun

The identical gas-gun as described in Section 4.5 is used for the OHPB method. However, the system for loading the striker bar is not used in this variant as the incident bar is loaded manually into the barrel.

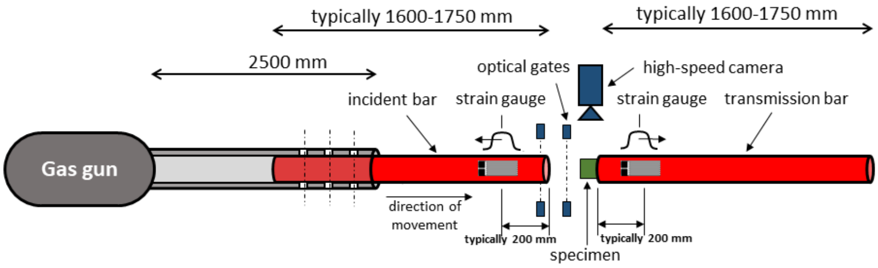

Figure 4.48: The scheme of the OHPB setup including the major parts of the instrumentation.

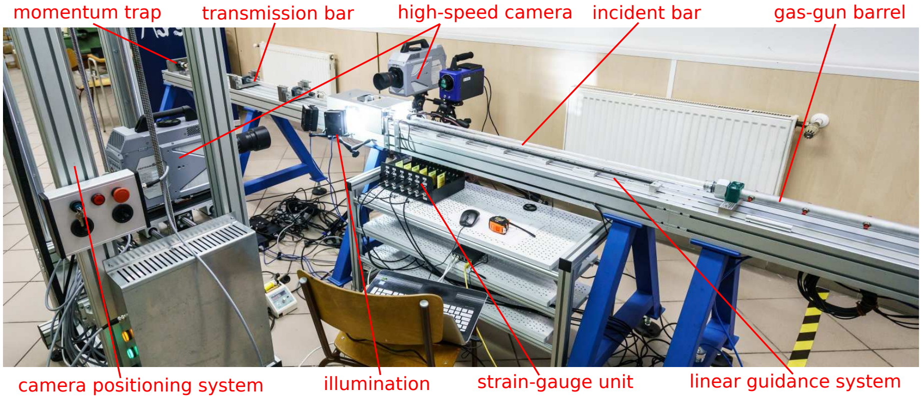

Figure 4.49: The overview of the OHPB experimental setup.

Incident bar and linear guidance system

In our laboratory, the length of the incident bar is usually selected in the range of 1500 – 1800 mm. The back-end of the incident bar is loaded in the gas-gun barrel while the front-end is carried by a linear guidance system. The strain-gauges are mounted in the frontal part of the incident bar at a typical distance of 200 mm from the impact face. The linear guidance system is mounted in front of the strain-gauges. The system consists of a friction clamp, a polymeric or aluminum alloy flange, a linear guide carriage (DryLin T, TW-04-12, IGUS, Germany) with a sliding polymeric liner, and a linear guide rail with a length of 1400 mm mounted on the main frame profile using a set of fixtures. The incident bar launch system is shown in Fig. 4.50.

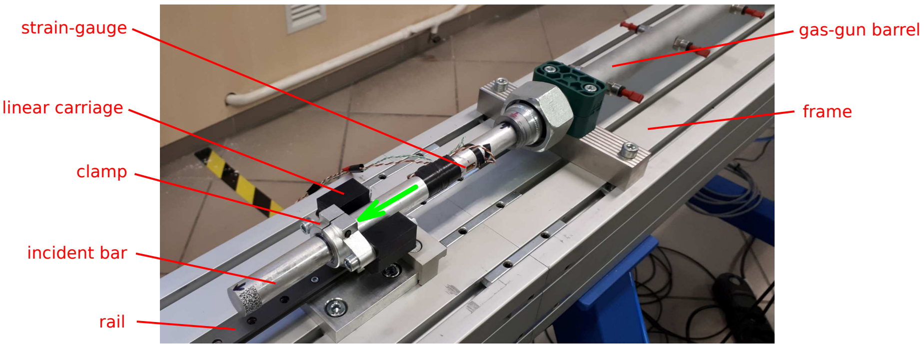

Figure 4.50: The OHPB incident bar launch system.

Other parts of the setup

The other parts of the experimental setup are identical to the SHPB setup. The specimen is mounted on the transmission bar using a small amount of grease and natural friction. The specimen mounted in the OHPB and the other parts of the setup are shown in Fig. 4.51.

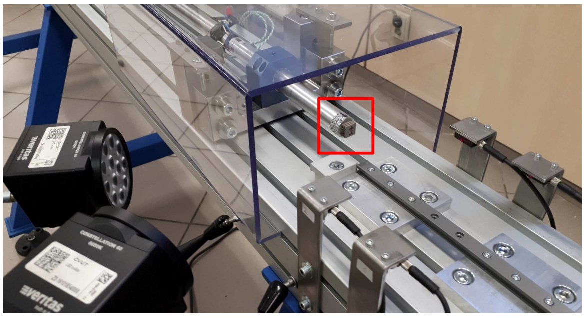

Figure 4.51: The specimen mounted in the OHPB and the other parts of the setup.

OHPB instrumentation

The instrumentation of the OHPB experiment is, in principle, identical to the SHPB experiment. All parts of the instrumentation summarized in Section 4.6 have been straightforwardly adapted for the OHPB method. However, some differences exist in the actual arrangements:

- The optical gates are mounted as close to the specimen as possible to trigger the experiment precisely as a longer deformation time requires a tight triggering to capture the whole experiment.
- The optical gates are mounted as close to each other as possible to estimate the initial impact velocity with sufficient precision. The friction of the incident bar decreases as it is being pushed-out of the barrel. Thus, the acceleration at the end of the stroke is very rapid and no correction method for the estimation of the initial impact velocity is sufficient.
- The high-speed camera is always used to record the pre-impact phase of

the experiment and to capture the movement of the incident bar. DIC is then used for the precise evaluation of the initial impact velocity.

- As the incident bar is used as a striker, the moving mass impacting the specimen is usually higher than in the SHPB. Moreover, the residual energy after the experiment is not dissipated over time in a series of waves propagating in the bars (prior to the collision with the momentum trap). As a result, the momentum trap of the OHPB setup is usually more stressed than in the SHPB experiment.

OHPB calibration

The strain-gauges in the OHPB are quasi-statically calibrated using the same procedure described in Section 4.6.3. The bars apart and bars together void tests are used for the evaluation of the dynamic properties of the bars. In this case, a small striker is loaded in the gas-gun barrel and impacts the incident bar face directly inside the barrel. Finally, a direct impact void test is employed. During this void test, the standard OHPB experiment is carried out without any specimen. The recorded strain waves from both bars are recorded and compared. As in the case of the SHPB, all the differences should be in the range of a few percent, if not, this indicates a problem in the experimental setup.

Performance

Using the maximum compressor pressure of $1\,\mathrm{MPa}$, the gas-gun system is capable of accelerating the aluminum alloy incident bar with a length of $1600\,\mathrm{mm}$ to the maximum impact velocity of approx. $18-20\,\mathrm{ms^{-1}}$ and the lighter polymeric PMMA bar with a length of $1750\,\mathrm{mm}$ to the maximum impact velocity of approx. $25{-}30\,\mathrm{ms^{-1}}$. With this performance, the maximum achievable strain-rate using the OHPB method is at the bottom range of the strain-rates achievable by the SHPB. Thus, the method can be beneficially used for testing at the strain-rates between the drop-weight test and the SHPB.

Our gas-gun system can be pressurized up to the maximal design pressure of 1.6 MPa using, e.g., a compressed air bottle. This approach can increase the aforementioned maximum velocities by approx. 25 %. However, this method has not been tested until to the finalization of the thesis.

The lower strain-rate in the OHPB test is defined predominantly by the mass of the striker bar. As the impact energy is proportionally dependent on the impacting mass and on the squared impact velocity, the impact energy decreases dramatically with the lower impact velocities (if the incident bar mass remains the same). With a smaller energy margin in the experiment, the strain-rate dramatically drops as the specimen is able to absorb a significant amount of the impact energy.

4.9.5 Advantages and disadvantages

The OHPB exhibits several advantages over the SHPB and the direct impact Hopkinson bar methods, but is also limited by several disadvantages. The advantages are summarized in the following list:

- Higher achievable strain of the specimen in comparison with the SHPB with the same overall length of the setup.
- Long duration of the experiment prior to the wave superposition in comparison with the SHPB with the same overall length of the setup.
- Approximately identical signals measured in both bars.
- Strain-gauge signals are measured very close to the specimen without signal superposition.
- Strain waves are almost without any wave dispersion effects as the wavelength and frequency bandwidth correspond with the behavior of the specimen.
- Low noise of the signals caused by the parasitic oscillations in the setup.

- Strain-rate range in between the typical strain-rates achieved by the drop weight test and SHPB test.
- Reliable measurement of the incident and transmission bar signals. Strain wave information from both sides of the specimen.
- Easier calibration and geometrical adjustment of the setup.
- Good quality dynamic equilibrium.
- Easier processing of the signals and evaluation of the results.
- Low or no effects of the visco-elastic bars (see Section 4.10).

The main disadvantages are summarized in the following list:

- A more complex system.
- More difficult alignment of the bars at higher impact velocities. Susceptibility to bending, particularly with soft polymeric visco-elastic bars.
- More difficult dissipation of the residual impact energy.
- More difficult mounting of the specimen.
- Decreasing impact energy with the decreasing impact velocity can lead to the dramatically dropping and unstable strain-rate during the experiment.
- Testing at high strain-rates, comparable with the upper strain-rates of SHPB, would be complicated and would require a very complex setup.
- Impact velocity has to be measured directly and with high precision using, e.g., DIC.

The OHPB method has been found to be very beneficial and suitable for the testing of cellular materials under high strain-rates. However, it is not generally superior to the other Hopkinson bar methods and, depending on the specimen and strain-rate, its parameters have to be properly tailored for the desired application.

4.10 Measurement using visco-elastic bars

The high performance aluminum alloy EN-AW-7075-T6 has been identified as a material suitable for the measurement of cellular meta-materials using the Hopkinson bar method. With a nominal Young's modulus of approx. 70 GPa and wave propagation velocity of approx. $5100\,\mathrm{ms}^{-1}$ its mechanical impedance is significantly lower than that of steel (Young's modulus approx. 3× higher). Using the experimental setups described in the previous sections and bars with a diameter of 20 mm, it was possible to reliably detect forces as low as approx. 1000 N. For lower forces, however, it has been necessary to use bars with an even lower mechanical impedance. In this case, polymeric bars made of polymethyl methacrylate (PMMA - known as plexiglass) have been used. With a nominal dynamic modulus of approx. 5.5 GPa and a wave propagation velocity of approx. $2100\,\mathrm{ms}^{-1}$, it has been possible to reliably detect forces as low as $50 - 100\,\mathrm{N}$. However, the mechanical behavior and wave propagation of the PMMA cannot be described using a simple linear elastic model as the material exhibits strong visco-elasticity and wave dispersion. Thus, more advanced wave dispersion correction methods for the signal processing in the frequency domain have to be applied (see Section 4.7.3).

4.10.1 Wave propagation in visco-elastic bars

In linear elastic bars, the signal attenuation can be considered negligible unless the wave propagation distances are very long (approx. $> 10\,\mathrm{m}$). The phase delay of the individual frequencies affecting the wave shape and causing Pochhammer-Chree oscillations is important in order to reconstruct the behavior on the specimen's boundaries. However, this effect can be minimized using a pulse-shaping technique. For such a case, the phase delay can also be considered negligible. Thus, the time-shifting of the signals in the linear elastic bars is rather simple and the methods for the wave dispersion analysis [112] (see Section 4.7.3) are primarily used for the calculation of the actual material properties of the bars and for calibration purposes.

However, this simple approach cannot be adopted for the experiments with the PMMA visco-elastic bars. Here, both the attenuation and phase delay of the individual frequencies cannot be considered negligible and have to be

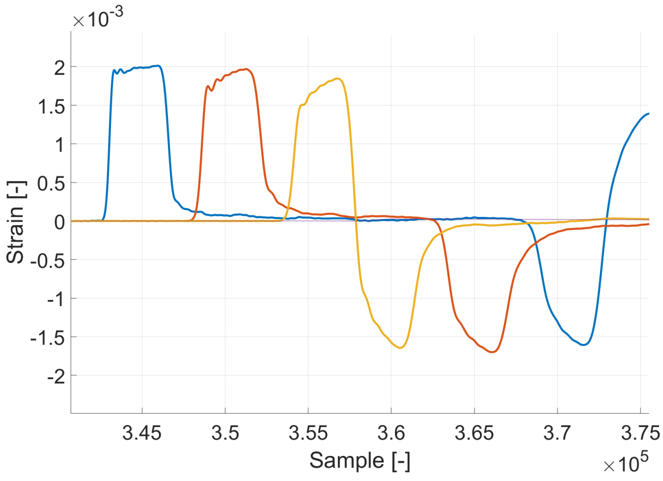

Figure 4.52: The typical strain-gauges data showing wave propagation in the visco-elastic bars. Note high attenuation and changes of the wave shape.

taken into account. Thus, an advanced time-shifting procedure has to be performed fully in the frequency domain using the experimentally evaluated wave propagation coefficient (see Eq. 4.27). By adopting the frequency domain based reconstruction of the signal together with visco-elastic material model, it is possible to reconstruct the signal at a certain point of the bar. The strain wave pulse propagating in the PMMA visco-elastic bar measured at the different points of the bar using the strain-gauges is shown in Fig. 4.52. The strain pulses measured by the two strain-gauges time-shifted to the same point at the bar using the aforementioned frequency domain method is shown in Fig. 4.53.

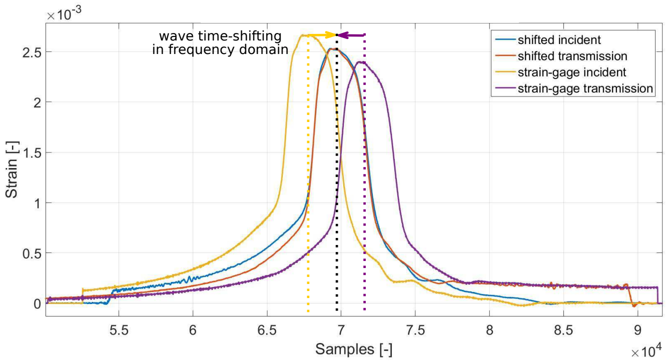

Figure 4.53: The strain pulses measured by the two strain-gauges time-shifted to the identical location at the bar using the frequency domain method.

4.10.2 SHPB

In the SHPB with the PMMA bars, the use of the visco-elastic material correction model in the frequency domain is a key requirement for reliable results. The strain waves traveled distances are always relatively long in the SHPB as the pulses have to travel at least through the whole length of the incident bar. Here, the wave dispersion effects are apparent and cause a significant wave distortion, attenuation and the increase in the wavelength. Thus, for the SHPB experiments, the following scheme for calibration has been adopted:

1. The quasi-static calibration of the experimental setup with quasi-static material parameters.
2. A series of bars apart void tests with short strikers ($50 - 200\,\mathrm{mm}$) for the evaluation of the propagation coefficient and the visco-elastic material properties in the incident bar.
3. A series of bars together void tests with short strikers ($50 - 200\,\mathrm{mm}$) for the evaluation of the propagation coefficient and the visco-elastic material properties in the transmission bar and through the bar-to-bar interface.
4. A series of bars apart and bars together void tests with the striker used in the experiments (typically $300 - 500\,\mathrm{mm}$) for the evaluation of the propagation coefficient of longer wavelengths.
5. The calculation of the average propagation coefficient and material properties combining the data for the short and long wavelengths.
6. A series of bars apart and bars together void tests to test the time-shifting procedure (time-shifted signals compared with the signals measured using the other strain-gauges).
7. If necessary, the modification of the propagation coefficient for the better fit to the experimental data.
8. Experiments with the specimens.

If the setup is used multiple times for a longer period of time (more than 1 month), the calibration procedure has to be repeated as the visco-elastic bars, in general, can absorb limited amount of moisture and, depending on the material type, environment and circumstances, can slightly change their material properties (affecting the evaluated results). In this study, only minor negligible differences caused by the environment were observed over time. However, after a series of high velocity impacts, the PMMA often suffered from micro-cracking requiring a repair or the replacement of the bars. Moreover, the correction methods, described in the previous sections, only work reliably when the time-shifting of the signals is performed for relatively short distances (approx. $< 1000 - 1500\,\mathrm{mm}$). Otherwise, the distortion of the signals is severe and their reliable reconstruction is not possible. The material properties and propagation coefficient should be evaluated for both bars separately as there may be significant differences. The transfer function at the end of the bars also has to be taken into account. The evaluation of the SHPB experiment performed with the visco-elastic bars is, therefore, a complex task and careful analysis of the results has to be performed.

4.10.3 OHPB

The time-shifting procedure of the OHPB data is, in principle, identical to the SHPB data. However, if the following conditions are met, the evaluation of the OHPB results can be significantly simplified:

- Both OHPB bars have the same length and diameter.
- The strain-gauges on both bars are mounted at the same distance from the impact face.
- The strain-gauges are mounted at the maximal distance of approx. 20× diameters from the impact face to limit the wave travel distance.
- The deformation of the specimen is plastic producing long wavelengths and smooth signals (naturally filtered, almost without a wave dispersion).

Under the aforementioned conditions, the following approach for the time-shifting of the signals can be used:

- No time-shifting of the signals is necessary as the wave propagation time from the impact face is equal for both bars.
- No propagation coefficient and correction of the wave-shape are necessary as the strain pulses have a long wavelength and are almost free of dispersion effects.
- The forces and particle velocities can be calculated using the complex modulus and wave propagation velocity evaluated experimentally for the long wavelengths (for low frequencies the complex modulus and wave propagation velocity are almost constant).

The comparison of the OHPB signal time-shifted using the visco-elastic model in the frequency domain with a simply-shifted signal processed using the aforementioned method and with a signal measured in the corresponding point using a strain-gauge is shown in Fig. 4.54.

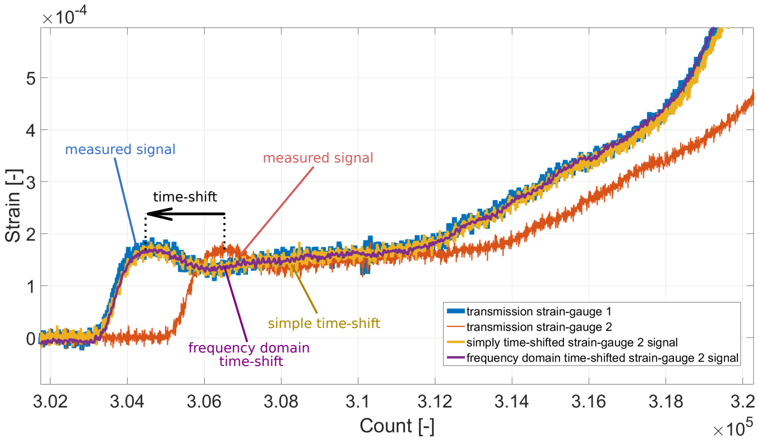

Figure 4.54: The comparison of the OHPB signal (red) time-shifted using the visco-elastic model in the frequency domain (violet) with a simply-shifted signal processed using the aforementioned method (yellow) and with a signal measured in the corresponding point using strain-gauge (blue).

4.11 Supplementary methods

Additional methods, that were used in the selected experimental campaigns, are briefly described in this section. Supplementary methods were applied to obtain additional data about the deformation behavior of the specimens, and as an enhancement to the experimental techniques. The most important supplementary methods employed in the experiments were: (i) high-speed thermography, (ii) testing at elevated temperatures using a heating stage, and (iii) testing at low temperatures using a cooling stage. The supplementary methods are described only briefly as an overview of the combined and complex testing that have been employed for the analysis of the cellular materials and their constituents.

4.11.1 High-speed thermography

Heat related phenomena during impact loading are well known effects causing, e.g., strain-rate related softening of the material. The thermal response of the samples during the impact, heat transfer, and heat dissipation effects were observed using the thermal imaging camera (SC7600, Flir, USA) equipped with an actively cooled focal plane array (FPA) with a full-frame resolution of 640×512 px and a pixel pitch 15 μm. The camera was attached to a 50 mm f/2 lens with an anti-reflection coated silicon based optics. The camera uses a photon counting Indium Antimonide (InSb) detector operating in the $1.5 - 5.1\,\mu$m spectral range (SWIR to MWIR band). The lens-camera assembly was calibrated for the temperature range from $-20\,°$C to $300\,°$C, where the thermal response of the samples to the loading was anticipated. To achieve the maximum possible frame-rate at a reasonable resolution, the FPA windowing to 96×44 px was used to perform the imaging at approx. 2 kfps for the room and elevated temperature experiments, while the cooled samples were observed at approx. 1.9 kfps given by the integration time necessary for the imaging of the samples at such low temperatures. During all the experiments, an MgF_2 infrared-transparent protective window was used to guarantee the safety of the thermal imaging optics. For verification of the cooling procedure and the sensitivity of the high-speed thermal-imaging camera, a microbolometric LWIR thermal imager i7 (FLIR, USA) was used.

In all the experiments, it was possible to capture only a limited number of the infrared images of a sample undergoing deformation. According to the obtained results, the thermograms could be successfully used for the identification of the stress-concentration regions. This also opened possibilities for the analysis of the friction-effects on the bar-specimen boundary that are crucial for the numerical simulations of the experiments, where finding appropriate models and constants for the frictional boundary effects is a very challenging task. Note that only a qualitative analysis of the heat distribution could be provided as the precision of the thermal imaging in this temperature range has inherent physical limitations because the photon counting detector is used for the thermal imaging. Here, the quality of the images is affected by a limited amount of photons emitted by the specimens in the spectral range of the detector, while the required maximum frame rate influences the necessary integration time yielding uncertainties and a low signal-to-noise ratio in the observed temperature range. An example of the experimental setup with the infra-red camera installed is shown in Fig. 4.55.

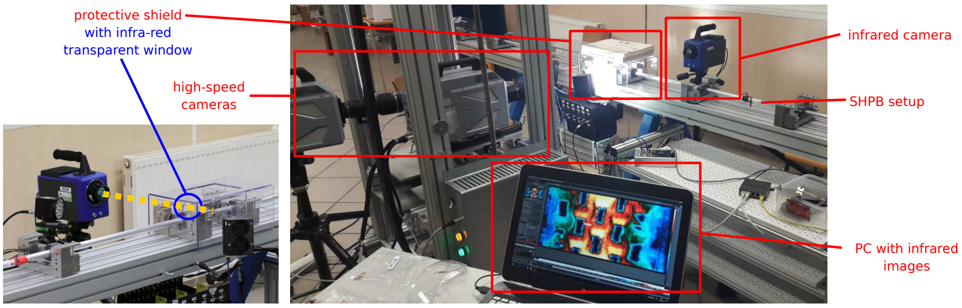

Figure 4.55: An example of the experimental setup with an infra-red camera.

4.11.2 Heating-stage

The heating setup consisted of two pairs of the ceramic heating elements, each having an energy input of 40 W, that are commonly used for construction of HotEnds (printing heads of thermal-based 3D printers). The heating elements were placed into movable aluminum clamps to provide proper contact with the heated specimens. Movement of the clamps was provided by two independently regulated (RC) servo drives controlled by the in-house developed electronics. The temperature was regulated by an open-loop control system using a pulse-width modulation signal to achieve the desired temperature of the sample up to approx. 220 °C. To warm up the specimen, the heating clamps were set in contact with the upper and bottom face of the specimen prior to the experiment. After the target temperature had been reached, the clamps were commanded to move away from the specimen and the SHPB experiment was started. The heating stage was developed by team member Jan Šleichrt. The stage is shown in Fig. 4.56.

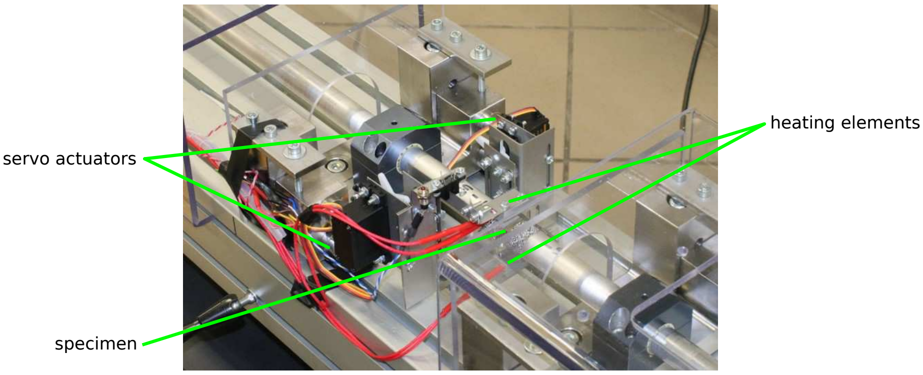

Figure 4.56: The heating stage mounted in the SHPB setup.

4.11.3 Cooling-stage

The cooling setup was designed as a gas cooling system with carbon-dioxide as an active medium. From a pressure vessel with a volume of 6.7 l containing 5 kg of liquid carbon-dioxide, gas was released through a reduction valve at 15 bars and fed through a silicon low-temperature certified hose into the cooling stage. The cooling stage was composed of a thermally isolated cooling box containing dry ice, i.e., carbon dioxide in a solid state with a temperature of −78 °C, and another smaller vessel filled with a combination of dry ice and 1 l of pure ethanol. The silicon hose from the pressure vessel was led in the first instance through the dry ice and then through the cooled ethanol vessel. The lengths of the hose segments in the dry and ethanol part of the cooling stage were 2 m and 0.3 m, respectively. The super-cooled gas was then led directly to the specimen area, while the specimen was cooled from its top and bottom side by a pair of nozzles to reach the specimen temperature of −27 °C before the start of the experimental procedure. The discrepancy between this temperature and the nominal temperature of −5 °C of the specimen at the start of the measurement was given by the thermal conductivity of the samples leading to a rapid rise in the temperature before the SHPB experiment was started. The cooling stage was developed by team members Jan Falta and Marcel Adorna. The stage is shown in Fig. 4.57.

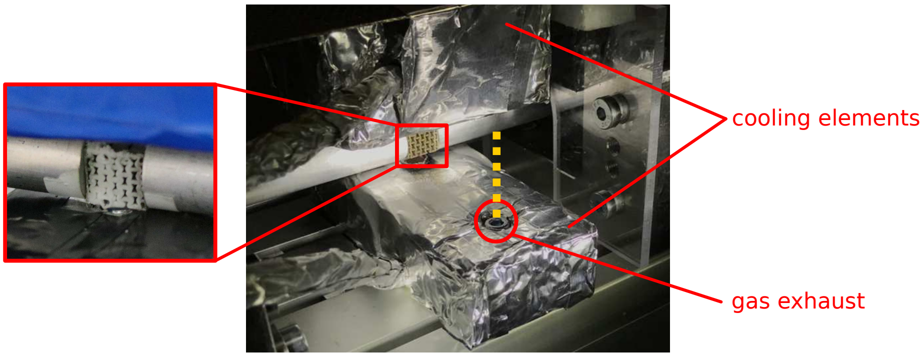

Figure 4.57: The cooling stage mounted in the SHPB setup.

Chapter 5

Experiments and Results

Several experimental campaigns with different types of specimens were performed during this study. An overview of the major experimental campaigns and the main results are presented in this chapter. The results are focused particularly on the experiments with the SLS printed austenitic steel auxetic structures. However, the representative results of the other materials covering the application of DIC, strain-rate sensitivity and dynamic material properties are also shown.

5.1 Overview of the experimental campaigns

Two major groups of specimens were tested in this study: (i) SLS auxetic lattices made of 316L–0407 powdered austenitic steel (see Section 4.1.1), (ii) hybrid open-cell foams and auxetic structures with a polymeric core and a nanocrystalline nickel coating (see Section 4.1.2 and 4.1.3). In the following list, an overview of the individual experimental campaigns presented in this study is summarized:

- **Campaign 1** - SLS auxetics 3 × 3 - 3 types of strain-rate sensitive fillings; 316L–0407; November-December 2016; SHPB; 1 strain-rate; aluminum bars; paper pulse-shaper
- **Campaign 2** - SLS auxetics 6 × 6; 316L–0407; October 2017 - October 2018; SHPB + OHPB; 4 strain-rates; aluminum bars; copper pulse-shaper
- **Campaign 3** - SLS auxetics 6 × 3; 316L–0407; October 2017 - October 2018; OHPB; 3 strain-rates; aluminum bars; no pulse-shaper
- **Campaign 4** - SLS auxetics 3 × 3 - different temperatures; 316L–0407; May 2019; SHPB; 2 strain-rates; aluminum bars; copper pulse-shaper
- **Campaign 5** - Hybrid Ni/Pu foams; May 2017; SHPB; 2 strain-rates; aluminum bars; copper or no pulse-shaper
- **Campaign 6** - Hybrid Ni/polymer auxetics; January 2019; OHPB; 2 strain-rates; PMMA bars; no pulse-shaper

5.2 Campaign 1 - Initial testing - SLS Auxetics

Campaign 1 was the initial experimental investigation of the SLS printed auxetic lattices using SHPB. The applicability of the method and quality of the results were investigated in the experiments. Moreover, some of the specimens were filled with a strain-rate sensitive filling to analyze the effect of the intermediate phase in the structure. The structures were tested using a quasi-static compression and only a single strain-rate in SHPB.

5.2.1 Specimens

The first version of the SLS auxetic lattices was tested. Here, three types of auxetic structures with 3×3 cells were analyzed. The specimens are described in detail in Section 4.1.1 together with information about the materials used as the strain-rate sensitive filling. For purposes of clarity, the specimens used in Campaign 1 and Campaign 2 are compared in Fig. 5.1.

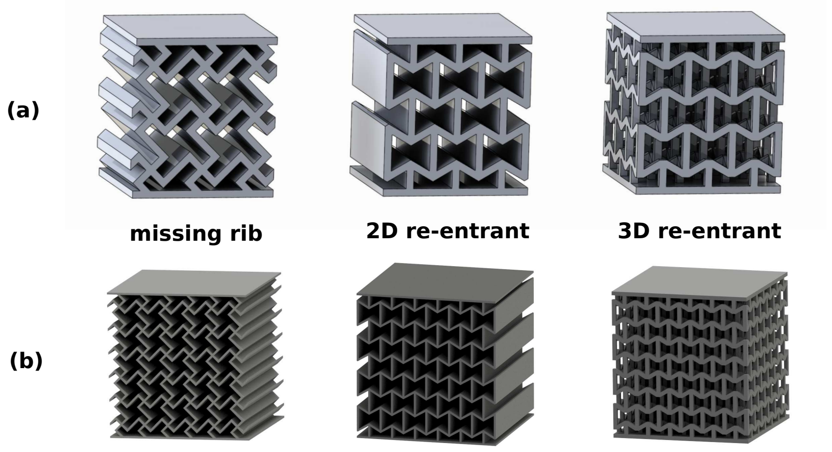

Figure 5.1: The tested SLS Auxetics: (a) initial versions - Campaign 1, (b) optimized versions - Campaign 2.

5.2.2 Experimental setup

A modified Kolsky SHPB setup was used in the study. The incident, transmission, and striker bars had the same nominal diameter of 20 mm with a solid cross-section and were made of a high-strength aluminum alloy (EN-AW-7075-T6) to match the mechanical impedance of the specimens as close as possible. The incident bar and the transmission bar had the same length of 1600 mm and were supported by eight low-friction polymer-liner slide bearings with an aluminum housing (Drylin FJUM housing, IGUS, Germany). The striker bar with a length of 500 mm was used for the generation of the incident wave. The experiments were carried out without a momentum trap as the damping elements were not in initial contact with the transmission bar. A paper pulse-shaper (thickness of 2 × 0.25 mm) satisfactorily reduced the spurious effects of the wave dispersion, while the wave shape was not significantly influenced. This allowed for constant strain-rates in the plateau region with no wave interference in the bars. However, a better version of pulse-shaper has been found in the subsequent campaigns.

The deformation process of the sample was observed using a Fastcam SA-5 high-speed digital camera. As a compromise between the frame rate and the image resolution, 100 kfps and a 320 × 192 px image resolution were chosen.

A gas–gun release pressure of 0.5 MPa was used in the experiments, resulting in impact velocity of the striker bar approx. $33\,\mathrm{ms}^{-1}$. The impact velocity was tuned to achieve the maximal deformation in the specimen and a constant strain-rate during most of the time during the experiment.

5.2.3 Dynamic equilibrium and results consistency

Good quality dynamic equilibrium was observed in all the experiments. As the printing precision is high, the results were very consistent. An example of the evaluated dynamic equilibrium during the experiment with the 2D re-entrant specimen is shown in Fig. 5.2. The consistency of the results is illustrated in the three stress-strain curves shown in Fig. 5.3.

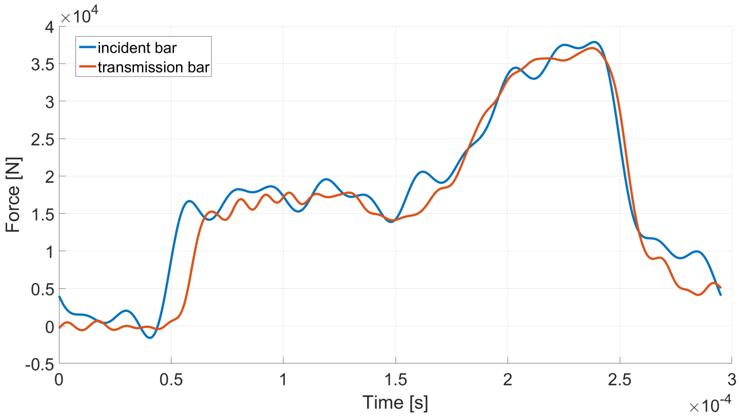

Figure 5.2: An example of the evaluated dynamic equilibrium during the experiment with the 2D re-entrant specimen.

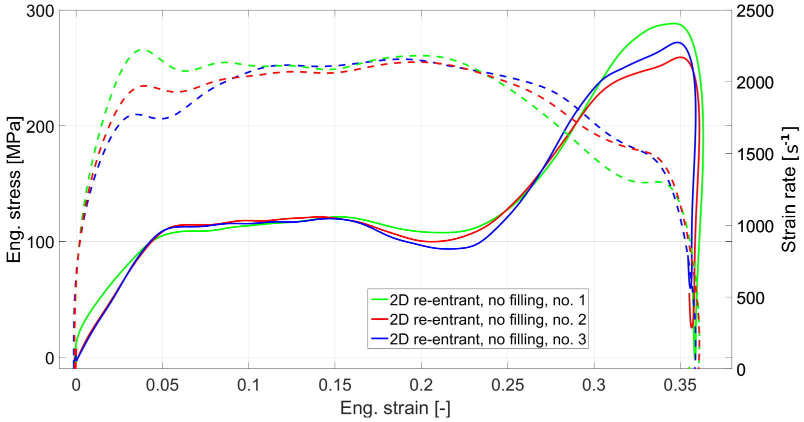

Figure 5.3: The consistency of the results is illustrated in the three stress-strain curves.

5.2.4 Stress-strain diagrams

In this experimental campaign, it was possible to evaluate the stress-strain diagrams for the three types of auxetic structures tested in SHPB. A strong strain-rate sensitivity has been identified in the structures increasing the average plateau stress roughly by a factor of 1.4-1.7 (depending on the type of the structure). The comparison of the average plateau stress in the quasi-static and the dynamic compression together with the specific energy absorption ratio (ratio of strain energy in the dynamic and quasi-static compression) is summarized in Tab. 5.1. The average stress-strain and strain-rate to strain curves are shown in Fig. 5.4-Fig. 5.6. The standard deviation of the data is represented with the shaded area. During the experimental campaign, DIC was successfully used for the analysis of the in-plane displacements and strains of the specimens. However, the data are not presented in this study, as better quality image correlation results were measured in the subsequent campaigns. Only the representative and most interesting results from the DIC are shown in the thesis. For more information about the DIC results from this particular experimental campaign, please refer to the related contribution [1].

Structure	**Average plateau stress**			**Specific energy absorption ratio**
	Static [MPa]	Dynamic [MPa]	Ratio [-]	Dynamic/Static [-]
2D re-entrant	80	113	1.41	1.43
3D re-entrant	33	51	1.56	1.55
Missing-rib	30	49	1.66	1.66

Table 5.1: The average plateau stress and specific energy absorption ratio.

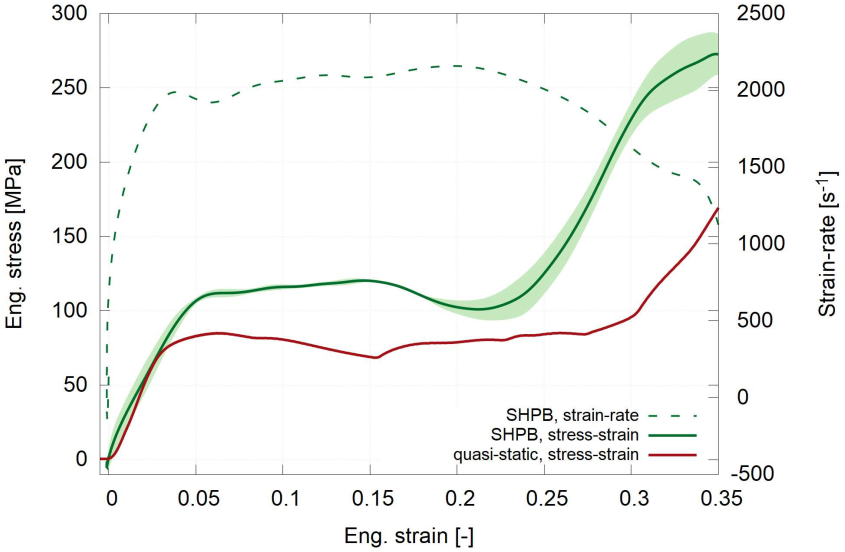

Figure 5.4: The 2D re-entrant honeycomb - the stress-strain diagram from the SHPB experiment compared with the quasi-static data. The standard deviation of the data is represented with the shaded area.

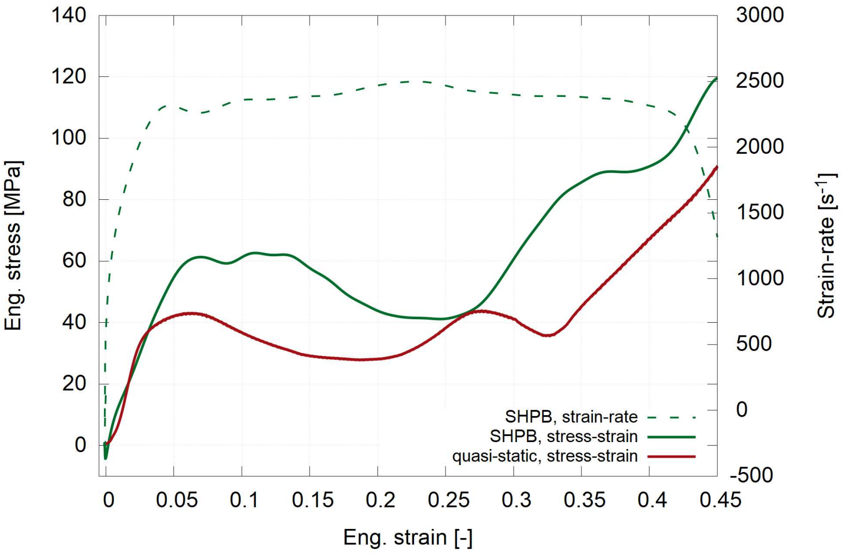

Figure 5.5: The 3D re-entrant honeycomb - the stress-strain diagram from the SHPB experiment compared with the quasi-static data. The standard deviation is not shown here as only a single experiment was valid.

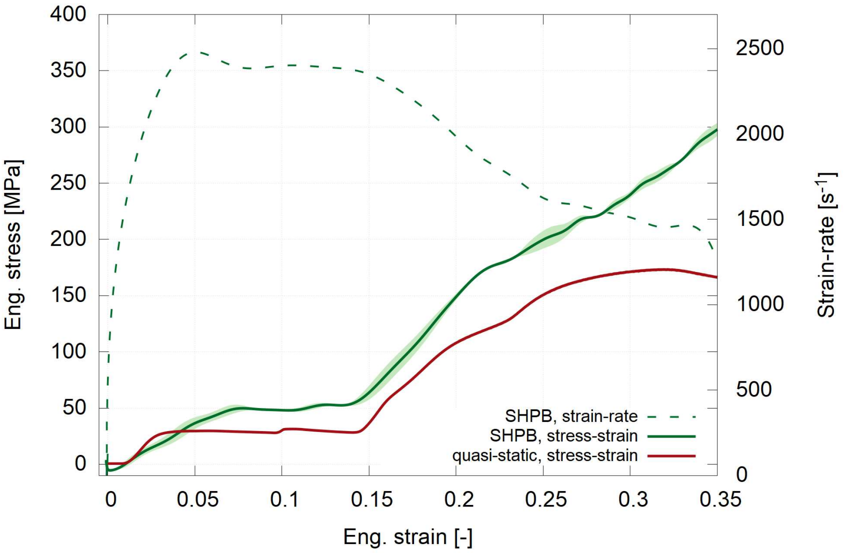

Figure 5.6: The missing-rib - the stress-strain diagram from the SHPB experiment compared with the quasi-static data.

5.2.5 Effect of filling

Two types of strain-rate sensitive fillings (ordnance gelatin and closed cell polyurethane foam) were used to create the interpenetrating phase composite (IPC) combining the auxetic lattice structure with the highly strain-rate sensitive material. The ordnance gelatin was selected as it is used as a ballistic gelatin and its strain-rate sensitivity and material properties are well known. The closed-cell polyurethane foam was selected because of its low density and strain-rate sensitivity related to the closed pores. The effect of the fillings was detectable in the evaluated data for all the investigated structures. The increase in the factor of the averaged plateau stress was approx. 1.05-1.40 (depending on the type of the auxetic structure). The specific energy absorption ratio between the non-filled structures and the structures with the filling is shown in Tab. 5.2. The representative averaged stress-strain curves showing the effect of the filling for the individual structures are shown in Fig. 5.7 - Fig. 5.9. For detailed information, please refer to our paper [1]. The investigation of the strain-rate sensitive filling effects is a part of the research conducted by team member Tomáš Doktor.

Structure	**Filling**	**Specific energy absorption ratio**
2D re-entrant	gelatin	1.11
	PU	1.06
3D re-entrant	gelatin	1.09
	PU	1.39
Missing-rib	gelatin	1.06
	PU	1.18

Table 5.2: The specific energy absorption ratio between the non-filled structures and the structures with the filling in the dynamic compression.

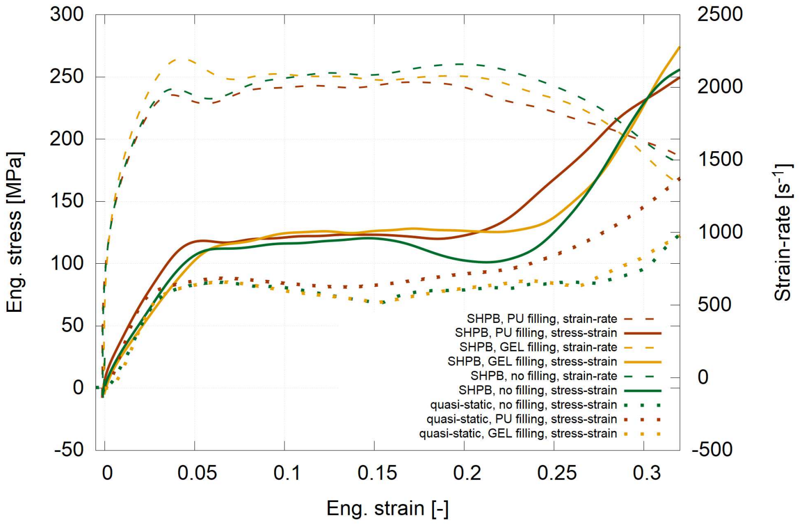

Figure 5.7: The 2D re-entrant honeycomb - the stress-strain diagram from the SHPB experiment compared with the quasi-static data - the effect of the strain-rate sensitive filling.

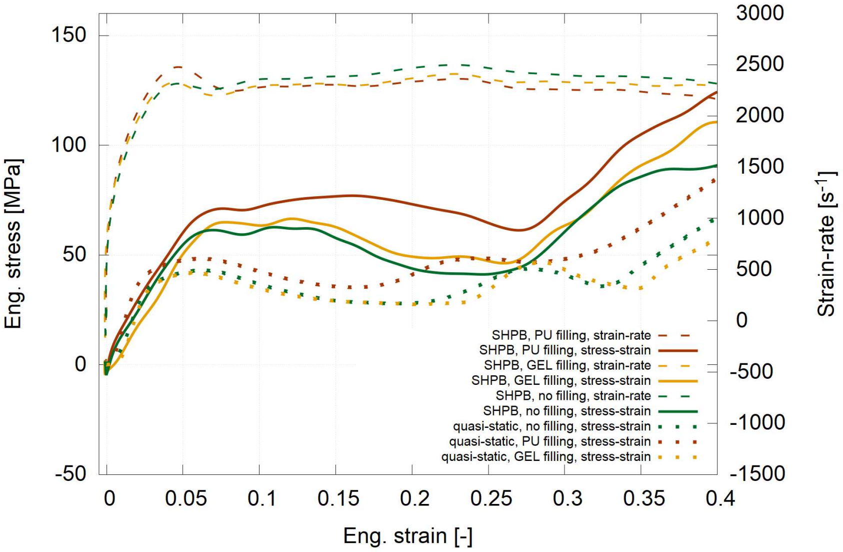

Figure 5.8: The 3D re-entrant honeycomb - the stress-strain diagram from the SHPB experiment compared with the quasi-static data - the effect of the strain-rate sensitive filling.

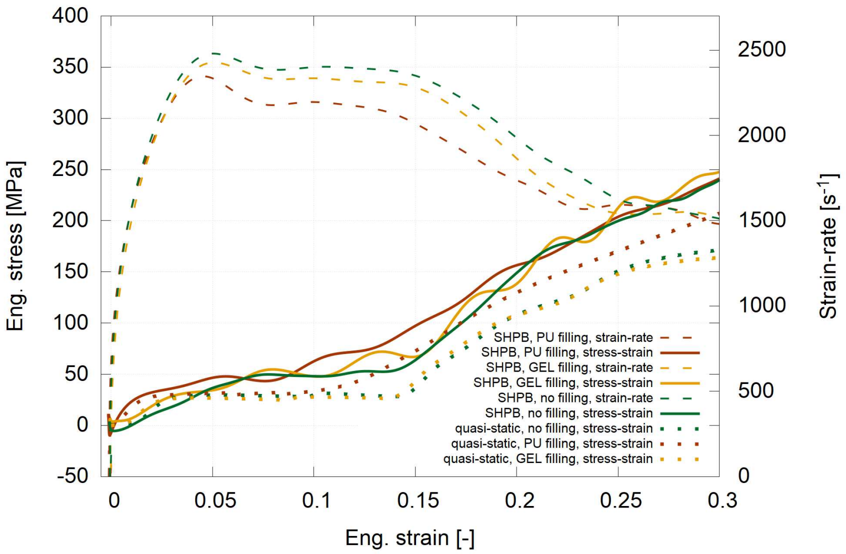

Figure 5.9: The missing-rib - the stress-strain diagram from the SHPB experiment compared with the quasi-static data - the effect of the strain-rate sensitive filling.

5.2.6 Campaign 1 - Summary

- Pilot testing of the auxetic structures subjected to the dynamic impact in the SHPB.
- A set of three different auxetic structures produced using SLS was tested.
- Behavior of the specimens showed it was strain-rate sensitive with significant strain-rate hardening effect between the quasi-static and dynamic conditions.
- Behavior of the specimens was auxetic in all cases (investigated using DIC - not shown in the study).
- Effect of the strain-rate sensitive filling was detectable.
- As the response of the structures under the quasi-static and dynamic conditions was different, it was necessary to perform an advanced study for the investigation of the collapse and the effects of the strain-rate, micro-inertia and friction.

5.3 Campaign 2 - Strain-rate sensitivity - SLS Auxetics

In this experimental campaign, mechanical behavior of the SLS printed auxetic lattices at both the quasi-static and dynamic loading conditions was studied. In this program, a set of three different optimized auxetic lattices with at least 6 × 6 unit cells was tested. The specimens were optimized using the results and experiences from Campaign 1. Therefore, the printing process was upgraded to achieve better resolution, smaller thickness of the struts and smaller size of the cells. Moreover, the geometry of the specimens was upgraded to achieve better behavior of the structures during the collapse.

In this experimental campaign, the strain-rate sensitivity, micro-inertia and friction effects under the quasi-static and dynamic conditions were investigated. Thus, the specimens were tested in uni-axial quasi-static and dynamic compression using both the SHPB and OHPB at four different strain-rates. At least five specimens were tested at each strain-rate to guarantee sufficient statistics and to obtain reliable results. Based on the quasi-static and calibration tests, the parameters of the dynamic tests were optimized to achieve approximately the identical strain-rate and strain for all the types of the specimens (in contrast with Campaign 1).

DIC was used in this study to compare the image-based results with the results from the strain-gauges. Primarily, the DIC was employed for the evaluation of the functions of Poisson's ratio (see Section 4.8). The data have been used for the development of the finite-element numerical analyses simulating the auxetic lattices under the quasi-static and dynamic conditions. The quasi-static investigation and numerical simulations of the auxetic lattices is a part of the research conducted by team member Petr Koudelka.

5.3.1 Experimental setup

In this experimental campaign, both the SHPB and OHPB setups were employed for the testing at a spectrum of four different strain-rates. OHPB was used for the testing at two lower strain-rates (approx. $500\,\mathrm{s}^{-1}$ and approx. $1000\,\mathrm{s}^{-1}$) whereas SHPB was used for the testing at two higher strain-rates (approx. $1500\,\mathrm{s}^{-1}$ and approx. $3000\,\mathrm{s}^{-1}$).

OHPB

The OHPB setup described in detail in Section 4.9 was used. All the bars had a nominal diameter of 20 mm, had an identical length of 1600 mm and were made of a high-strength aluminum alloy (EN-AW-7075-T6). Both bars were instrumented using foil strain-gauges mounted at a distance of 200 mm from the impact face and were connected in a Wheatstone half-bridge arrangement. The experiments were observed by a Fastcam SA-5 high-speed camera using a reduced resolution of 184×128 pixels with a corresponding frame rate of approximately 186 kfps. To reach two different strain-rates in the specimens, two impact velocities of the striker bar were used. A lower striker impact velocity of approx. $7\,\mathrm{ms}^{-1}$ was used to compress the specimens at a strain-rate of approximately $500\,\mathrm{s}^{-1}$ (referred to as strain-rate 1 in the following text). A higher striker impact velocity of approximately $18\,\mathrm{ms}^{-1}$ was used to compress the specimens at a strain-rate of approximately $1000\,\mathrm{s}^{-1}$ (referred to as strain-rate 2 in the following text). Approximately 75 images of the deforming specimen were captured using the high-speed camera during each experiment.

SHPB

The standard arrangement of the experimental setup with the striker, incident, and transmission bars was used for the testing. All the bars had a nominal diameter of 20 mm and were made of a high-strength aluminum alloy (EN-

AW-7075-T6). A striker bar with a length of 500 mm was accelerated using a gas-gun system. The incident bar and the transmission bar had an identical length of 1600 mm. The incident bar was instrumented by establishing three individual measurement points, each equipped by foil strain-gauges. On the incident bar, one measurement point was located in the middle of the bar and the other two measurement points were located 200 mm from each of the faces of the bar, while the transmission bar was equipped with one measurement point located 200 mm from the impact face of the bar. At each measurement point, a pair of strain-gauges wired in a Wheatstone half-bridge arrangement was used. The experiments were observed by a Fastcam SA-5 high-speed camera. In the experiments, the region of interest was set to 256 × 168 pixels. The reduced resolution of the camera allowed for the observation of the specimen during the impact with approximately 130 kfps. To reach two different strain-rates in the specimens, two impact velocities of the striker bar were used. A lower striker impact velocity of approx. $21\,\mathrm{ms}^{-1}$ was used to compress the specimens at a strain-rate of approximately $1500\,\mathrm{s}^{-1}$ (referred to as strain-rate 3 in the following text). A higher striker impact velocity of approximately $43\,\mathrm{ms}^{-1}$ was used to compress the specimens at a strain-rate of approximately $3000\,\mathrm{s}^{-1}$ (referred to as strain-rate 4 in the following text). Depending on the type of the auxetic structure, the specimens in the low-rate experiments were compressed to a maximum overall strain of approximately $25-30\,\%$. The specimens in the experiments conducted at the higher strain-rate reached a significantly higher overall strain of approximately $40-50\,\%$. To minimize the wave dispersion effects, cylindrical soft copper pulse-shapers were placed on the incident bar impact face. Depending on the type of the auxetic structure and strain-rate, the diameter and the thickness of the pulse-shapers varied between $7-8\,\mathrm{mm}$ and $0.5-1.0\,\mathrm{mm}$, respectively. Approximately 35 images of the deforming specimen during the first deformation pulse were captured using the high-speed camera and were processed using the DIC technique.

5.3.2 Experiment validity

Based on the experience with the testing of the auxetic structures in Campaign 1 as well as other materials in other experimental programs (not presented in this thesis), it was possible to optimize the parameters of the setup and pulse-shaping technique to achieve a good dynamic equilibrium and high quality strain-gauges signals. The typical output of the experiment is shown in Fig. 5.10. The typical strain wave equilibrium, force equilibrium and corresponding stress-strain diagram are shown in Fig. 5.11 - Fig. 5.13.

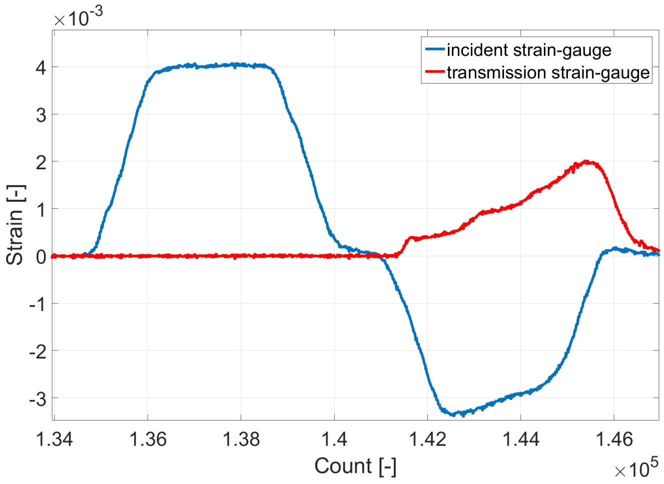

Figure 5.10: The typical output of the experiment - strain-gauges signals.

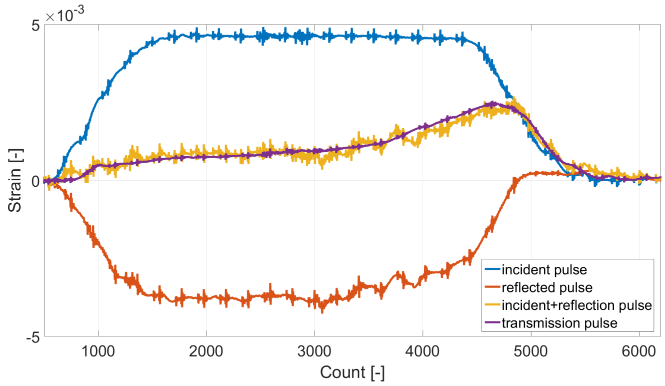

Figure 5.11: The typical strain wave dynamic equilibrium.

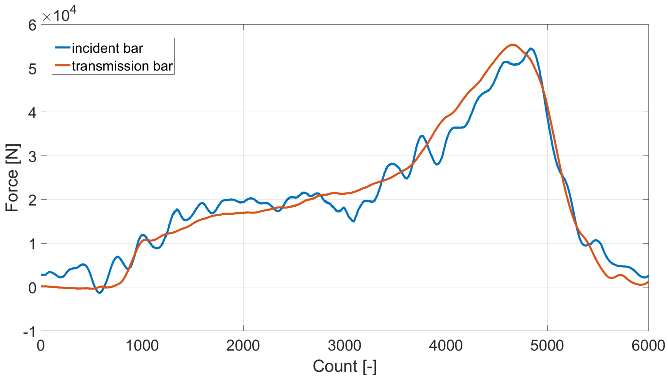

Figure 5.12: The typical force equilibrium.

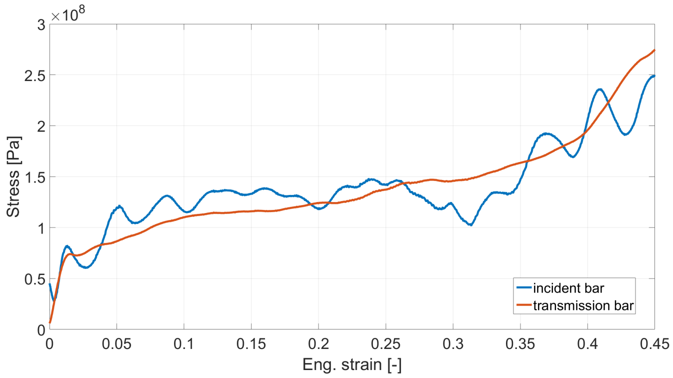

Figure 5.13: The evaluated stress-strain diagram using the stress calculated from both the incident and the transmission strain-gauge.

5.3.3 Strain-rate sensitivity

The average stress-strain and strain-rate curves were evaluated for all the experiments and are presented in the following text. The curves were calculated as the average of all the experiments at a given strain-rate in the relevant range of the strain. For all the structures, similar trends of the strain-rate sensitivity were observed. Tabular data summarizing the strain-energy density for the common range of the plateau strain (to approx. 15 %) and the corresponding relative ratios revealing similar trends are presented.

2D re-entrant

The slideshow of the high-speed camera images showing the deformation of the 2D re-entrant in the SHPB is shown in Fig. 5.14. The average stress-strain and strain-rate to strain diagrams for the 2D re-entrant are shown in Fig. 5.15. The 2D re-entrant exhibited the most profound strain-rate sensitivity related to the collapse of the first layer of the cells. With an increasing strain-rate, the collapse occurred at higher strains and higher stresses. This strain-rate hardening is connected with the different impact velocity and micro-inertia effects during the collapse of the first layer. After the collapse of the first layer, the rest of layers' collapsed almost instantly producing stress oscillations in the plateau region. The calculated strain energy density for the strain ranging from 0 to 0.15 for all the strain-rates and the ratios related to the quasi-static value are shown in Tab. 5.3. The strain energy density plotted against the strain-rate is shown in Fig. 5.16.

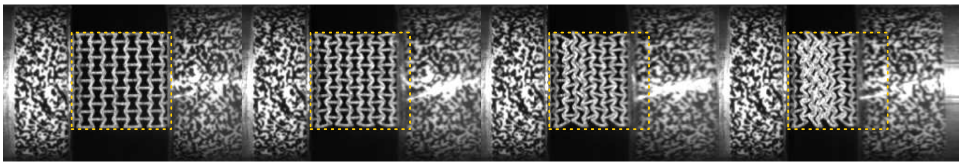

Figure 5.14: The 2D re-entrant - the slideshow of the high-speed camera images showing the deformation.

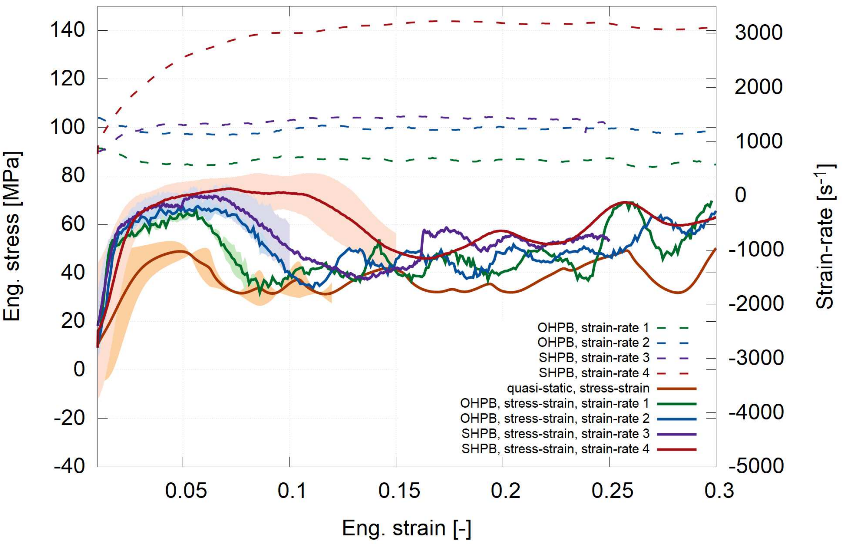

Figure 5.15: The 2D re-entrant - the average stress-strain and strain-rate to strain diagrams. For purposes of clarity, the errors are displayed only to a limited strain.

Nominal strain-rate	**Strain energy density**	**Ratio**
	(strain $0 - 0.15$)	
[s^{-1}]	[MJm^{-3}]	[−]
Quasi-static	5.18	1.00
≈ 500	6.70	1.30
≈ 1000	7.32	1.42
≈ 1500	7.80	1.51
≈ 3000	9.08	1.75

Table 5.3: The 2D re-entrant - the calculated strain energy density for the strain ranging from 0 to 0.15 for all the strain-rates and ratios related to the quasi-static value.

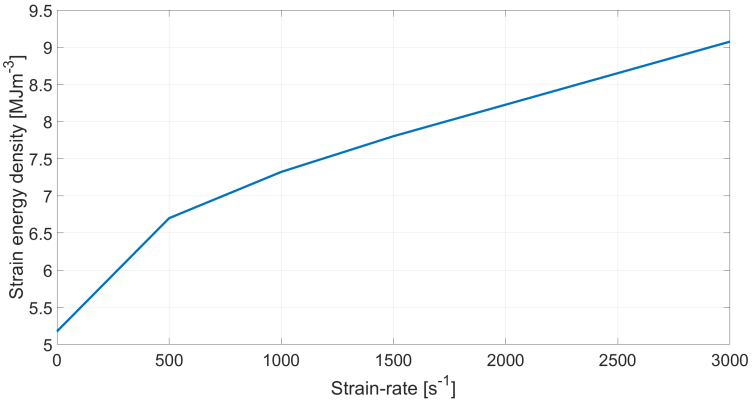

Figure 5.16: The 2D re-entrant - the strain energy density plotted against the strain-rate.

3D re-entrant

The 3D re-entrant has the lowest porosity and the highest nominal density from all the tested structures and exhibited very stiff behavior. The slideshow of the high-speed camera images showing the deformation of the 3D re-entrant in the SHPB is shown in Fig. 5.17. The average stress-strain and strain-rate to strain diagrams for the 3D re-entrant are shown in Fig. 5.18. As the specimen was compact with only small gaps between the layers, no sudden collapse of the individual layers occurred at any strain-rate and the measured stress-strain curves were smooth. The strain-rate sensitivity of the lattice was clearly detectable. Unfortunately, the maximum strain at strain-rate 3 performed using the SHPB (see violet curve in Fig. 5.18) was limited to only approx. $0.15 - 0.20$ because of the stiffness of the cell (note that the OHPB method has been introduced in the study to overcome this SHPB disadvantage). The calculated strain energy density for the strain ranging from 0 to 0.15 for all the strain-rates and ratios related to the quasi-static value are shown in Tab. 5.4. The strain energy density plotted against the strain-rate is shown in Fig. 5.19.

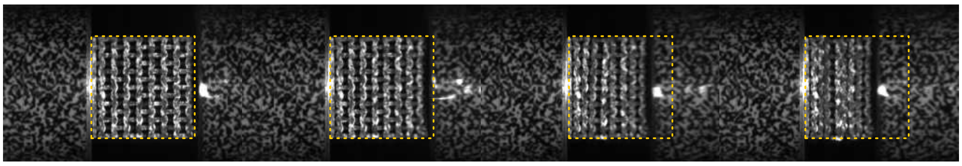

Figure 5.17: The 3D re-entrant - the slideshow of the high-speed camera images showing the deformation.

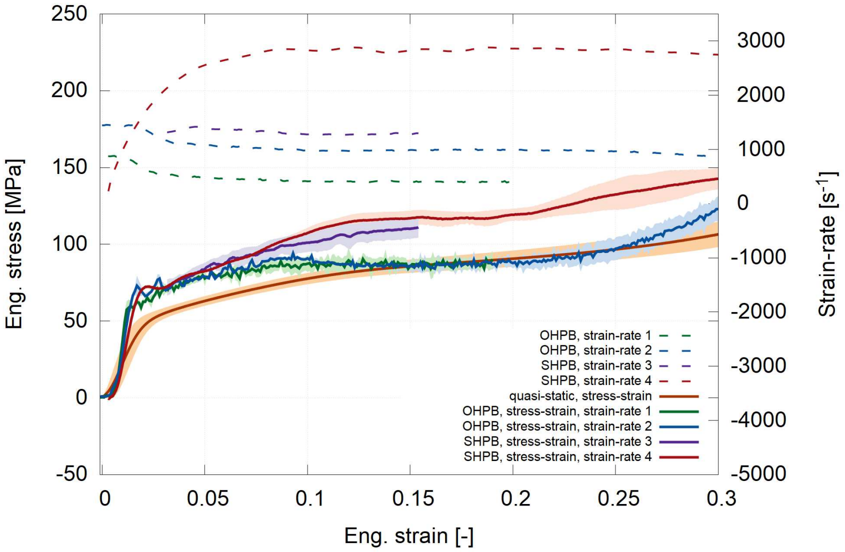

Figure 5.18: The 3D re-entrant - the average stress-strain and strain-rate to strain diagrams.

Nominal strain-rate	**Strain energy density**	**Ratio**
	(strain $0 - 0.15$)	
[s^{-1}]	[MJm^{-3}]	[$-$]
Quasi-static	9.81	1.00
≈ 500	11.24	1.15
≈ 1000	11.57	1.18
≈ 1500	12.84	1.31
≈ 3000	13.31	1.36

Table 5.4: The 3D re-entrant - the calculated strain energy density for the strain ranging from 0 to 0.15 for all the strain-rates and ratios related to the quasi-static value.

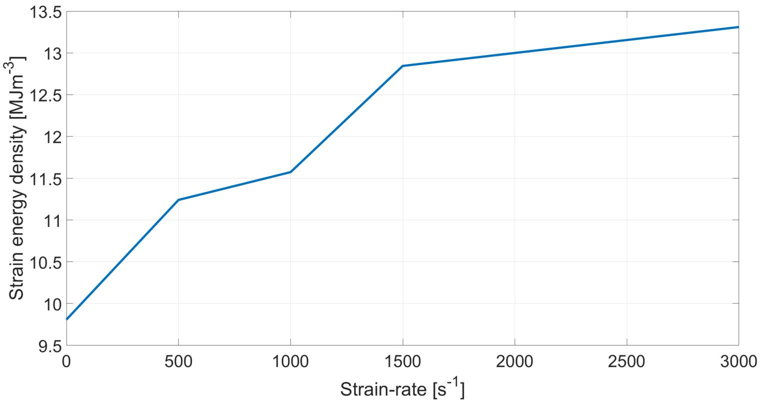

Figure 5.19: The 3D re-entrant - the strain energy density plotted against the strain-rate.

Missing-rib

The missing-rib was the weakest structure exhibiting large lateral deformations and side movements. The collapse of the individual layers was relatively uniform and distributed through the specimen and the measured stress-strain curves were smooth. The strain-rate sensitivity of the lattice was detectable and exhibited similar trends as in the case of the 3D re-entrant. The slideshow of the high-speed camera images showing the deformation of the missing-rib in the SHPB is shown in Fig. 5.20. The average stress-strain and strain-rate to strain diagrams for the missing-rib are shown in Fig. 5.21. The calculated strain energy density for the strain ranging from 0 to 0.15 for all the strain-rates and ratios related to the quasi-static value are shown in Tab. 5.5. The strain energy density plotted against strain-rate is shown in Fig. 5.22.

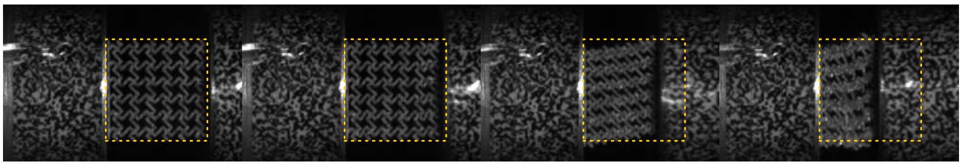

Figure 5.20: The missing rib - the slideshow of the high-speed camera images showing the deformation.

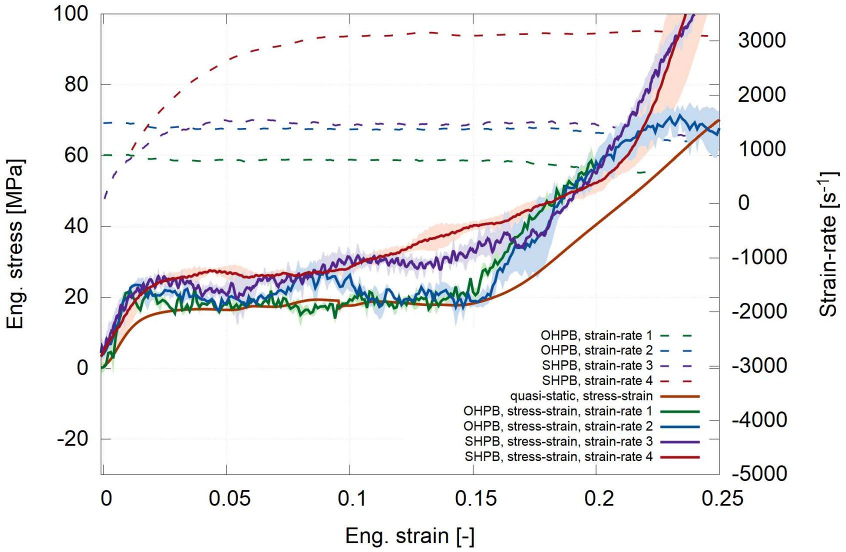

Figure 5.21: The missing-rib - the average stress-strain and strain-rate to strain diagrams.

Nominal strain-rate [s^{-1}]	**Strain energy density** (strain $0-0.15$) [MJm^{-3}]	**Ratio** [$-$]
Quasi-static	2.49	1.00
≈ 500	2.51	1.01
≈ 1000	2.90	1.17
≈ 1500	3.55	1.43
≈ 3000	3.96	1.59

Table 5.5: The missing-rib - the calculated strain energy density for the strain ranging from 0 to 0.15 for all the strain-rates and ratios related to the quasi-static value.

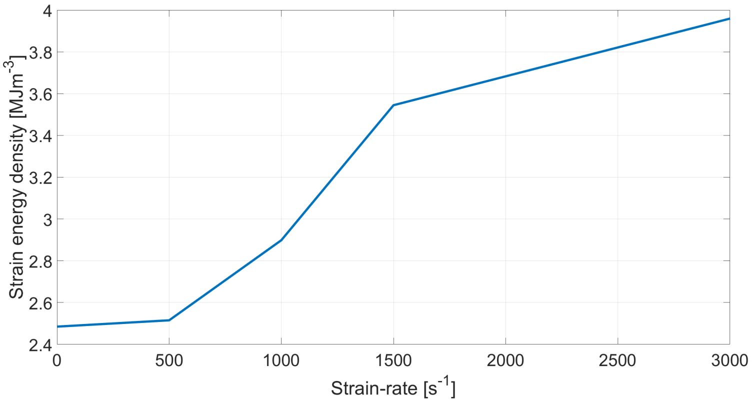

Figure 5.22: The missing-rib - the strain energy density plotted against the strain-rate.

All structures - specific strain energy density ratio

One of the possibilities how to compare the tested auxetic structures is to use the specific strain energy density plots. The specific strain energy density ratio was calculated as the ratio of the strain energy density at a given strain-rate with the quasi-static strain energy density (both integrated in a strain range from 0 to 0.15). The specific strain energy density ratio of all the structures plotted against the nominal strain-rate is shown in Fig. 5.23. All the structures exhibited a similar trend in the strain-rate sensitivity as the specific strain energy density ratio monotonically increased.

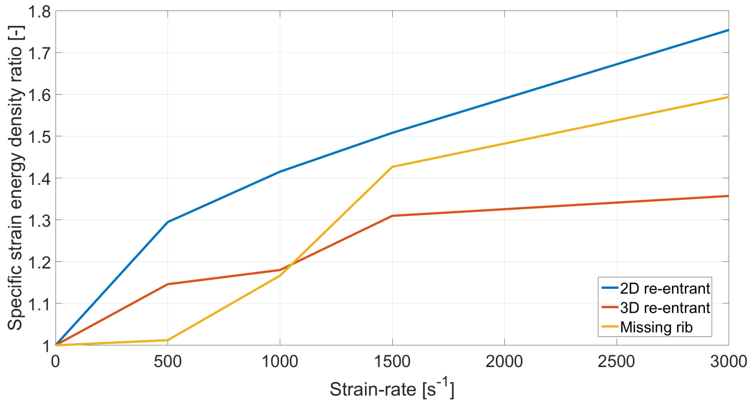

Figure 5.23: All the structures - the specific strain energy density ratio plotted against the strain-rate.

5.4 Campaign 2 - Function of Poisson's ratio - SLS Auxetics

One of the most important properties of the auxetic structures is Poisson's ratio. Generally, it is not a constant value, but rather a function dependent on strain and even on strain-rate. Evaluating the function of Poisson's ratio was the second part of Campaign 2. The DIC was employed for evaluating Poisson's ratio to investigate the possible changes in the deformation behavior. In this section, the methods for the evaluation of Poisson's ratio are summarized and results of both the quasi-static and SHPB experiments (strain-rate 3 and strain-rate 4, see Section 5.3.1) are presented. The experimental setup and experimental program was identical to that described in Section 5.3.1. For more information, please refer to the related contribution [4].

5.4.1 Function of Poisson's ratio

The in-plane displacement and strain fields were evaluated using the DIC algorithm described in detail in Section 4.8. From the strain fields assessed by DIC, Poisson's ratio ν_{12} was calculated using the formula

$$\nu_{12} = -\frac{\epsilon_2}{\epsilon_1}, \tag{5.1}$$

where ϵ_2 is the lateral strain in the direction perpendicular to the direction of the loading and ϵ_1 is the strain in the direction of loading.

Different methods for determining the function of Poisson's ratio were used for both the quasi-static and dynamic experiments. The outputs of the different methods were analyzed and compared to evaluate their reliability. As three specimens of each microarchitecture were tested in the quasi-static experiments and five specimens were tested at each strain-rate during the

SHPB experiments, the mean curves and standard deviation envelopes of the functions of Poisson's ratio for each type of experiment were calculated.

The methods for calculating Poisson's ratio were based on the different sets of correlation markers selected for the calculation. In the first method, both the deformation parallel and perpendicular to the direction of the loading were evaluated from the inner part of the specimens' microstructure, where the concentration of the lateral strain occurred (see the red markers of the correlation points in Fig. 5.24). In the following text, the function of Poisson's ratio calculated from this region of interest will be designated as the "inner-inner" function. In the second method, the deformation in the same directions was calculated from the outer part of the specimens' microstructure (see the outer green markers of the correlation points in Fig. 5.24). The corresponding function of Poisson's ratio will be designated as the "outer-outer" function. The difference in the functions of Poisson's ratio using both methods enables one to characterize the influence of the boundary effects emerging from the cellular nature of the specimens. In the dynamic experiments, another method based on the local Poisson's ratio was also employed to study its variations in the different parts of the crushed microstructures. Here, Poisson's ratio was derived as a mean of the ratio between the lateral and longitudinal strains in the localized regions around every correlation point within the outer-outer region. Since Poisson's ratio calculated at every time step for a given correlation point is based on the local gradient of the lateral and longitudinal deformation, the corresponding function of Poisson's ratio will be designated as the "local-gradient" function. The inner-inner and outer-outer methods were based on a correlation grid composed of markers generated over the joints of the individual struts forming the auxetic microstructure. Due to the lower resolution of the high-speed images and rapid changes in the microstructure, the local-gradient method was based on a grid with higher density composed of 11×11 points covering the whole observed face of the specimens. Apart from the possibility to plot the maps of the strains and Poisson's ratio over the entire investigated structure, the average over the region corresponding to the inner-inner method of the evaluation was calculated to obtain the comparative Poisson's ratio–strain curves.

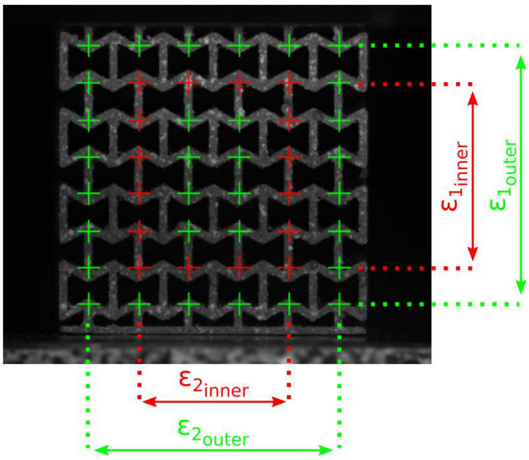

Figure 5.24: The correlation pattern (green color) generated on the 2D re-entrant honeycomb specimen showing the inner (red color) and outer part used for the DIC evaluation of results.

In the following paragraphs, the attention is focused on the functions of Poisson's ratio calculated using the inner-inner evaluation method described above. The motivation for this is that the results calculated according to the inner-inner approach can be considered the most representative by taking the region of the cellular microstructure into account, where the boundary effects arising from the free outer faces of the specimens are minimized. A comparison of the results based on all the evaluation methods is also provided.

5.4.2 Function of Poisson's ratio from the DIC - quasi-static loading

As can be seen in Fig. 5.25, the 2D re-entrant honeycomb structure exhibited auxetic behavior during the quasi-static tests over the whole range of the applied compressive strain and the calculated Poisson's ratio remained negative up to a 28 % strain. The maximum absolute value of Poisson's ratio identified for this type of microarchitecture was approx. -0.9 at a 1 % strain. From this strain, Poisson's ratio gradually increased to zero at the maximum compressive strain achieved in the experiments.

On the contrary, the calculated function of Poisson's ratio of the 3D re-entrant honeycomb specimens showed a significantly different quasi-static response of a similar type of unit-cell geometry (see Fig. 5.26). Here, the extreme value of Poisson's ratio only reached the value of -0.1 at the same 1 % of compressive strain. Poisson's ratio then gradually increased, reached a value of -0.05 at a 5 % strain and formed a plateau-like region of an approximately constant Poisson's ratio up to a compressive strain over 30 %.

Fig. 5.27 depicts the function for Poisson's ratio of the missing rib structure. It can be seen that, in this case, the identified compressive response is, in terms of the function of Poisson's ratio, very similar to the 3D re-entrant honeycomb. However, the difference between these two microarchitectures consists in the value of Poisson's ratio at the plateau-like region, where the missing rib structure reaches $\nu_{12} = 0$ at a 10 % strain. Furthermore, from the 25 % of compressive strain, Poisson's ratio increases to positive values. This effect was investigated by the visual inspection of the images captured during the late stages of the experiment and such behavior can be accounted for by the overall loss of stability of the specimens due to excessive rotations of the individual strut joints.

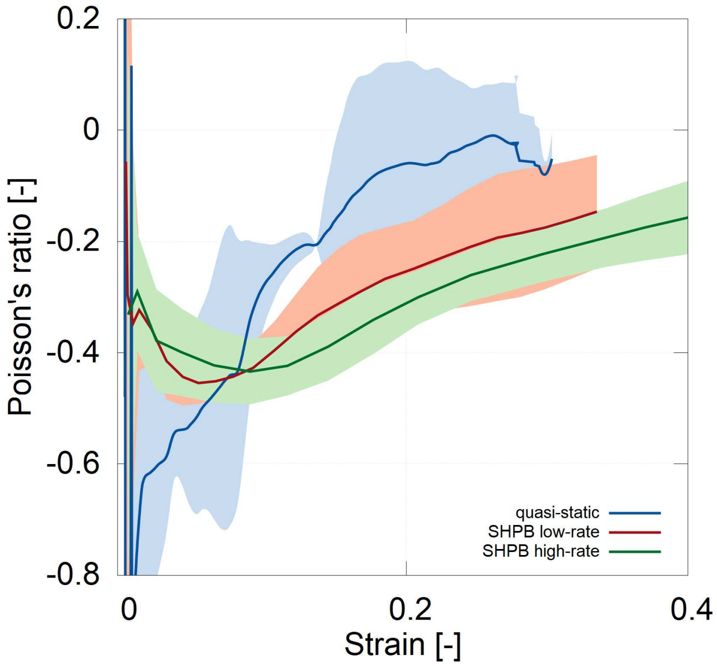

Figure 5.25: The 2D re-entrant honeycomb - the DIC evaluated Poisson's ratio curves, the inner-inner method.

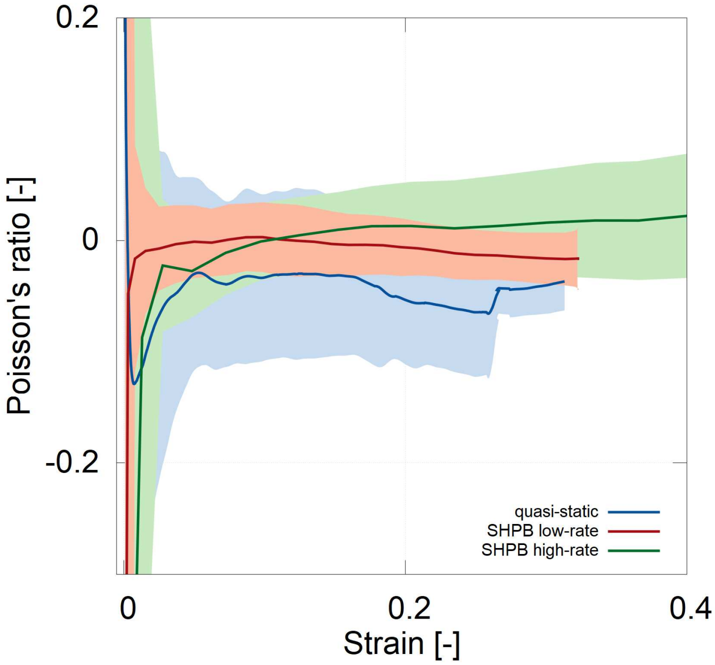

Figure 5.26: The 3D re-entrant honeycomb - the DIC evaluated Poisson's ratio curves, the inner-inner method.

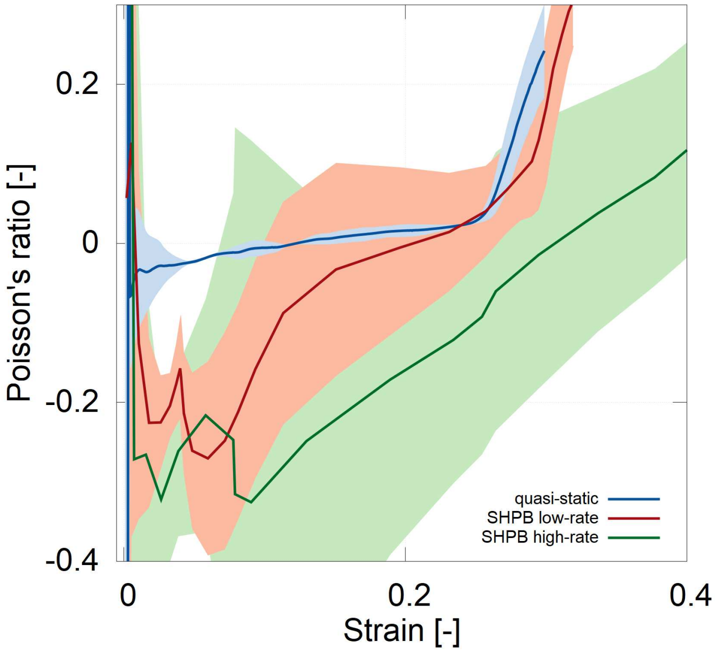

Figure 5.27: The missing-rib - the DIC evaluated Poisson's ratio curves, the inner-inner method.

5.4.3 Function of Poisson's ratio from the DIC – dynamic loading

For every investigated microarchitecture, the DIC based evaluation of the function of Poisson's ratio was performed for both SHPB strain-rates and the resulting curves were compared to reveal the strain dependent characteristics of the structures.

From the comparison of the strain dependent function of Poisson's ratio of the 2D re-entrant honeycomb structure depicted in Fig. 5.25, it can be seen that the overall shape of the curve is very similar for both of the considered strain-rates. Poisson's ratio reaches its global minimum in the initial stages of deformation and then gradually increases up to a positive value. The difference between the strain-rates is the magnitude of the auxetic effect.

Similarly to the quasi-static results, the 3D re-entrant honeycomb structures exhibited a significantly different response than the periodical assembly of the two-dimensional re-entrant honeycombs. As can be seen in Fig. 5.26, the results from the dynamic testing at both of the strain-rates are very similar to each other and the results of the quasi-static test. During the dynamic experiments, Poisson's ratio increased from the value of approximately -0.1 at the very small strains and then formed the plateau-like region similar to the specimens subjected to the quasi-static loading. The comparison of the different strain-rates shows that the values of Poisson's ratio at the plateau region increase with a higher strain-rate. At the lower strain-rate (strain-rate 3), the Poisson's ratio remains constantly negative (approx. -0.02) beyond a 30 % compressive strain. However, with the increase of the applied strain-rate (strain-rate 4), the plateau region reaches positive values at a 10 % compressive strain and further increases at a 40 % strain.

The most profound difference between the quasi-static and the dynamic response (i.e., the strain-rate dependence) was revealed in the case of the missing-rib structure (see Fig 5.27). At both of the considered strain-rates, Poisson's ratio decreased to one local and a global minimum located between a 2 % and 10 % compressive strain. The global minimum was, in both cases, followed by a gradual increase to a positive value while zero Poisson's ratio was reached at a 20 % compressive strain in the case of the low strain-rate and 30 % in the case of the high strain-rate. Both strain-rates produced insignificantly different values for the lowest achieved Poisson's ratio of -0.28 during the lower strain-rate and -0.33 during the high strain-rate experiments. Interestingly, this trend is inverse to the other dynamic experiments. The visual inspection of the deforming structures also showed that the two observable local extrema of the function of Poisson's ratio can be accounted for to the initial collapse of the layers of the microstructure.

5.4.4 Local-gradient results of Poisson's ratio in dynamic compression

The local-gradient method was used for the strain evaluation of the dynamic experiments in parallel to the calculations based on the displacements and strains calculated for each pair of correlation points in the respective direction. Due to significantly lower resolution and number of images in the captured sequence during the dynamic tests, the higher-density correlation grid used in the local-gradient evaluation methods enabled to support the conclusions based on the results from the other methods. A set of images showing the deforming auxetic structure during the impact with the local-gradient results in the form of a map of the strain and Poisson's ratio is shown in Fig. 5.28.

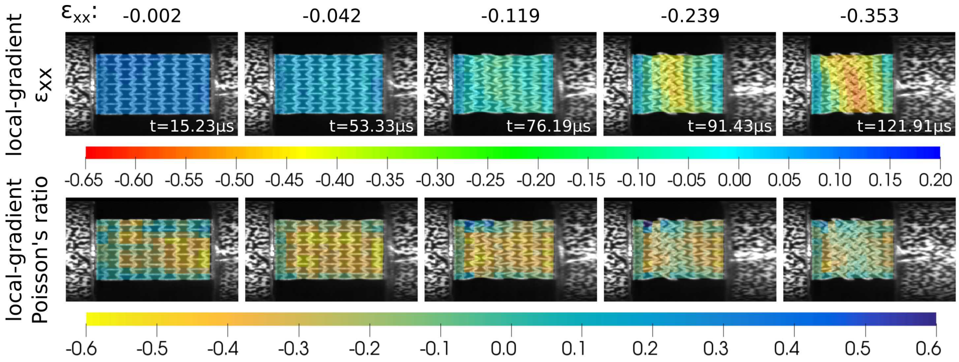

Figure 5.28: The image sequence showing the deforming 2D re-entrant honeycomb auxetic lattice during the impact with the mapped local-gradient results of the longitudinal strain and Poisson's ratio.

The results of the local-gradient analysis of the 2D re-entrant honeycomb lattice are shown in Fig. 5.29. The functions of Poisson's ratio for both of the strain-rates are represented by solid lines showing the mean values with the standard deviations obtained from the region equivalent to the inner-inner method. For comparison, the dashed lines in this figure represent similar curves of the mean Poisson's ratio calculated according to the inner-inner method from the quasi-static and dynamic experiments. It can be seen, that the strain-rate dependence of Poisson's ratio was captured by both methods. The results from the inner-inner method are within the standard deviation envelopes from an approximately 10 % strain up to the densification. Nevertheless, the results from both methods are in very good agreement. The local-gradient functions of Poisson's ratio exhibit slightly lower values than the inner-inner results.

The results of the local-gradient analysis of the 3D re-entrant honeycomb lattice are shown in Fig. 5.30. It can be seen that apart from the high strain-rate measurements, the results from both evaluation methods are also in good agreement. Only Poisson's ratio evaluated using the inner-inner method reaches positive values at an approximately 10 % strain, while the local-gradient method indicates auxetic behavior up to the densification region. From the comparison with the quasi-static results, it can be seen that the deformation behavior of this microstructure is similar to the behavior of the metal foams and the difference in Poisson's ratio decreases with the higher strain-rates.

The results of the full-field analysis of the 2D missing-rib structure are shown in Fig. 5.31. The difference of the inner-inner and local-gradient results is higher than in the case of the 2D re-entrant honeycomb, particularly between a 10 % and 30 % compressive strain. The local-gradient method also gives lower values of Poisson's ratio. However, the results of both methods are very close to the standard deviation envelopes of the local-gradient approach and can be considered very similar. The plot also shows the diametrically different behavior of this structure in comparison with the 3D re-entrant honeycomb. Here, the magnitude of the negative Poisson's ratio of the missing-rib structure increases with the higher strain-rates showing that the dynamic effects induce a significant auxetic response resulting in approximately five times lower Poisson's ratio up to a 10 % compressive strain.

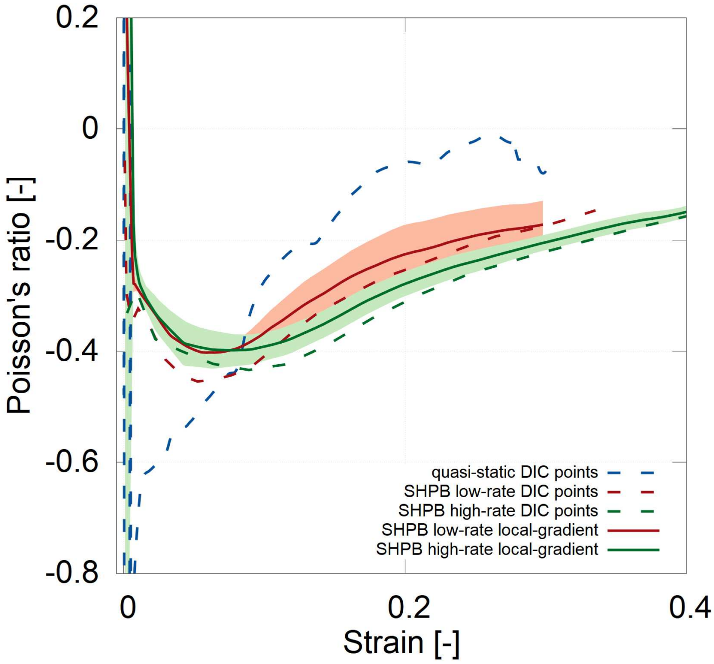

Figure 5.29: The 2D re-entrant honeycomb - the DIC evaluated Poisson's ratio functions, the solid lines – the local-gradient method, the dashed lines - the inner-inner method.

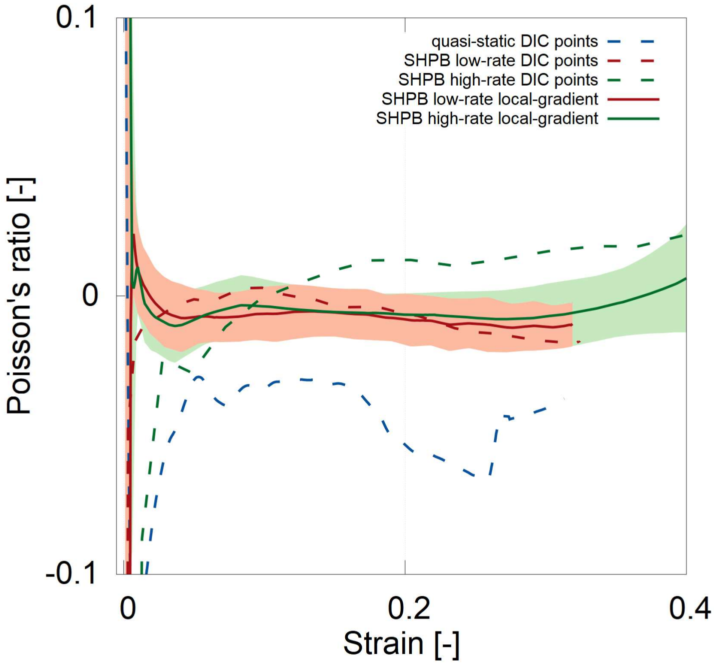

Figure 5.30: The 3D re-entrant honeycomb - the DIC evaluated functions of Poisson's ratio, the solid lines – the local-gradient method, the dashed lines - the inner-inner method.

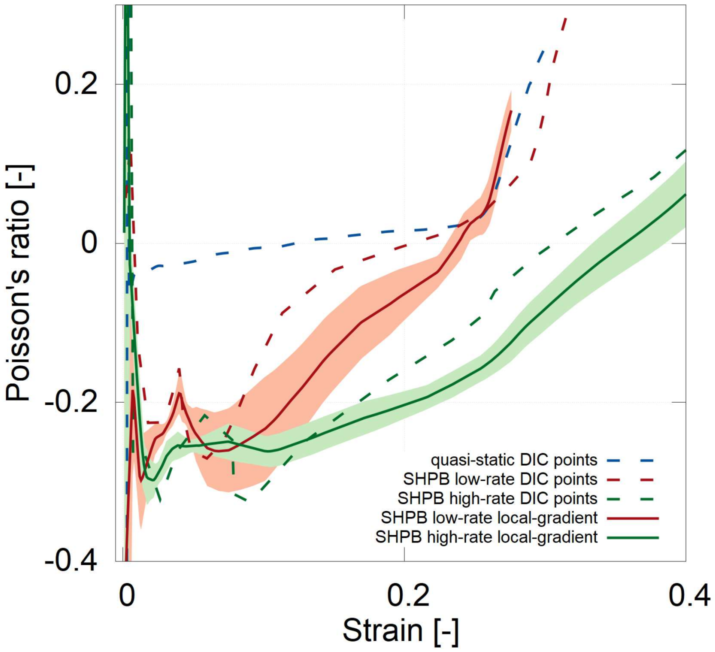

Figure 5.31: The missing-rib structure - the DIC evaluated functions of Poisson's ratio, the solid lines – the local-gradient method, the dashed lines - the inner-inner method.

5.4.5 Comparison of all the methods

The comparison of the results calculated by all three methods is shown in Fig. 5.32 (the 2D re-entrant honeycomb), Fig. 5.33 (the 3D re-entrant honeycomb) and Fig. 5.34 (the missing-rib structure). The solid lines represent the curves estimated by the inner-inner method, the dashed lines represent curves estimated by the outer-outer method and the dotted lines represent curves estimated by the local-gradient method. As can be seen in all the figures, the results of all the three methods are in good agreement and exhibit very similar trends. The only significant difference can be found in the quasi-static curves of the 3D re-entrant lattice. Here, Poisson's ratio evaluated by the outer-outer method is considerably higher than the estimation of the inner-inner method and is close to zero in the whole range of the deformation.

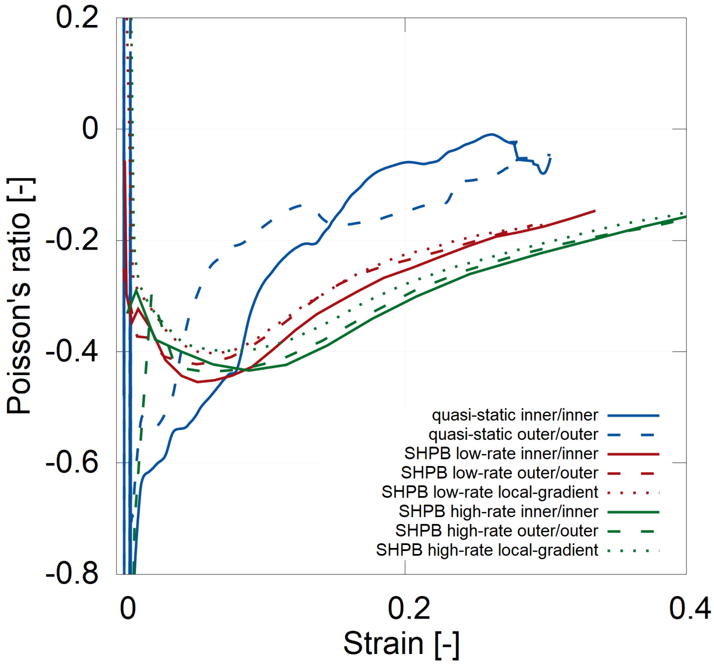

Figure 5.32: The 2D re-entrant honeycomb - the comparison of the function of Poisson's ratio calculated by all the methods, the solid line - the inner-inner, the dashed line - the outer-outer, the dotted line – the local-gradient.

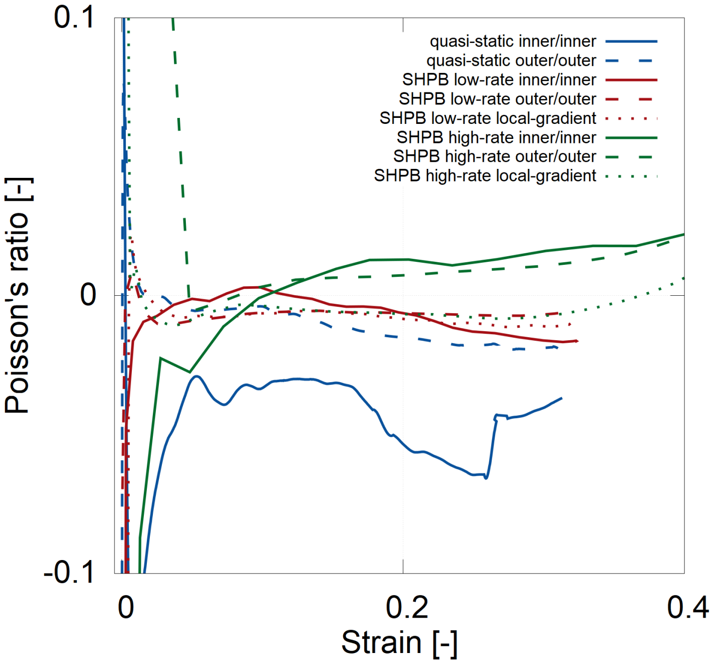

Figure 5.33: The 3D re-entrant honeycomb - the comparison of the function of Poisson's ratio calculated by all the methods, the solid line - the inner-inner, the dashed line - the outer-outer, the dotted line – the local-gradient.

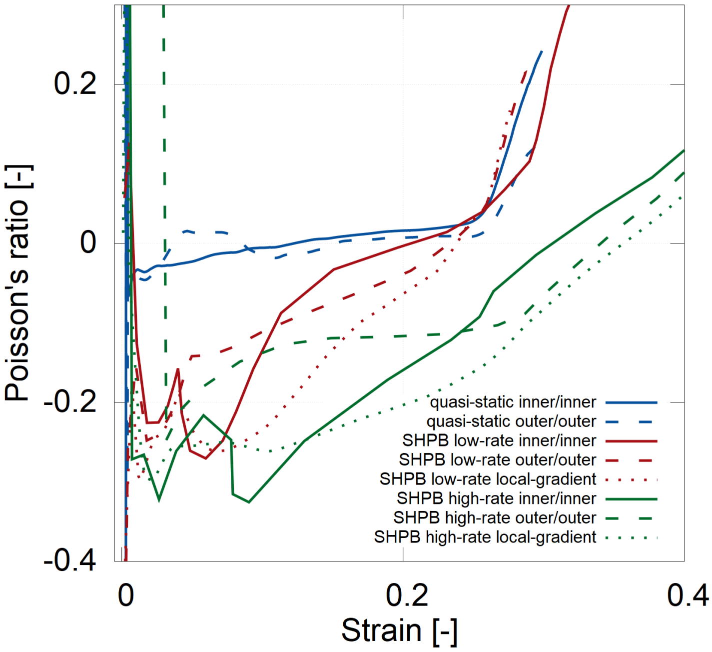

Figure 5.34: The missing-rib structure - the comparison of the function of Poisson's ratio calculated by all the methods, the solid line - the inner-inner, the dashed line - the outer-outer, the dotted line – the local-gradient.

5.5 Campaign 2 - summary

- Campaign 2 is the main experimental program of this study investigating the influence of the micro-inertia, friction and strain-rate related effects in the auxetic lattices subjected to the dynamic compression in Hopkinson bar experimental device.
- The specimens were successfully tested by both SHPB and OHPB.
- The experiments were carefully optimized and the results were reliable and consistent.
- The strain-rate related effects were identified in all the tested auxetic structures.
- The strain energy density of all three tested structures monotonically increased with the strain-rate.
- Different collapse mechanisms were observable under the different strain-rates.
- The DIC was successfully employed for the evaluation of the in-plane displacement and strains.
- Three different methods were used for the evaluation of the function of Poisson's ratio using DIC.
- Poisson's ratio was identified as being both strain and strain-rate dependent with all three employed methods.

5.6 Campaign 3 - Strain-rate sensitivity Short samples 6×3

Shortened versions of the specimens tested in Campaign 2 were also manufactured. The shortened specimens were originally produced as specimens for the testing at very high strain-rates using the SHPB. With the identical setup, the higher strain-rate can be achieved with a shortened specimen (to some point). However, as the response of the specimens was affected by the size effects related to the limited number of cells and different boundary conditions, the specimens were used for the supplementary experimental campaign using the OHPB. The specimens were tested using the identical OHPB setup as was used in Campaign 2 with the identical parameters and settings for the high-speed imaging. As the specimens were short, it was possible to test their response at a wide range of strain-rates (approx. $250 - 2700\,\mathrm{s}^{-1}$) using the single OHPB setup.

5.6.1 Experiments

The specimens were subjected to an impact at the velocities of $7\,\mathrm{ms}^{-1}$, $12\,\mathrm{ms}^{-1}$ and $19\,\mathrm{ms}^{-1}$ resulting in three strain-rates (depending on the type of the structure) of approx. $250 - 800\,\mathrm{s}^{-1}$ (strain-rate 1), $600 - 1500\,\mathrm{s}^{-1}$ (strain-rate 2) and $1500 - 2700\,\mathrm{s}^{-1}$ (strain-rate 3). In the campaign, five specimens were tested per strain-rate for sufficient statistics. The behavior of all the specimens in OHPB was consistent and stable.

2D re-entrant

The average stress-strain and strain-rate to strain diagrams for the 2D re-entrant are shown in Fig. 5.35. With an increasing strain-rate, the collapse occurred at higher strains and a higher stresses exhibiting a similar trend as the longer specimens. The calculated strain energy density for the strain ranging from 0 to 0.20 for all the strain-rates and ratios related to the quasi-static value are shown in Tab. 5.6. The strain energy density plotted against the strain-rate is shown in Fig. 5.36.

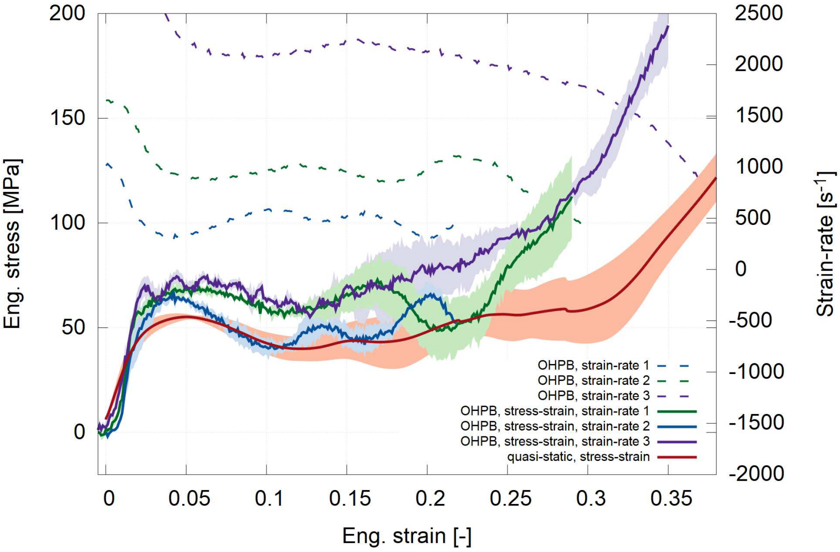

Figure 5.35: The 2D re-entrant, short - the average stress-strain and strain-rate to strain diagrams.

Nominal strain-rate $[\mathrm{s}^{-1}]$	Strain energy density (strain $0-0.15$) $[\mathrm{MJm}^{-3}]$	Ratio $[-]$
Quasi-static	8.43	1.00
≈ 500	9.65	1.15
≈ 1000	11.96	1.42
≈ 2000	12.84	1.52

Table 5.6: The 2D re-entrant, short - the calculated strain energy density for the strain ranging from 0 to 0.20 for all the strain-rates and ratios related to the quasi-static value.

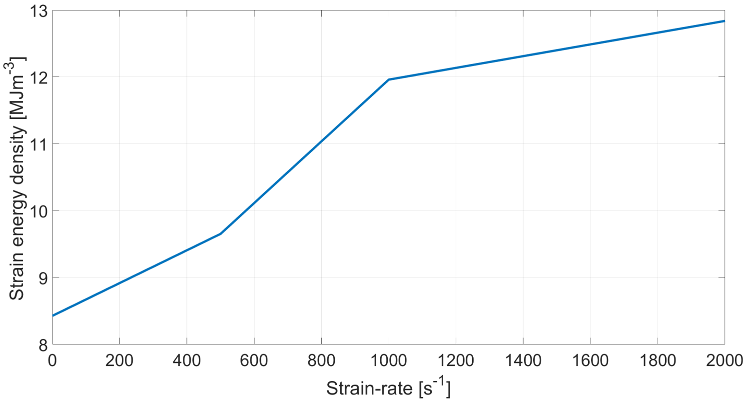

Figure 5.36: 2D re-entrant, short - strain energy density plotted against strain-rate.

5.6.2 3D re-entrant

The average stress-strain and strain-rate to strain diagrams for the 3D re-entrant are shown in Fig. 5.37. The 3D re-entrant exhibited very similar behavior as that of the longer version of the specimen and was again the most stiffest structure. The calculated strain energy density for the strain ranging from 0 to 0.20 for all the strain-rates and ratios related to the quasi-static value are shown in Tab. 5.7. The strain energy density plotted against the strain-rate is shown in Fig. 5.38.

Nominal strain-rate [s^{-1}]	**Strain energy density** (strain $0-0.15$) [MJm^{-3}]	**Ratio** [$-$]
Quasi-static	14.01	1.00
$\approx$ 250	17.26	1.23
$\approx$ 600	19.43	1.39
$\approx$ 1500	20.61	1.47

Table 5.7: The 3D re-entrant, short - the calculated strain energy density for the strain ranging from 0 to 0.20 for all the strain-rates and ratios related to the quasi-static value.

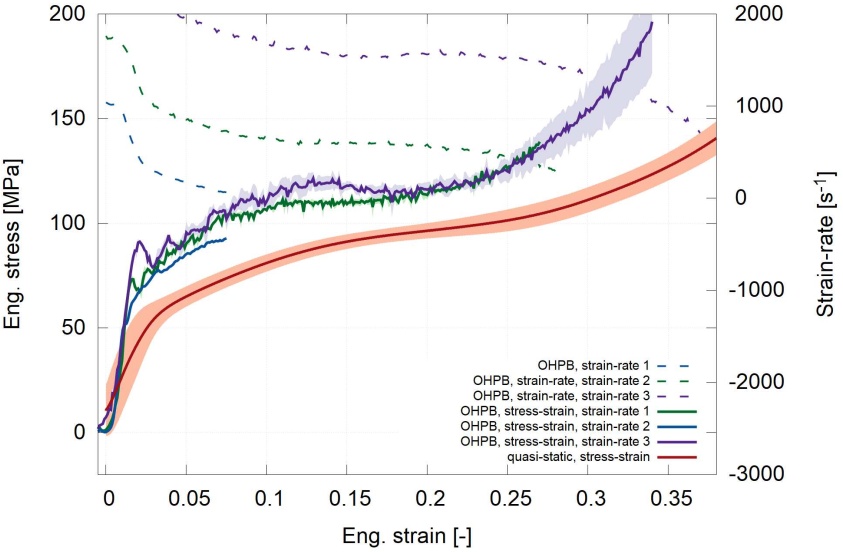

Figure 5.37: The 3D re-entrant, short - the average stress-strain and strain-rate to strain diagrams.

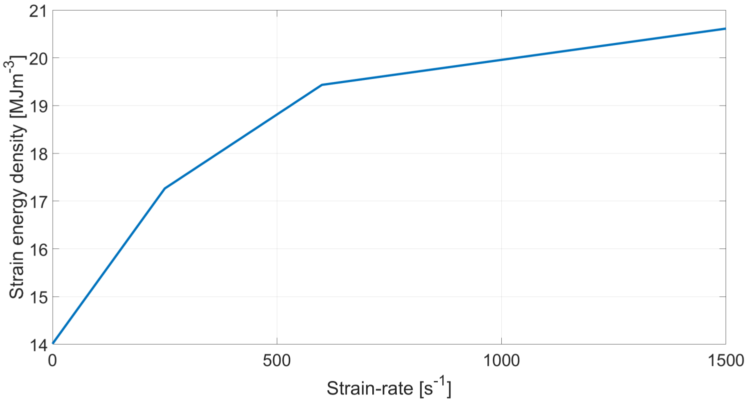

Figure 5.38: The 3D re-entrant, short - the strain energy density plotted against the strain-rate.

5.6.3 Missing-rib

The average stress-strain and strain-rate to strain diagrams for the missing-rib are shown in Fig. 5.39. The missing-rib exhibited very different behavior than the longer version of the specimen. The change in the behavior is related to the more constrained layers of the shortened specimen. The longer version of this structure exhibited very large lateral displacements. However, the lateral displacements in the short specimen are suppressed because of the higher lateral stiffness of the specimen causing the similar behavior to the longer version of the 2D re-entrant. Here, the strain-rate hardening is related to the collapse of the first layer. The calculated strain energy density for the strain ranging from 0 to 0.20 for all the strain-rates and ratios related to the quasi-static value are shown in Tab. 5.8. The strain energy density plotted against the strain-rate is shown in Fig. 5.40.

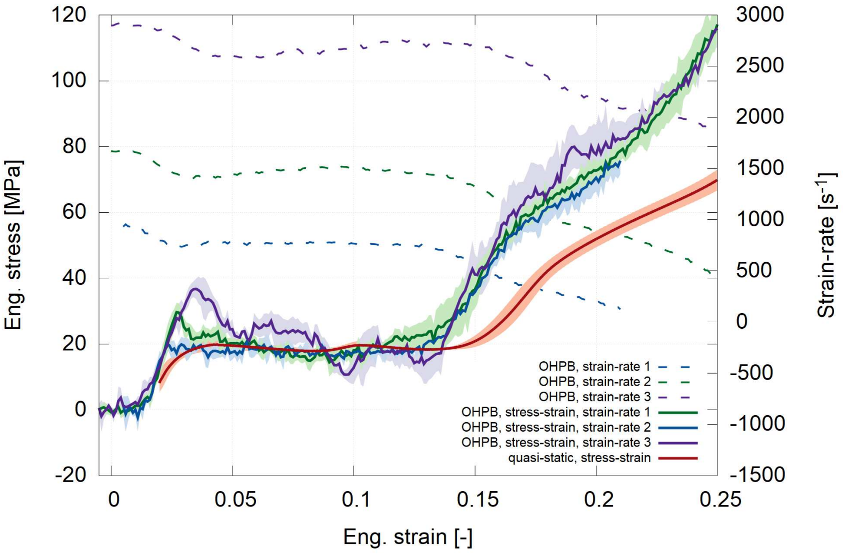

Figure 5.39: The missing-rib, short - the average stress-strain and strain-rate to strain diagrams.

Nominal strain-rate	Strain energy density	Ratio
	(strain $0 - 0.15$)	
[s^{-1}]	[MJm^{-3}]	[$-$]
Quasi-static	4.26	1.00
≈ 800	5.43	1.28
≈ 1500	5.81	1.36
≈ 2700	6.30	1.48

Table 5.8: The missing-rib, short - the calculated the strain energy density for strain ranging from 0 to 0.20 for all the strain-rates and ratios related to the quasi-static value.

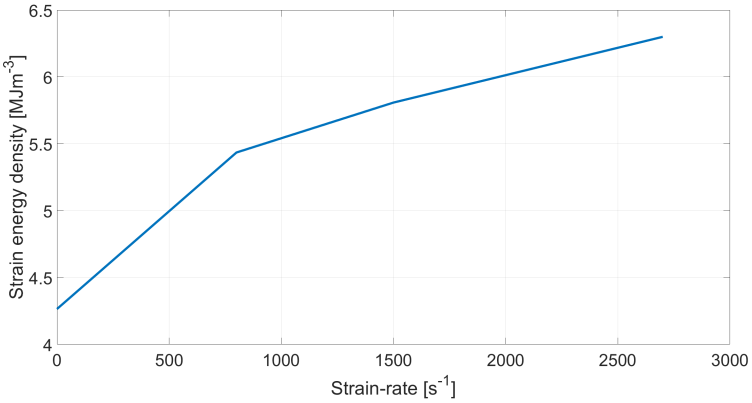

Figure 5.40: The missing-rib, short - the strain energy density plotted against the strain-rate.

5.7 Strain-rate sensitivity - summary

The specific strain energy density ratio was calculated using the approach identical to Section 5.3.3. The specific strain energy density ratio of all the short structures plotted against the nominal strain-rate is shown in Fig. 5.41. All the structures exhibit a similar trend to the strain-rate sensitivity with a monotonically increasing specific strain energy density ratio. The specific strain energy density ratio of all the (short and long) structures plotted against the nominal strain-rate is shown in Fig. 5.42. The strain-rate sensitivity trend is comparable for both the long and short specimens. Both versions of the structures exhibited non-linear dependency to the specific strain energy density ratio on the strain-rate in the tested range of the strain-rates. Note that the logarithmic fit is included for illustration purposes only, as the comparison of the strain energy density is relative and does not include any physics-related model. The fit is used to highlight the possible trend.

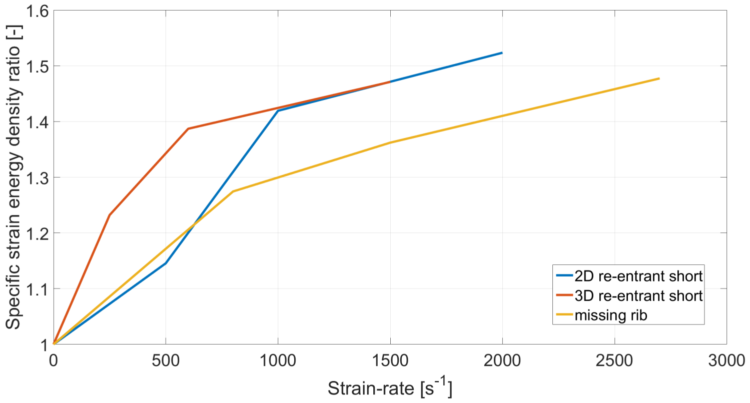

Figure 5.41: All the short structures - the specific strain energy density ratio plotted against the strain-rate.

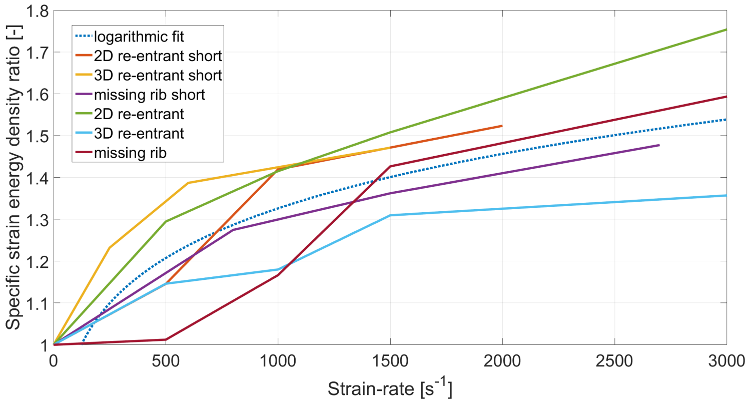

Figure 5.42: All the structures (short and long) - the specific strain energy density ratio plotted against the strain-rate.

5.8 Campaign 3 - summary

- Shortened versions of three auxetic lattices were tested using OHPB at three different strain-rates.
- Testing in the OHPB produced consistent and reliable results.
- The strain-rate sensitivity of the structures exhibited similar trends to the specimens from Campaign 2.

5.9 Campaign 4 - Testing at different temperatures - SLS Auxetics

The dynamic testing of the SLS stainless steel auxetic lattices at different temperatures was performed in this study. In this campaign, a 2D re-entrant auxetic lattice with a similar geometry to Campaign 1 was used. The arrangement with 4 × 5 cells and thick cell (0.6 mm) walls was selected to maximize the thermal related effects in the material. The auxetic lattices were tested at two different strain-rates and three different temperatures to evaluate the possible strain-rate and thermal related hardening effects. For more information, please refer to our contribution [6].

5.9.1 Experimental setup

A conventional SHPB apparatus was used for the compression of the specimens at two different strain-rates. High-strength aluminum alloy bars (EN-AW-7075-T6) with a diameter of 20 mm were used in the experiments. A striker bar with length of 750 mm was accelerated using a gas-gun system. The striker impact velocities used in the experiments were $30\,\mathrm{ms}^{-1}$ and $45\,\mathrm{ms}^{-1}$. The incident and the transmission bar had the same length of 1600 mm. Both bars were equipped with one measurement point located in the middle of the bar to prevent wave superposition at the strain-gauge. A pulse-shaping technique using cylindrical soft copper shapers mounted on the incident bar impact face was employed. The impact was observed by a pair of Fastcam SA-Z high-speed cameras. The cameras were used to record the in-plane auxetic deformation of the specimen at a resolution of 256 × 168 px and approx. 252 kfps and to observe the overall scene. The images of this camera were used for the DIC analysis to calculate the displacement and the strain fields. A speckle pattern was applied on both ends of bars for the DIC of their movement during the experiment. The heating and cooling stages, described in detail in Section 4.11, were used for the heating and cooling of the specimen. The specimens were tested at three different temperatures: room temperature ($\approx 25\,^\circ\mathrm{C}$), elevated temperature ($\approx 120\,^\circ\mathrm{C}$) and low temperature ($\approx -5\,^\circ\mathrm{C}$).

The thermal behavior was observed by a SC7600 IR camera described in detail in Section 4.11. The image resolution was 94 × 44 px at frame rate of approx. 2 kfps.

5.9.2 Results

The plot showing the strain-rate and temperature related dependency of the stress-strain curve for all temperatures and both used strain-rates is shown in Fig. 5.43. The combined temperature and strain-rate related hardening effects are shown in Fig. 5.44, where the value of the mean plateau stress is plotted against the strain-rate. As can be seen, the auxetic structure made of the powdered austenitic steel exhibited both strain-rate and temperature related hardening effects (thermal softening). The results are important for the further complex investigation of the material behavior and for the relevant advanced material model for the numerical simulations.

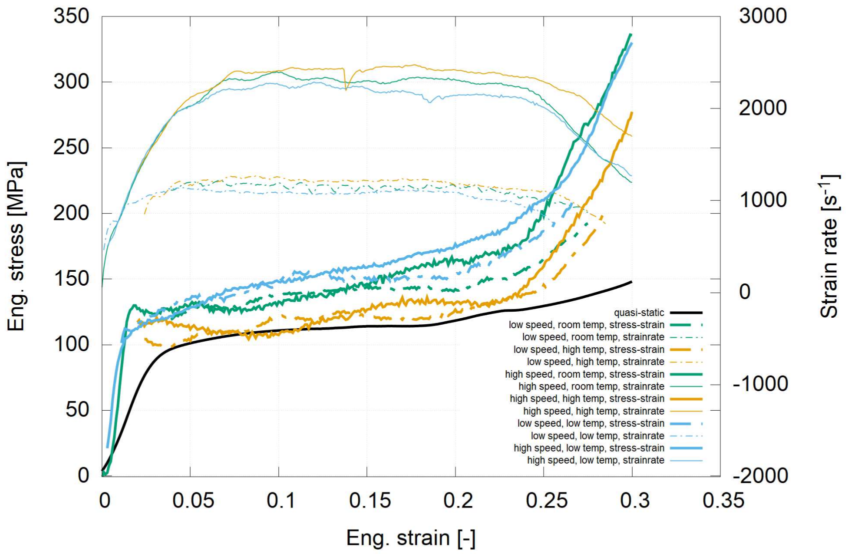

Figure 5.43: The strain-rate and temperature related dependency of the stress-strain curve for all the temperatures and all the strain-rates.

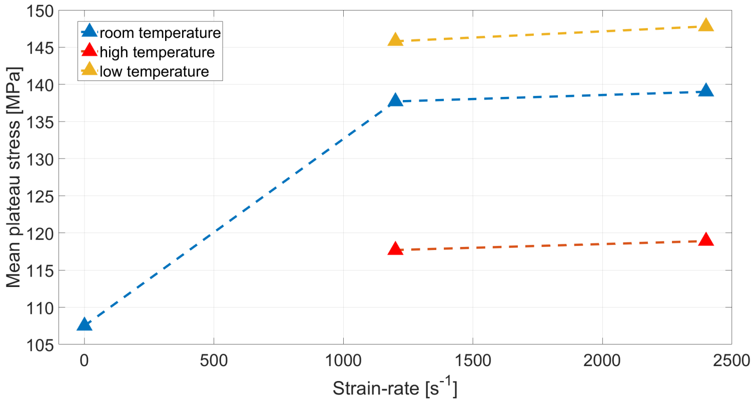

Figure 5.44: The combined temperature and strain-rate related hardening effects.

5.10 Campaign 4 - summary

- The 2D re-entrant auxetic lattices were tested at three different temperatures and two different strain-rates in the SHPB.
- Both the strain-rate hardening and thermal softening were identified in the results.

5.11 Campaign 5 - Hybrid Ni/Pu foams

The hybrid Ni/Pu open-cell foam was tested in dynamic compression using SHPB. Two sizes of the specimens were tested in this experimental campaign. However, the specimens had low impedance and the measurement using the aluminum bars was not trivial. Based on the results of this experimental campaign, it was decided to start experimenting with visco-elastic bars and direct impact methods. This resulted in the introduction of the OHPB experimental setup.

5.11.1 Experimental setup

The identical setup, as in Campaign 1, was used for the testing of the hybrid foams. The striker impact velocities were in the range from $20\,\mathrm{ms^{-1}}$ to $45\,\mathrm{ms^{-1}}$. Copper pulse shapers with diameters from 12 mm to 18 mm and a thickness of 1.5 mm were used. The specimens were observed using a Fastcam SA-5 high-speed camera with the identical settings to Campaign 1. A hybrid foam specimen mounted in the experimental setup is shown in Fig. 5.45.

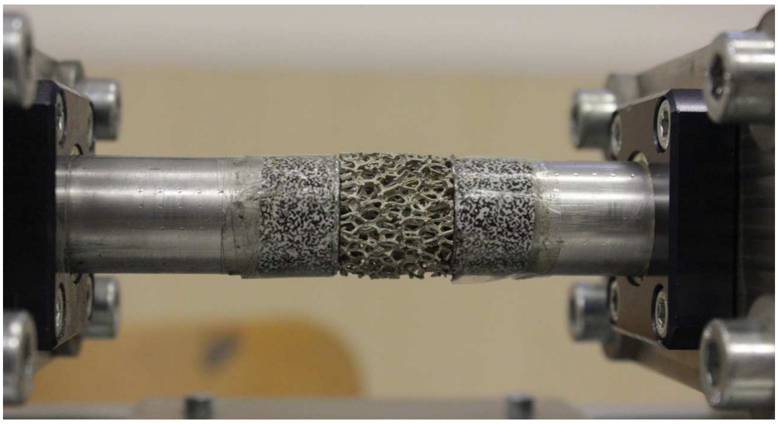

Figure 5.45: The hybrid foam specimen mounted in the experimental setup.

5.11.2 Representative results

The slideshow of the deforming foam in the SHPB is shown in Fig. 5.46. The typical recorded dynamic equilibrium is shown in Fig. 5.47. Note the long time period before establishing the force convergence related to the long and low impedance specimens. The comparison of the stress-strain diagram, where the strain was evaluated using a strain-gauge and using the DIC tracking of the bars, is shown in Fig. 5.48.

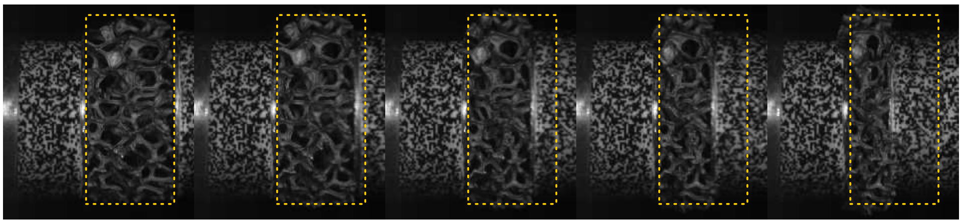

Figure 5.46: The slideshow of the deforming hybrid foam in the SHPB.

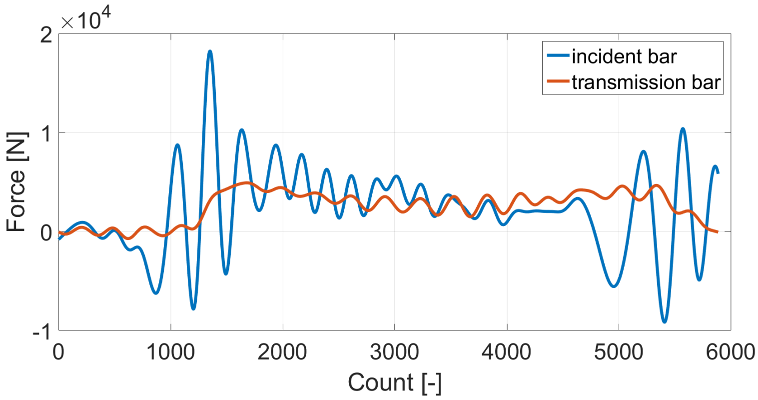

Figure 5.47: The typical recorded dynamic equilibrium of the hybrid foam.

5.11.3 Stress-strain diagrams

The stress-strain diagrams for both the short and long hybrid foam specimens calculated with respect to the specimen's density are shown in Fig. 5.49 and Fig. 5.50. Size effect related problems were observed in the results as the size of the specimens were smaller than the representative volume element (RVE) of the hybrid foam. Strain-rate related hardening was not observed in the applied range of strain-rates.

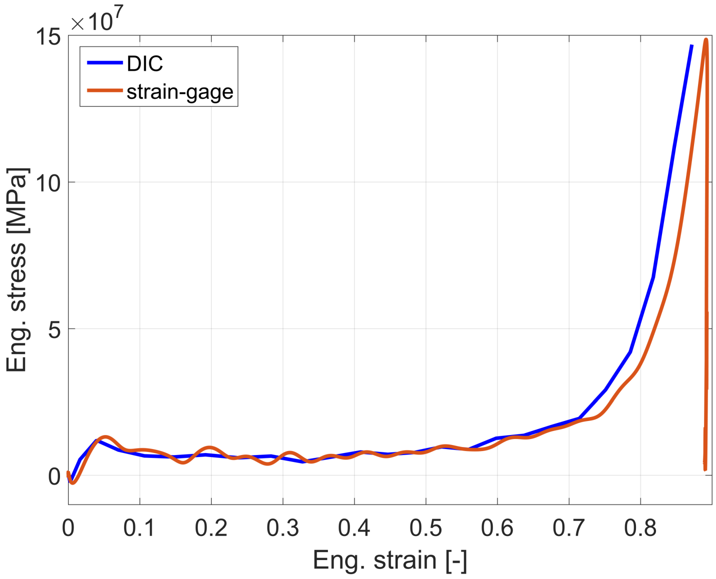

Figure 5.48: The hybrid foam - the comparison of the stress-strain diagram, where the strain was evaluated using a strain-gauge and using the DIC tracking of the bars.

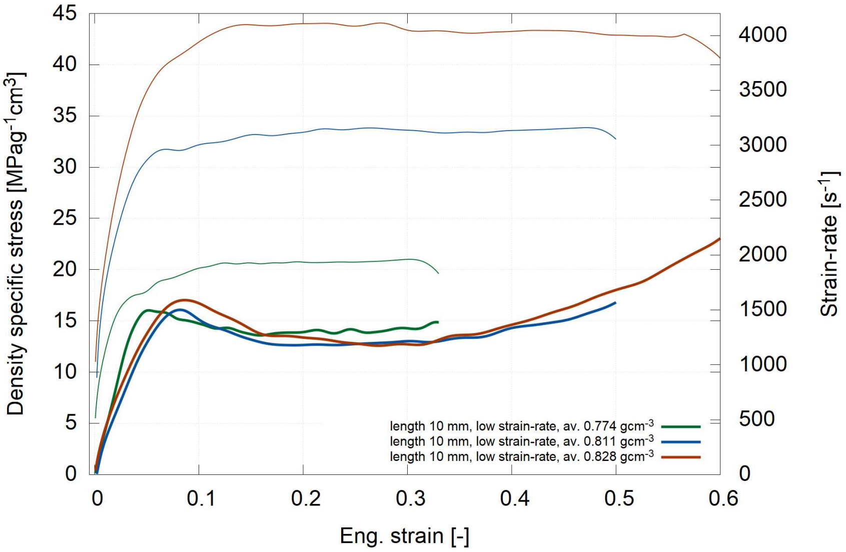

Figure 5.49: The hybrid foam, the short specimens - the stress-strain diagram calculated with respect to the specimen's density.

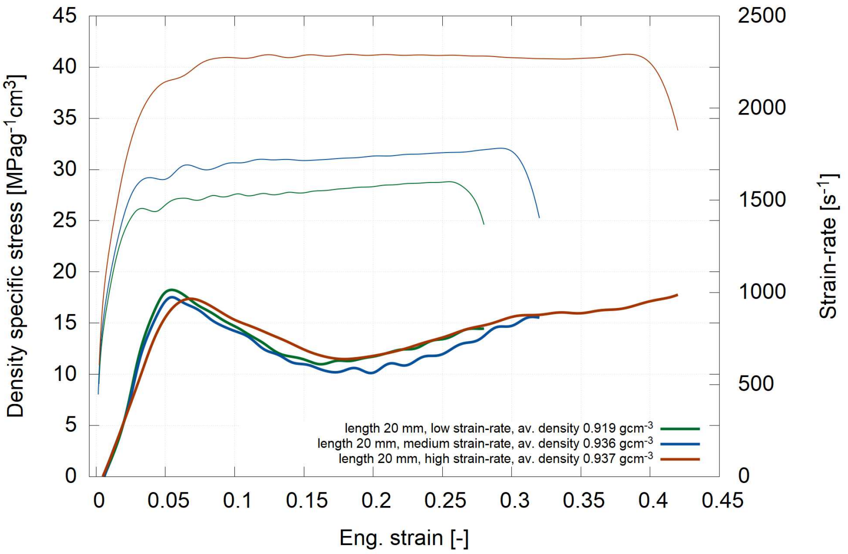

Figure 5.50: The hybrid foam, the long specimens - the stress-strain diagram calculated with respect to the specimen's density.

5.12 Campaign 5 - summary

- Hybrid auxetic lattices with nickel coating and polyurethane core were tested using SHPB.
- The specimens were found to have low impedance in comparison with the setup impedance.
- Size effect was identified in the tested specimens.
- No strain-rate sensitivity and micro-inertia effects were identified in the range of the applied strain-rates.

5.13 Campaign 6 - Hybrid Ni/polymer auxetic structures

Hybrid Ni/polymer auxetic lattices (see Section 4.1.3) were tested in this campaign. Two types of hybrid auxetic structures with a polymeric core and a nickel coating were tested using dynamic compression. Three types of specimens were prepared: base structure specimens without a coating, specimens with a 60 μm coating layer thickness, and with a 120 μm coating layer thickness. A complex experimental investigation was performed for the evaluation of the material properties, deformation mechanisms, energy dissipation and heat transfer effects at the different strain-rates. For the dynamic experiments, the OHPB apparatus was used for the compression of the specimens at two different strain-rates. Only the selected representative results are shown in this thesis. For more details, please refer to the related contribution [5].

5.13.1 Experimental setup

Due to the low mechanical impedance of the samples, PMMA bars with a diameter of 20 mm were used. The length of both bars was 1750 mm. One measurement point was created on the incident bar, two measurement points were created on the transmission bar. Each measurement point consisted of two pairs of strain-gauges in the Wheatstone half-bridge arrangement. The first pair was equipped with foil strain-gauges 3/120 LY61 (HBM, Germany) with a 3 mm active length, whereas the second pair was equipped with semiconductor strain-gauges AFP-500-090 (Kulite, USA) with a 2.29 mm active length. The length of the track was 1200 mm. The experiments were simultaneously observed by a synchronized pair of Fastcam SA-Z high-speed cameras and by a SC7600 thermal imaging camera. The hybrid auxetic specimens were tested at two nominal strain-rates corresponding approximately to 400 s^{-1} and 800 s^{-1}. Reaching an identical nominal strain-rate in all the experiments required a different impact velocity for each type of coating. Thus, the impact velocities varied from approx. 5 ms^{-1} to approx.

$26\,\mathrm{ms}^{-1}$. The experiments were observed by the high-speed cameras with a resolution of 256×168 px at approx. 252 kfps. The thermal response of the samples during the impact, heat transfer, and heat dissipation effects were observed using the thermal imaging camera with a resolution of 94×44 px at a frame rate of approx. 2 kfps. The experimental setup is shown in Fig. 5.51.

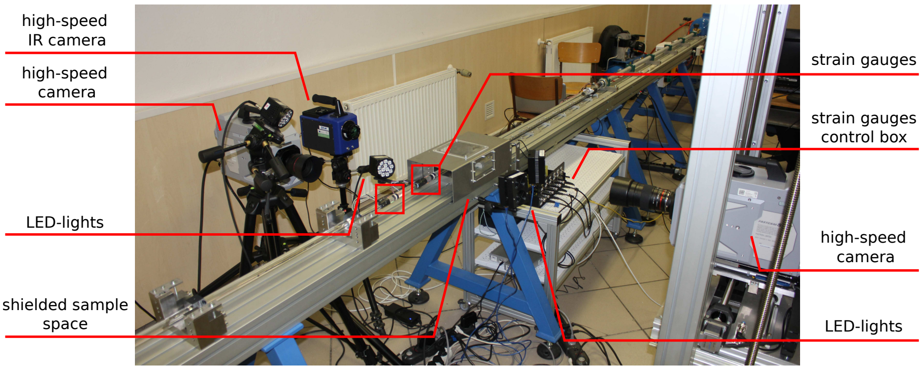

Figure 5.51: The experimental setup for the hybrid Ni/polymer auxetic structures.

5.13.2 Representative results

The slideshow of the deforming hybrid auxetic structure in the OHPB is shown in Fig. 5.52. In this campaign, forces as low as 100 N were successfully measured using the PMMA bars. The full-field DIC results of the longitudinal strain of the specimen with the $60\,\mu$m coating are shown in Fig. 5.53. Note the initial gap between the specimen and the incident bar that subsequently impacts the specimen directly. The typical dynamic equilibrium is shown in Fig. 5.54. The illustrative images showing the influence of the strain-rate and coating thickness on the heat distribution are presented in Fig. 5.55. The comparison of the incident and transmission stress-strain diagrams of the specimen with the $60\,\mu$m coating evaluated using the strain-gauges (solid lines) with diagrams where strain was evaluated using the DIC (dotted lines) is presented in Fig. 5.56. Note that the strains evaluated from DIC are in very good agreement with the strain-gauges.

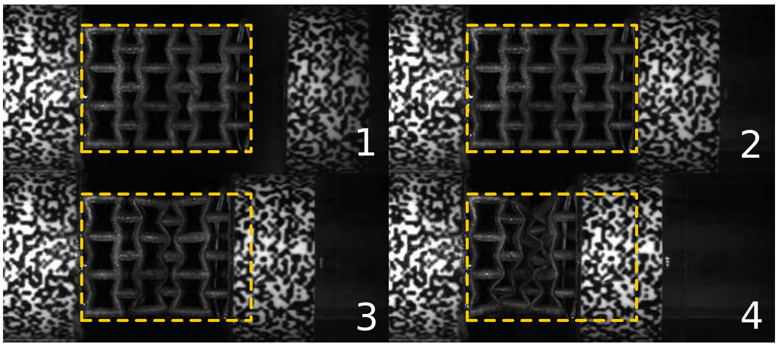

Figure 5.52: The slideshow of the deforming hybrid auxetic structure in the OHPB.

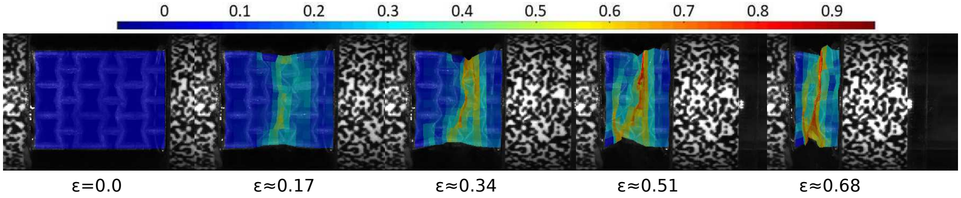

Figure 5.53: The full-field DIC results of the longitudinal strain of the specimen with the 60 μm coating at a high-rate.

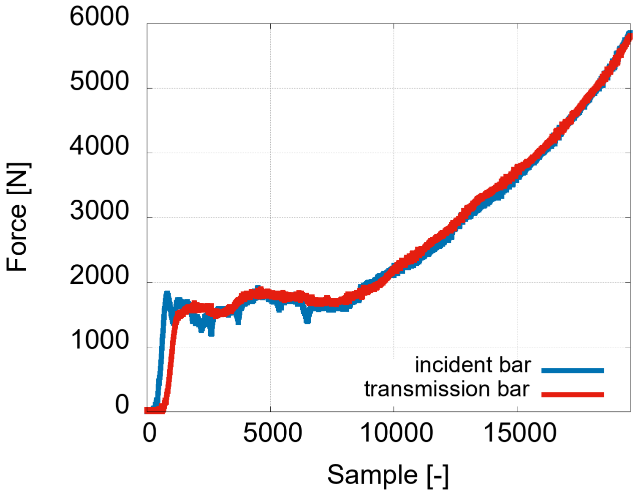

Figure 5.54: The typical dynamic equilibrium. The signals are presented as measured and are not time-shifted revealing one of the advantage of the OHPB.

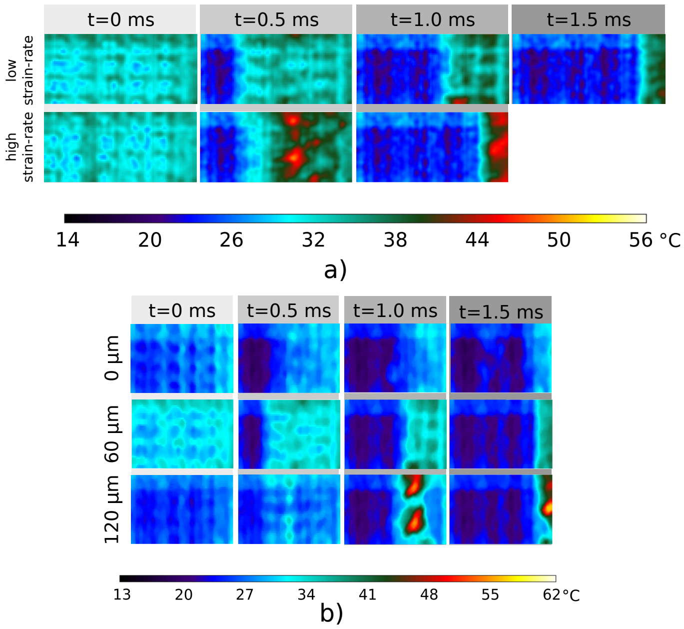

Figure 5.55: The illustrative images showing the influence of the strain-rate and coating thickness on the heat distribution: (a) the influence of the strain-rate on heat distribution of the specimens with the 60 μm coating, (b) the influence of the coating thickness on the heat distribution of the specimens at low strain-rate.

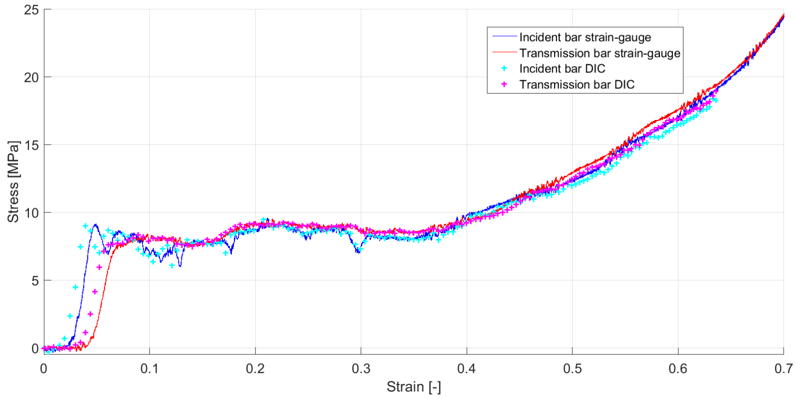

Figure 5.56: The comparison of the incident and transmission stress-strain diagrams of the specimen with the 60 μm coating evaluated using strain-gauges (solid lines) with diagrams, where the strain was evaluated using DIC (dotted lines).

5.13.3 Stress-strain diagrams

The representative stress-strain diagrams of the structure without the coating and with the coating thickness of 60 μm and 120 μm tested at two strain-rates are shown in Fig. 5.57. The non-coated specimens exhibited instant disintegration without any strain-rate hardening. The structures with the coating exhibited plastic behavior without any strain-rate hardening effects. No effects of the micro-inertia could be detected in the data as the structures had hollow struts with low mass and various imperfections were present in the coating.

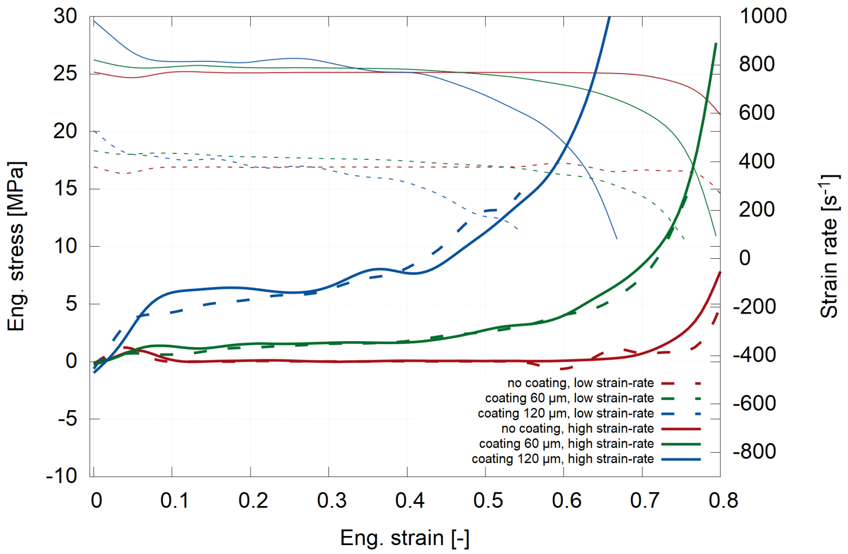

Figure 5.57: The representative stress-strain diagrams of the hybrid auxetic structure without the coating and with the coating thickness of 60 μm and 120 μm.

5.14 Campaign 6 - summary

- Hybrid auxetic lattices with a nickel coating and polymeric core were tested using OHPB with visco-elastic bars.
- The experimental setup was optimized for low impedance materials.
- Forces as low as 100 N were successfully measured with the PMMA bars.
- No strain-rate sensitivity and micro-inertia effects were identified in the range of applied strain-rates.
- Although the specimens had lower impedance than the hybrid foam structures (Campaign 5) their behavior was measured reliably using the OHPB with the visco-elastic bars.

5.15 Representative DIC results

The representative and interesting high-speed images and results evaluated by the DIC are shown in this section.

5.15.1 Longitudinal and lateral displacements

The development of the longitudinal and lateral displacements showing the auxetic effect in the hybrid nickel auxetic structure is presented in Fig. 5.58.

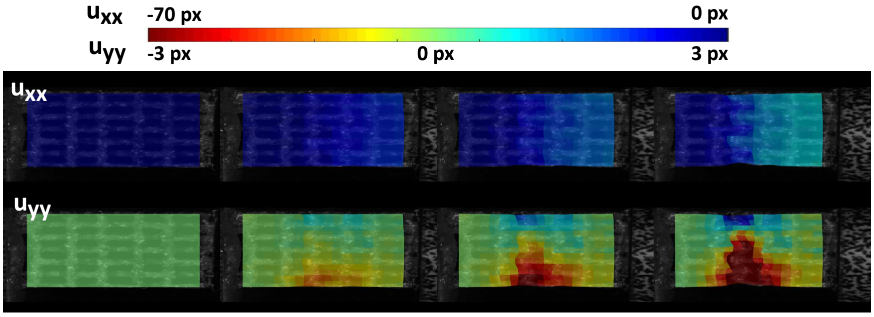

Figure 5.58: The development of the longitudinal (first row) and the lateral displacements (second row) showing the auxetic effect in the hybrid nickel auxetic structure.

5.15.2 Auxetic structure - comparison between elastic bars, visco-elastic bars and DIC

The missing-rib structure investigated in Campaign 2 (see Section 5.3) was tested using both aluminum bars and PMMA visco-elastic bars. The comparison of the stress-strains curves evaluated using the aluminum and PMMA bars at approximately the same strain-rate is shown in Fig. 5.59. The results from both bars are comparable and consistent. A complex DIC analysis was performed during the experiments to compare the strain-gauges data with the image based results.

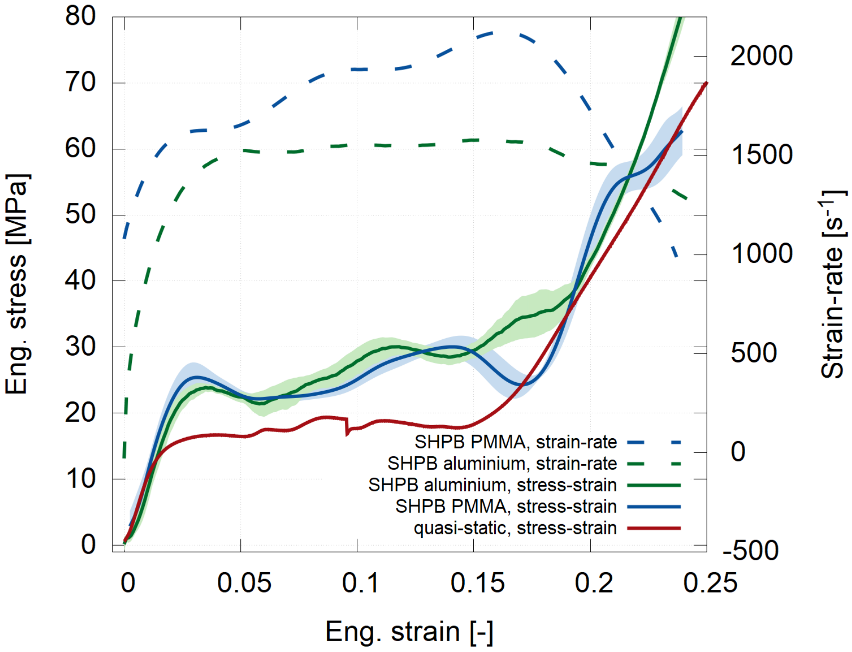

Figure 5.59: The stress-strain and strain-rate to strain curves derived from the SHPB with the aluminum and PMMA bars compared to the quasi-static experiments.

Strain using DIC

An identical grid consisting of 26 × 17 correlation points covering the area of the sample and the end parts of the measurement bars was placed on the high-speed camera images. The grid was tracked using DIC and the new positions of the grid points were identified in every captured image. The high-speed camera images were converted from a raw format to 8-bit PNG by a lossless compression algorithm and were not subjected to any additional pre-processing. In all the cases, the DIC was successful with a mean correlation coefficient at 95.7 % in the worst case. In every experiment, some of the points lost the relevant correlation, particularly the points located on the side edges of the specimen. Based on the image correlation results, four strain values valid for the different parts of the specimen were calculated. The geometric configuration used for the calculation of four different strains is shown in Fig. 5.60. The following strains were calculated from the mean displacement evaluated at the lines shown in Fig. 5.60:

$$\epsilon_{\mathrm{xx_b}} = \frac{u_{11} - u_{12}}{L_{\mathrm{i2}}}, \tag{5.2}$$

$$\epsilon_{\mathrm{xx_e}} = \frac{u_{21} - u_{22}}{L_{\mathrm{i2}}}, \tag{5.3}$$

$$\epsilon_{\mathrm{xx_{in2}}} = \frac{u_{31} - u_{32}}{L_{\mathrm{i3}}}, \tag{5.4}$$

$$\epsilon_{\mathrm{xx_{in3}}} = \frac{u_{41} - u_{42}}{L_{\mathrm{i4}}}, \tag{5.5}$$

where u_{jk} corresponds to the longitudinal displacements and L_{in} corresponds to the initial lengths of the relevant part of the specimen. Thus, $\epsilon_{\mathrm{xx_b}}$ expresses the strain calculated using the image correlation data from the random pattern fixed on the measurement bars, $\epsilon_{\mathrm{xx_e}}$ expresses the strain on the edges of the specimens and the other two ($\epsilon_{\mathrm{xx_{in2}}}$, $\epsilon_{\mathrm{xx_{in3}}}$) are the strain values in the specimen's core.

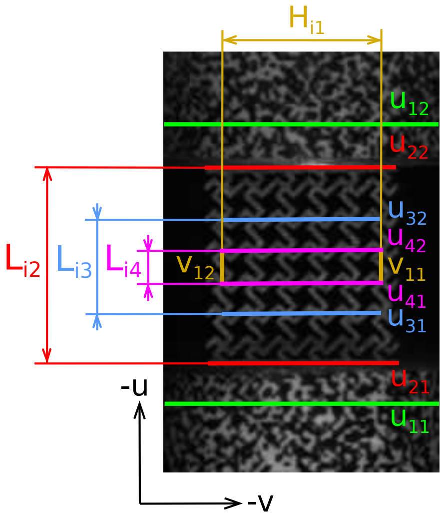

Figure 5.60: The geometric configuration of the correlation grid used for the strain calculations in the different parts of the specimen.

The strain values calculated using Eq. 5.2-5.5 are plotted against the reference strain from the strain-gauge (dashed line) in Fig. 5.61 and Fig. 5.62, showing the strain development in the different parts of the specimen for both the aluminum and PMMA bars. In the case of the aluminum bars, strain $\epsilon_{\mathrm{xx_b}}$ (the strain from the bar's ends) is slightly higher than the reference strain and strain $\epsilon_{\mathrm{xx_e}}$ (the strain from the specimen's edges) corresponds almost perfectly to the reference strain. This difference corresponds to approximately 2 px of the image and can be considered as the image correlation error. Other possible reasons for this can be attributed to a correlation pattern shift during

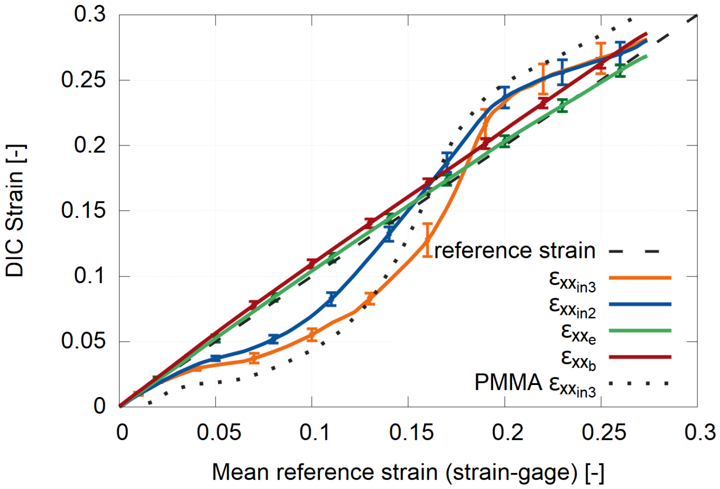

Figure 5.61: The comparison of the different DIC strains with the reference strain-gauge signal - the aluminum bars.

the experiment, optical lens errors or to a minor error in the used mechanical parameters of the bars. Strains $\epsilon_{\mathrm{xx_{in2}}}$ and $\epsilon_{\mathrm{xx_{in3}}}$ show different deformation behavior in the central regions of the specimen as the core deforms with a certain time delay than the boundary parts of the specimen. The dotted line expresses strain $\epsilon_{\mathrm{xx_{in3}}}$ from the PMMA bars (or the aluminum bars, respectively) showing similar trend, but not the same values. The strains from the PMMA experiments in Fig. 5.62 show very good agreement with $\epsilon_{\mathrm{xx_b}}$ and $\epsilon_{\mathrm{xx_e}}$. Moreover, they are in good agreement with the aluminum bars experiments showing a similar deformation behavior.

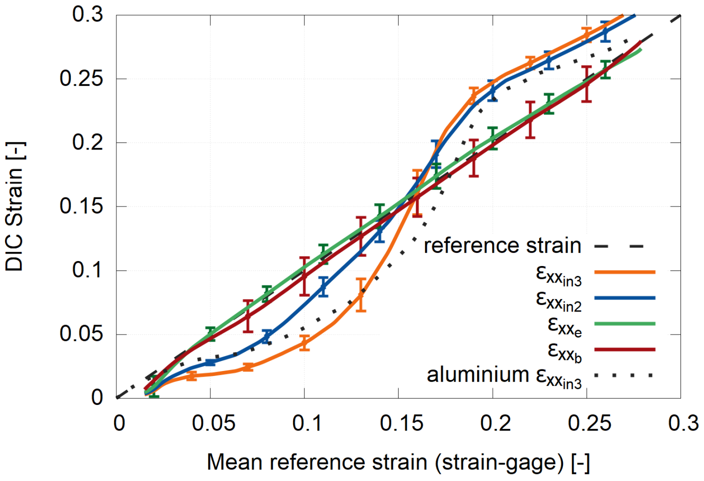

Figure 5.62: The comparison of the different DIC strains with the reference strain-gauge signal - the PMMA bars.

Evaluation of Poisson's ratio from DIC

The average Poisson's ratio of the specimen's core was calculated from the DIC results for both types of the bars. Poisson's ratio was calculated using the longitudinal and transverse displacements averaged per row or column, respectively. The ratio was calculated with the following formula (see Fig. 5.60):

$$\nu_{\mathrm{in3}} = -\frac{L_{\mathrm{i4}}\left(v_{11} - v_{12}\right)}{H_{\mathrm{i1}}\left(u_{41} - u_{42}\right)}. \tag{5.6}$$

The results of Poisson's ratio calculated for both types of experiments are shown in Fig. 5.63. The graph shows the auxetic behavior of the lattice structure. The curves are in good agreement while the results for the aluminum bars express a slightly lower auxetic behavior.

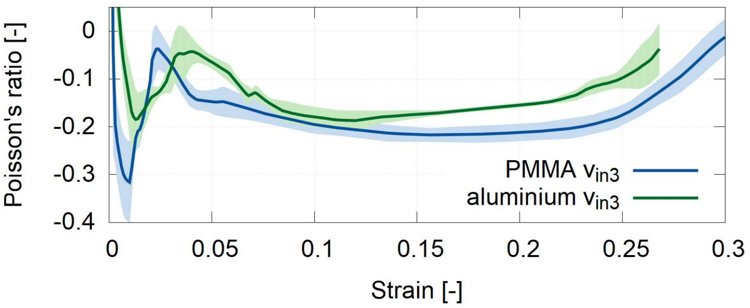

Figure 5.63: The mean Poisson's ratio calculated from the experiments with the aluminum and PMMA bars.

Stress-strain curves using DIC

The stress-strain curves with the strain derived using DIC were calculated for both the aluminum and PMMA bars. The stress-strain graphs using strains $\epsilon_{\mathrm{xx_e}}$ (the specimen's edges) and $\epsilon_{\mathrm{xx_{in3}}}$ (the specimen's core) for both bar types are shown in Fig. 5.64 and Fig. 5.65. In the case of the aluminum bars (Fig. 5.64), the stress-strain curve corresponding to the specimen's edges is almost identical with the strain-gauge curve (dashed line). The stress-strain curve corresponding to the specimen's core exhibits similar trends with the prolonged plateau region. In the case of the PMMA bars (Fig. 5.65), the curve corresponding to the specimen's edges is in very good agreement with the strain-gauge. The differences in the initial parts of the DIC curves to the strain-gauge curve are caused by the low stiffness of the PMMA and the ramp-in effect of the strain wave in the specimen.

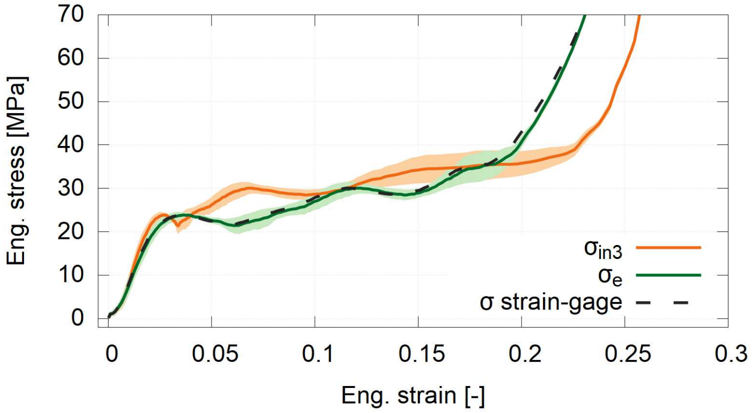

Figure 5.64: The DIC stress-strain curves for the boundary part of the specimen and for the specimen's core compared with the reference strain-gauge signal - the aluminum bars.

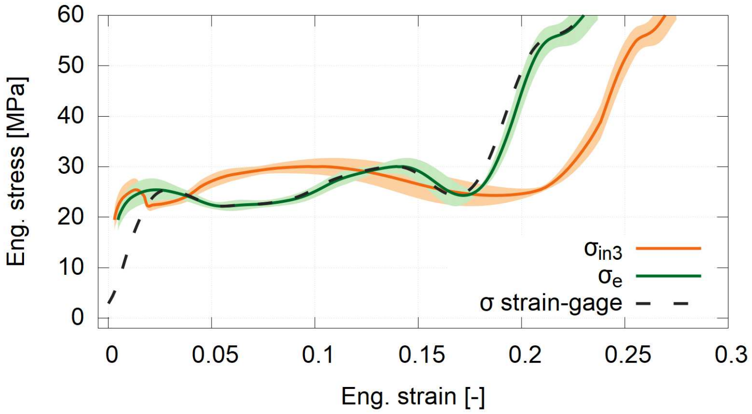

Figure 5.65: The DIC stress-strain curves for the boundary part of the specimen and for the specimen's core compared with the reference strain-gauge signal - the PMMA bars.

Full-field results

The full-field results were calculated using DIC. Using a correlation sub-matrix for each correlation point, it was possible to calculate both the longitudinal and transverse strains for every point in the correlation grid. The strains were then used for the calculation of Poisson's ratio in every correlation point using the standard formula $\nu = -\frac{\epsilon_{yy}}{\epsilon_{xx}}$. An example of the full-field results is shown in Fig. 5.66. The localized strain-fields on both sides of the specimen can be observed in the nominal strain as low as $\epsilon_{\mathrm{xx_e}} = 0.05$ indicating that the experiment was carried out in dynamic equilibrium. In the nominal strain of approximately $\epsilon_{\mathrm{xx_e}} = 0.18$ the deformation is distributed almost uniformly through the specimen. The results of the full-field Poisson's ratio exhibit a very profound auxetic behavior with the ratio reaching approx. -0.3 in the specimen's core. Auxetic behavior can be observed up to the nominal strain of approx. $\epsilon_{\mathrm{xx_e}} = 0.18$ where the structure stops to exhibit auxetic behavior.

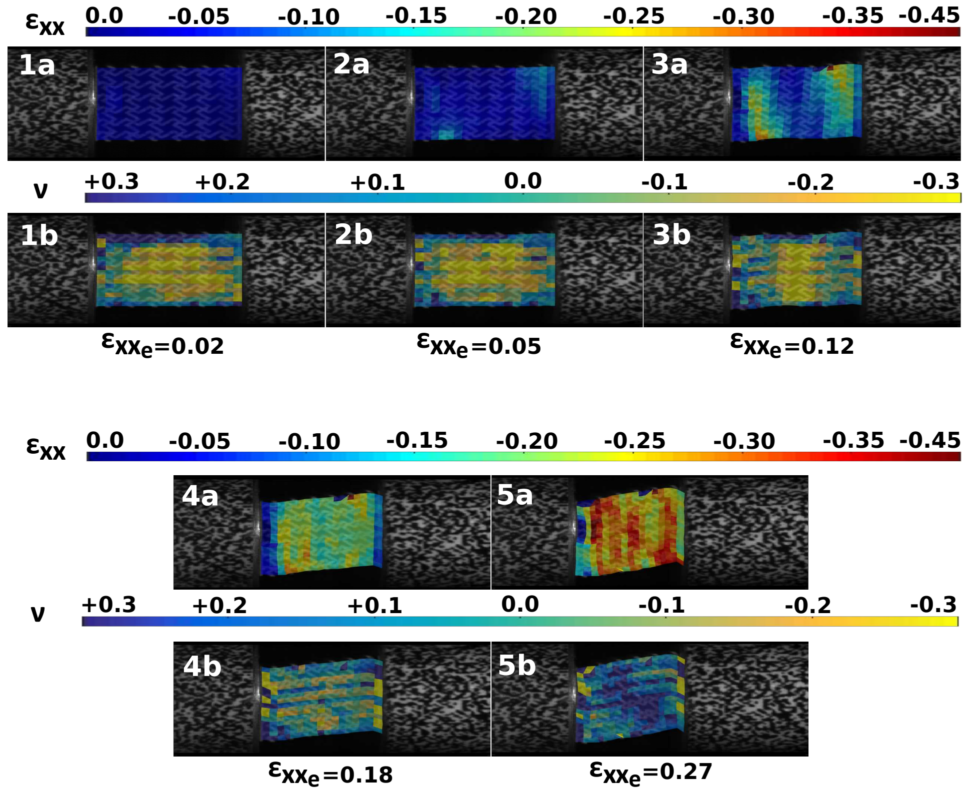

Figure 5.66: The full-field analysis: the in-plane longitudinal strain (first row), the in-plane Poisson's ratio (second row)

5.15.3 Deformed shape and auxetic effect

The development of the auxetic effect is shown in Fig. 5.67. The selected points on the surface of the 2D chiral auxetic lattice (not presented in this work - ongoing research) were tracked using DIC to visualize the auxetic effect and the deformed shape of the specimen.

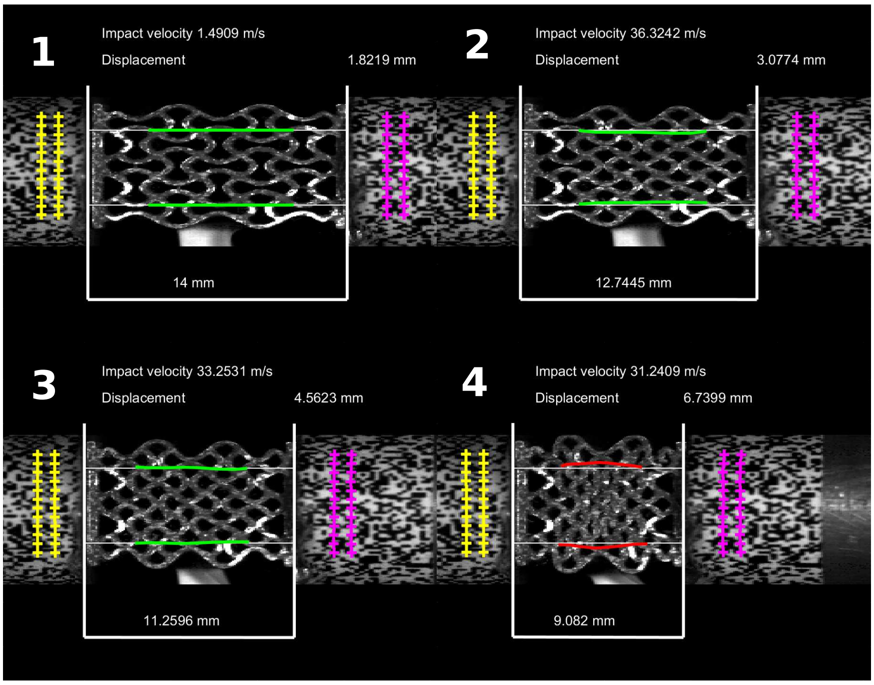

Figure 5.67: The development of the auxetic effect on the surface of the 2D chiral auxetic lattice.

5.16 Results quality

Three experiments of the cubic specimens of the closed-cell aluminum foam Alcoras conducted between years 2016-2019 were selected for the demonstration of the improvements in the measurement quality and reliability. As the representative indicator, dynamic equilibrium forces during these experiments were selected and are shown in Fig. 5.68. The different configuration of the measuring device SHPB/OHPB does not have any primary influence on the quality of recorded signal, unlike the realized instrumentation. Thus,

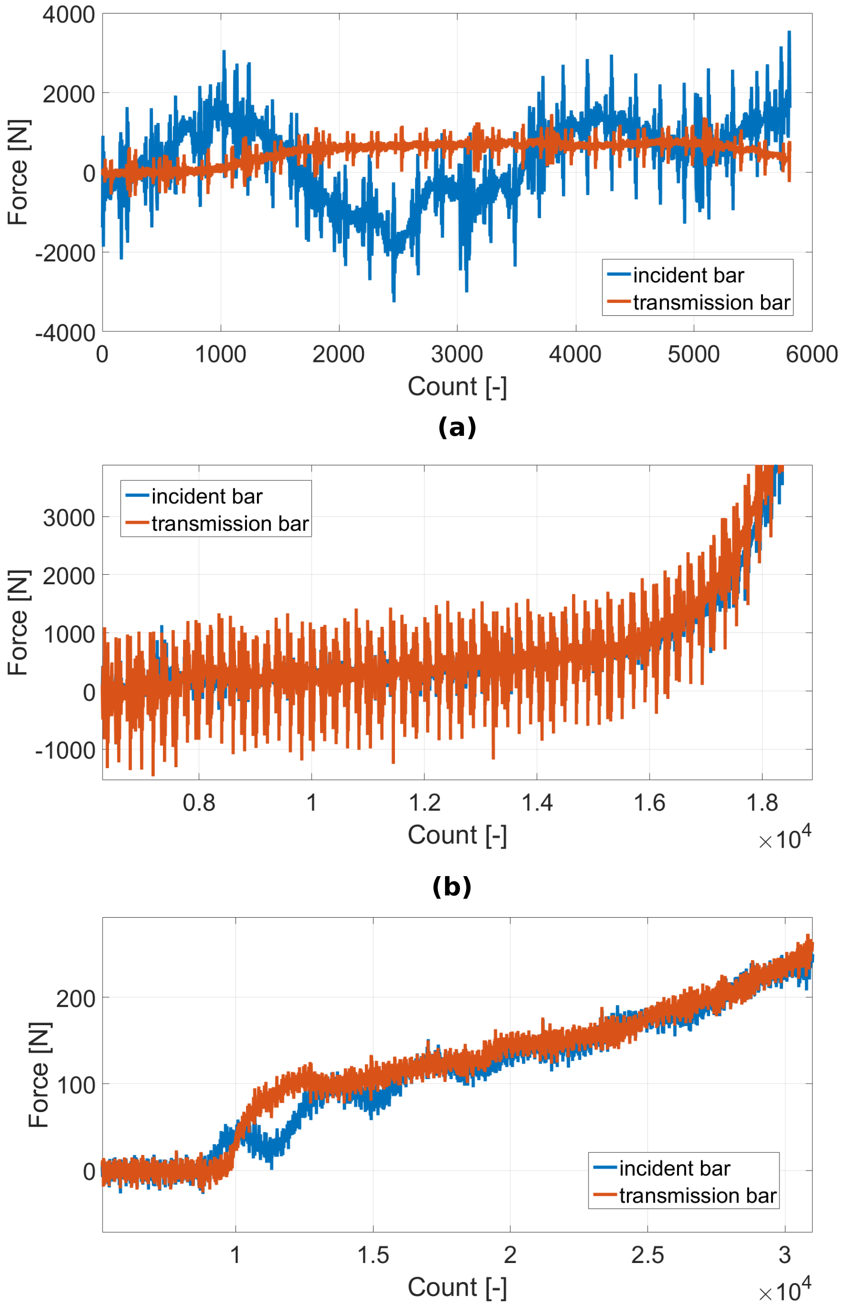

(a)

(b)

(c)

Figure 5.68: The force equilibrium of the Al-foam in the three representative cases.

the improvement in the quality of the measured force equilibrium can be attributed to the improvements in the instrumentation and the related parts. In Fig. 5.68a, the forces in the SHPB during the experiment are shown. Note, that dynamic equilibrium was not achieved, as the incident signal is significantly oscillating around the transmission signal and the noise levels are as high as 2 kN. This experiment was not valid. In Fig. 5.68b, the results of the experiment conducted in the OHPB are shown. In this experiment, equilibrium was reached and the experiment can be considered valid, however the noise levels were still high because of the wiring (approx. 1 kN) and the reliability of the curves is questionable. In the last experiment (see Fig. 5.68c), the OHPB with in-house twisted-pairs was used. Note that the noise levels are significantly reduced, the specimen deforms under the equilibrium condition and the experiment can be reliably evaluated even with forces as low as 50 N.

5.17 Experimental curiosities

The safety of the measurements is a very important task as can be shown in this paragraph. Here, a few examples of failures during the measurements are presented. A broken infrared protective window embedded in the safety shield is shown in Fig. 5.69. The destruction of the transmission bar by a cracked specimen is shown in the upper part of Fig. 5.70. The rapid escape of the specimen from the setup and its collision with the safety shield is shown in the bottom part of Fig. 5.70.

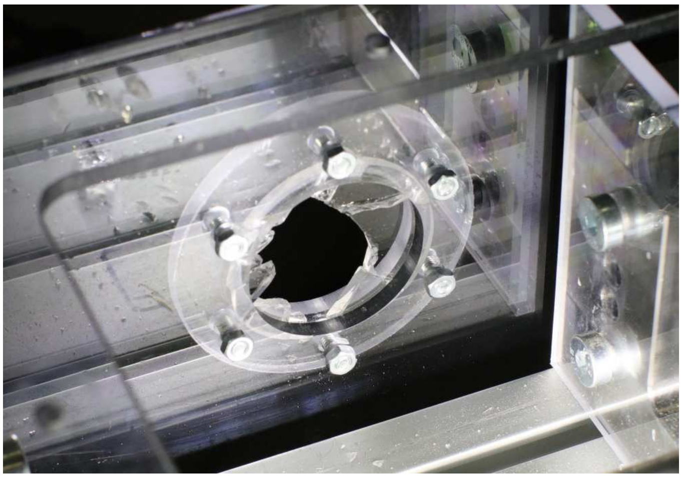

Figure 5.69: A broken infrared protective window embedded in the safety shield - damage in the amount of approx. 1000 EUR.

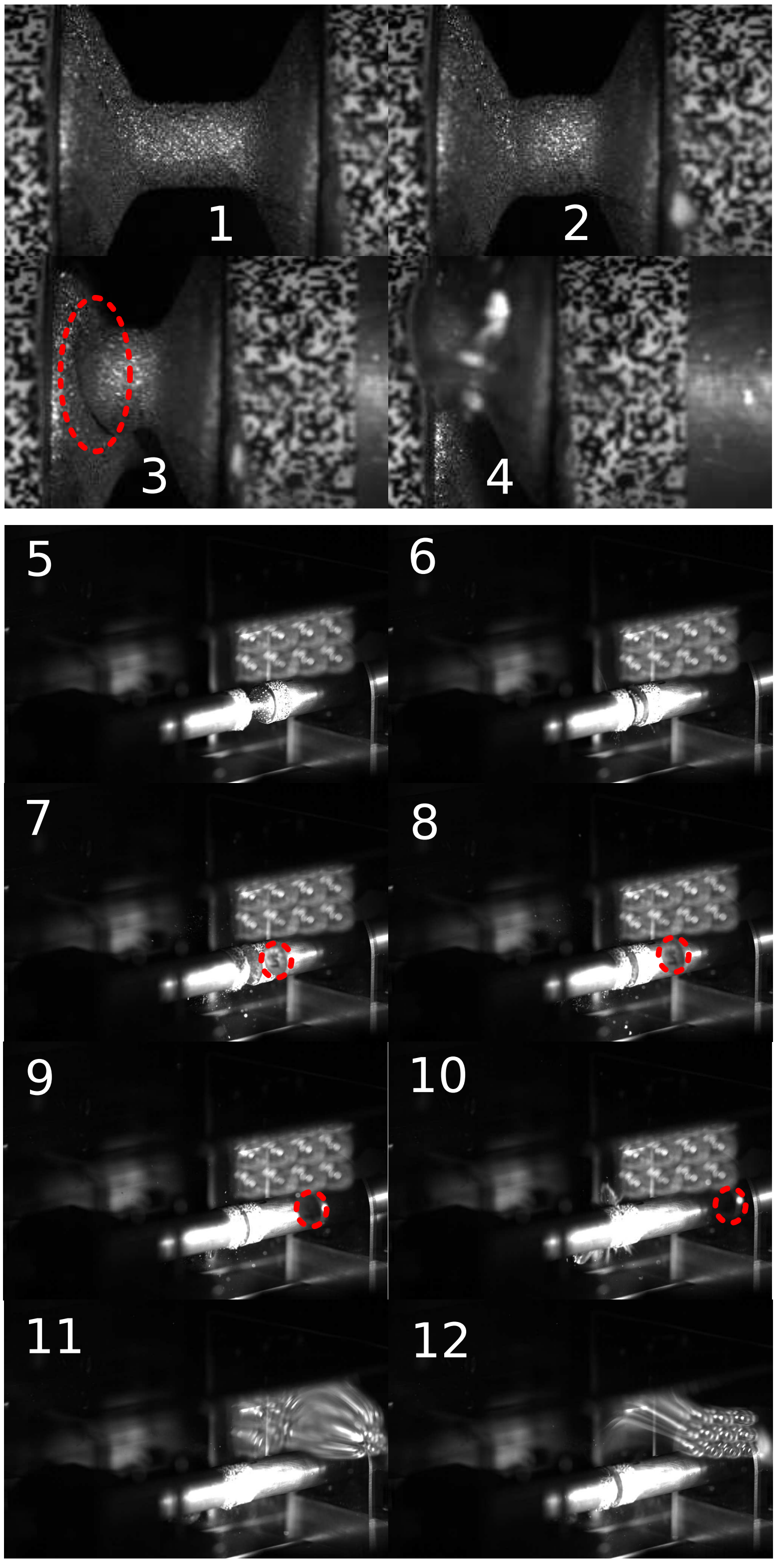

Figure 5.70: The destruction of the transmission bar by the cracked specimen (upper two rows, no. 1-4). The rapid escape of the specimen and its collision with the safety shield (bottom four rows, no. 5-12).

Chapter 6

Discussion

In this section, an overview of the most-important results of the thesis is provided and discussed. The main results and findings can be summarized in the following points:

- A modular SHPB experimental setup optimized for the testing the structural cellular meta-materials was developed and successfully tested in several experimental campaigns.
- Several types of bars (both linear elastic and visco-elastic), setup arrangements and instrumentation were tested to find the optimal settings for the testing the cellular structures using Hopkinson bar.
- The SHPB setup with a high-performance single stage gas-gun, high-strength aluminum alloy bars and cylindrical soft copper pulse-shapers with an optimized diameter exhibit the best results in terms of the quality of the measured signals, dynamic equilibrium and uniformity of the deformation.
- Foil strain-gauges were found to be superior to the semiconductor strain-gauges for the Hopkinson bar methods as they exhibit high linearity, load capacity and service-life.
- Optical inspection of the experiment using a high-speed camera is a crucial point of the testing and it has to be performed in every experiment

with the cellular structure.

- DIC is a vital technique for the advanced analysis of the displacement and strain fields. The technique was successfully applied for testing the cellular metallic meta-materials.
- The SHPB method has limitations for testing the cellular meta-materials in a lower range of strain-rates as it is complicated to achieve a high strain in the specimen. For the SHPB setup with a gas-gun, increasing the strain in the specimen requires a longer striker bar that can be physically realized only to a limited extent.
- A novel direct-impact OHPB method was employed to overcome the limitations and problems of SHPB testing of cellular materials. A modular OHPB experimental setup was developed and successfully utilized for the impact testing of the structural cellular meta-material in the lower strain-rate range of the SHPB method.
- The OHPB is found to be a vital method for testing in a lower range of the SHPB. Moreover, the evaluation of the experimental data is found to be less demanding.
- Calibration of the visco-elastic PMMA bars in the SHPB is problematic at high impact velocities ($> 20\,\mathrm{ms}^{-1}$) where the strain pulses have high amplitudes. In this case, the calibration of the visco-elastic wave propagation model is valid only for short distances ($< 1000\,\mathrm{mm}$).
- Application of the visco-elastic PMMA bars in the OHPB is rather simple as, in the direct-impact method, the amplitudes of the strain pulses are low with long pulse wavelengths. Together with the short propagation distances, the required correction for the wave dispersion effects is minimal. Bending of the relatively non-stiff PMMA bar has to be prevented during the direct impact.
- Auxetic lattices produced with additive manufacturing using selective laser sintering method were tested using both the SHPB and OHPB experimental devices at a variety of strain-rates. Three types of representative auxetic lattices were investigated: (i) a 2D re-entrant honeycomb, (ii) a 3D re-entrant honeycomb, and (iii) a missing-rib structure.
- DIC was successfully employed for the evaluation of the displacement and strain fields in all types of auxetic lattices.

- DIC was used for the evaluation of the function of Poisson's ratio in the quasi-static and dynamic experiments. Three different methods were used for the evaluation of Poisson's ratio in all three types of auxetic lattices. All the methods produced similar and comparable results.
- All three auxetic lattices exhibited strain-rate sensitive behavior affecting their stress-strain response.
- The strain dependency as well as strain-rate sensitivity of Poisson's ratio was identified in the case of the 2D re-entrant honeycomb and the missing-rib structure.
- The effect of the strain-rate sensitive fillings tested in the auxetic structures was detectable in the SHPB experiments. The fillings increased Poisson's ratio (reduced auxeticity) of the lattices. The successful experimental investigation of the filling materials within the cellular structures allowed for the further analysis in the related research.
- A case study with additively manufactured auxetic lattices subjected to dynamic compression at different temperatures was performed. The study identified that interconnected strain-rate sensitivity and thermal softening effects occur in the auxetic lattices produced from the powdered austenitic steel.
- The SHPB and OHPB methods were found to be applicable for both the hybrid lightweight open-cell foams and the hybrid auxetic lattices.
- The OHPB with visco-elastic bars was identified as a vital method for the high strain-rate testing of the specimens with very low mechanical impedance. With the visco-elastic OHPB experimental setup, it was possible to reliably measure forces as low as 100 N.
- A set of the acquired data and results has been used as the input to finite elements based numerical simulations. The numerical simulations of the auxetic structures has been a topic of the related research.

Chapter 7

Conclusions

In this thesis, a complex experimental investigation of cellular meta-materials, particularly additively manufactured auxetic lattices, was carried out at high strain-rates using several Hopkinson bar methods. Two modular experimental setups were developed for such an application: (i) a conventional SHPB apparatus based on the Kolsky arrangement, and (ii) a direct impact OHPB apparatus. Both setups were optimized for testing the cellular meta-materials and lattice structures. The SHPB with the optimized geometry, high-strength aluminum alloy bars and pulse-shaping using soft copper cylinders was identified as a vital tool for testing the cellular meta-materials at high strain-rates with high precision. The OHPB, as a novel direct impact method, was very beneficial for testing in a lower range of strain-rates overcoming here the limitations of the SHPB. All the experiments were optically inspected using a high-speed camera and the data were processed using an in-house developed DIC tool. The DIC allowed for the advanced analysis of the mechanical behavior and for the reliable identification of the displacement and strain-fields as well as Poisson's ratio. Additively manufactured auxetic lattices made of powdered austenitic steel using selective laser sintering as well as hybrid cellular metals were successfully tested using both the SHPB and OHPB. The additively manufactured auxetic lattices exhibited strong strain-rate sensitivity while the strain-rate sensitivity of the hybrid structures was not profound and, if present, was lower than the precision of the testing methods. The auxetic lattices exhibited the negative Poisson's ratio in the quasi-static as well as in the dynamic compression. Moreover, for some structures, Poisson's ratio was found to be strain as well as strain-rate dependent. To conclude, Hopkinson bar method was adapted for the testing of cellular meta-materials, particularly auxetic lattices, and novel findings about their deformation behavior under dynamic impact have been drawn.

Appendix A

Bibliography

[1] T. Fíla, P. Zlámal, O. Jiroušek, J. Falta, P. Koudelka, D. Kytýř, T. Doktor, and J. Valach. Impact testing of polymer-filled auxetics using split hopkinson pressure bar. *Advanced Engineering Materials*, 19(10), 2017.

[2] T. Fíla. Split hopkinson pressure bar: Design parameters and prediction of the experiment output. In *24th International Conference Engineering Mechanics, ENGMECH 2018*, pages 213–216, 2018.

[3] T. Fíla, P. Zlámal, J. Falta, T. Doktor, P. Koudelka, D. Kytýř, M. Adorna, J. Luksch, M. Neuhäuserovtomá, J. Valach, and O. Jiroušek. Testing of auxetic materials using hopkinson bar and digital image correlation. In *EPJ Web of Conferences*, volume 183, 2018.

[4] T. Fíla, P. Koudelka, P. Zlámal, J. Falta, M. Adorna, M. Neuhäuserová, J. Luksch, and O. Jiroušek. Strain dependency of poisson's ratio of sls printed auxetic lattices subjected to quasi-static and dynamic compressive loading. *Advanced Engineering Materials*, 21(8), 2019.

[5] T. Fila and et. al. Hybrid polymer-nickel auxetic structures: Testing using open hopkinson bar, digital image correlation and high-speed thermography. In *DYMAT Technical Meeting 2019*, 2019.

[6] P. Koudelka and et. al. Temperature dependent compressive characteristics of additively manufactured stainless-steel auxetic lattices at high strain-rate. In *DYMAT Technical Meeting 2019*, 2019.

[7] J. Falta, T. Fíla, M. Adorna, and P. Zlámal. Optimization of hopkinson bar instrumentation for testing of cellular and low impedance materials. In 25^{th} *International Conference Engineering Mechanics, ENGMECH 2019*, pages 97–100, 2019.

[8] I. G. Taylor. The use of flat-ended projectiles for determining dynamic yield stress i. theoretical considerations. *Proc. R. Soc. Lond. A*, 1948.

[9] A. C. Whiffin and I. G. Taylor. The use of flat-ended projectiles for determining dynamic yield stress ii. tests on various metallic materials. *Proc. R. Soc. Lond. A*, 1948.

[10] C. Zener and J. H. Hollomon. Effect of strain rate upon plastic flow of steel. *Journal of Applied Physics*, 15(1):22–32, 1944.

[11] H. Kolsky. An investigation of the mechanical properties of materials at very high rates of loading. *Proceedings of the Physical Society.Section B*, 62(11):676–700, 1949.

[12] J. H. Hollomon and C. Zener. Problems in fracture of metals. *Journal of Applied Physics*, 17(2):82–90, 1946.

[13] C. Zener and J. H. Hollomon. Problems in non-elastic deformation of metals. *Journal of Applied Physics*, 17(2):69–82, 1946.

[14] C. Wert and C. Zener. Interstitial atomic diffusion coefficients. *Physical Review*, 76(8):1169–1175, 1949.

[15] S. R. Bodner and Y. Partom. Constitutive equations for elastic-viscoplastic strain-hardening materials. *Journal of Applied Mechanics, Transactions ASME*, 42(2):385–389, 1975.

[16] D. J. Steinberg, S. G. Cochran, and M. W. Guinan. A constitutive model for metals applicable at high-strain rate. *Journal of Applied Physics*, 51(3):1498–1504, 1980.

[17] G. R. Johnson and W. H. Cook. Fracture characteristics of three metals subjected to various strains, strain rates, temperatures and pressures. *Engineering Fracture Mechanics*, 21(1):31–48, 1985.

[18] M. A. Meyers, Y. B. Xu, Q. Xue, M. T. Pérez-Prado, and T. R. McNelley. Microstructural evolution in adiabatic shear localization in stainless steel. *Acta Materialia*, 51(5):1307–1325, 2003.

[19] A. Marchand and J. Duffy. An experimental study of the formation process of adiabatic shear bands in a structural steel. *Journal of the Mechanics and Physics of Solids*, 36(3):251–283, 1988.

[20] A. S. Khan, Y. S. Suh, and R. Kazmi. Quasi-static and dynamic loading responses and constitutive modeling of titanium alloys. *International Journal of Plasticity*, 20(12):2233–2248, 2004.

[21] M. A. Meyers, V. F. Nesterenko, J. C. LaSalvia, and Q. Xue. Shear localization in dynamic deformation of materials: Microstructural evolution and self-organization. *Materials Science and Engineering A*, 317(1-2):204–225, 2001.

[22] J. Lankford Jr. and K. A. Dannemann. Strain rate effects in porous materials. In *Materials Research Society Symposium - Proceedings*, volume 521, pages 103–108, 1998.

[23] R. Hosseinzadeh, M. M. Shokrieh, and L. Lessard. Damage behavior of fiber reinforced composite plates subjected to drop weight impacts. *Composites Science and Technology*, 66(1):61–68, 2006.

[24] G. Wu, J. Yang, and H. T. Hahn. The impact properties and damage tolerance and of bi-directionally reinforced fiber metal laminates. *Journal of Materials Science*, 42(3):948–957, 2007.

[25] M. Sadighi, T. Pärnänen, R. C. Alderliesten, M. Sayeaftabi, and R. Benedictus. Experimental and numerical investigation of metal type and thickness effects on the impact resistance of fiber metal laminates. *Applied Composite Materials*, 19(3-4):545–559, 2012.

[26] S. R. Reid and C. Peng. Dynamic uniaxial crushing of wood. *International Journal of Impact Engineering*, 19(5-6):531–570, 1997.

[27] D. E. Grady and M. E. Kipp. Continuum modelling of explosive fracture in oil shale. *International Journal of Rock Mechanics and Mining Sciences and*, 17(3):147–157, 1980.

[28] R. Smerd, S. Winkler, C. Salisbury, M. Worswick, D. Lloyd, and M. Finn. High strain rate tensile testing of automotive aluminum alloy

sheet. *International Journal of Impact Engineering*, 32(1-4):541–560, 2005.

[29] Z. Xu, H. Hao, and H. N. Li. Experimental study of dynamic compressive properties of fibre reinforced concrete material with different fibres. *Materials and Design*, 33(1):42–55, 2012.

[30] M.A. Meyers, A. Mishra, and D.J. Benson. Mechanical properties of nanocrystalline materials. *Progress in Materials Science*, 51(4):427 – 556, 2006.

[31] S. Zhu and G. B. Chai. Low-velocity impact response of fibre-metal laminates - experimental and finite element analysis. *Composites Science and Technology*, 72(15):1793–1802, 2012.

[32] B. A. Gama, S. L. Lopatnikov, and J. W. Gillespie Jr. Hopkinson bar experimental technique: A critical review. *Applied Mechanics Reviews*, 57(1-6):223–250, 2004.

[33] T. Shyr and Y. Pan. Impact resistance and damage characteristics of composite laminates. *Composite Structures*, 62(2):193–203, 2003.

[34] X. Tan, B. Wang, Y. Yao, K. Yao, Y. Kang, S. Zhu, S. Chen, and P. Xu. Programmable buckling-based negative stiffness metamaterial. *Materials Letters*, 262, 2020.

[35] C. Bonatti and D. Mohr. Smooth-shell metamaterials of cubic symmetry: Anisotropic elasticity, yield strength and specific energy absorption. *Acta Materialia*, 164:301–321, 2019.

[36] P. Jiao, S. M. Nicaise, M. Azadi, J. Cortes, D. E. Lilley, W. Cha, P. K. Purohit, and I. Bargatin. Tunable tensile response of honeycomb plates with nanoscale thickness: Testing and modeling. *Extreme Mechanics Letters*, 34, 2020.

[37] Y. Jiang, Z. Liu, N. Matsuhisa, D. Qi, W. R. Leow, H. Yang, J. Yu, G. Chen, Y. Liu, C. Wan, Z. Liu, and X. Chen. Auxetic mechanical metamaterials to enhance sensitivity of stretchable strain sensors. *Advanced Materials*, 30(12), 2018.

[38] R. S. Kshetrimayum. A brief intro to metamaterials. *IEEE Potentials*, 23(5):44–46, 2004.

[39] J. U. Surjadi, L. Gao, H. Du, X. Li, X. Xiong, N. X. Fang, and Y. Lu. Mechanical metamaterials and their engineering applications. *Advanced Engineering Materials*, 21(3), 2019.

[40] Z. G. Nicolaou and A. E. Motter. Mechanical metamaterials with negative compressibility transitions. *Nature Materials*, 11(7):608–613, 2012.

[41] M. Kadic, T. Bückmann, N. Stenger, M. Thiel, and M. Wegener. On the practicability of pentamode mechanical metamaterials. *Applied Physics Letters*, 100(19), 2012.

[42] C. P. de Jonge, H. M. A. Kolken, and A. A. Zadpoor. Non-auxetic mechanical metamaterials. *Materials*, 12(4), 2019.

[43] K. E. Evans, M. A. Nkansah, I. J. Hutchinson, and S. C. Rogers. Molecular network design [7]. *Nature*, 353(6340):124, 1991.

[44] A. G. Kolpakov. Determination of the average characteristics of elastic frameworks. *Journal of Applied Mathematics and Mechanics*, 49(6):739–745, 1985.

[45] R. Lakes. Foam structures with a negative poisson's ratio. *Science*, 235(4792):1038–1040, 1987.

[46] Ken E Evans. Auxetic polymers: a new range of materials. *Endeavour*, 15(4):170 – 174, 1991.

[47] R. F. Almgren. An isotropic three-dimensional structure with poisson's ratio = -1. *Journal of Elasticity*, 15(12):427–430, 1985.

[48] P. S. Theocaris and G. E. Stavroulakis. Multilevel optimal design of composite structures including materials with negative poisson's ratio. *Structural Optimization*, 15(1):8–15, 1998.

[49] K. K. Saxena, R. Das, and E. P. Calius. Three decades of auxetics research - materials with negative poisson's ratio: A review. *Advanced Engineering Materials*, 18(11):1847–1870, 2016.

[50] H. M. A. Kolken and A. A. Zadpoor. Auxetic mechanical metamaterials. *RSC Advances*, 7(9):5111–5129, 2017.

[51] W. Wu, Y. Tao, Y. Xia, J. Chen, H. Lei, L. Sun, and D. Fang. Mechanical properties of hierarchical anti-tetrachiral metastructures. *Extreme Mechanics Letters*, 16:18–32, 2017.

[52] W. Wu, X. Song, J. Liang, R. Xia, G. Qian, and D. Fang. Mechanical properties of anti-tetrachiral auxetic stents. *Composite Structures*, 185:381–392, 2018.

[53] Y. Jiang and Y. Li. 3D printed chiral cellular solids with amplified auxetic effects due to elevated internal rotation. *Advanced Engineering Materials*, 19(2), 2017.

[54] Y. Jiang and Y. Li. Novel 3D-printed hybrid auxetic mechanical metamaterial with chirality-induced sequential cell opening mechanisms. *Advanced Engineering Materials*, 20(2), 2018.

[55] T. Li, Y. Chen, X. Hu, Y. Li, and L. Wang. Exploiting negative poisson's ratio to design 3d-printed composites with enhanced mechanical properties. *Materials and Design*, 142:247–258, 2018.

[56] T. Li, X. Hu, Y. Chen, and L. Wang. Harnessing out-of-plane deformation to design 3D architected lattice metamaterials with tunable poisson's ratio. *Scientific Reports*, 7(1), 2017.

[57] T. Li and L. Wang. Bending behavior of sandwich composite structures with tunable 3d-printed core materials. *Composite Structures*, 175:46–57, 2017.

[58] K. Kuribayashi, K. Tsuchiya, Z. You, D. Tomus, M. Umemoto, T. Ito, and M. Sasaki. Self-deployable origami stent grafts as a biomedical application of Ni-rich TiNi shape memory alloy foil. *Materials Science and Engineering A*, 419(1-2):131–137, 2006.

[59] M. N. Ali and I. U. Rehman. An auxetic structure configured as oesophageal stent with potential to be used for palliative treatment of oesophageal cancer; development and in vitro mechanical analysis. *Journal of Materials Science: Materials in Medicine*, 22(11):2573–2581, 2011.

[60] L. Jiang and H. Hu. Low-velocity impact response of multilayer orthogonal structural composite with auxetic effect. *Composite Structures*, 169:62–68, 2017.

[61] G. Imbalzano, P. Tran, T. D. Ngo, and P. V. S. Lee. Three-dimensional modelling of auxetic sandwich panels for localised impact resistance. *Journal of Sandwich Structures and Materials*, 19(3), 2017.

[62] M. Liaqat, H. A. Samad, S. T. A. Hamdani, and Y. Nawab. The development of novel auxetic woven structure for impact applications. *Journal of the Textile Institute*, 108(7):1264–1270, 2017.

[63] I. Gibson, D. W. Rosen, and B. Stucker. *Additive manufacturing technologies: Rapid prototyping to direct digital manufacturing*, pages 1–459. Additive Manufacturing Technologies: Rapid Prototyping to Direct Digital Manufacturing. 2010.

[64] L. Foster, P. Peketi, T. Allen, T. Senior, O. Duncan, and A. Alderson. Application of auxetic foam in sports helmets. *Applied Sciences (Switzerland)*, 8(3), 2018.

[65] G. Imbalzano, P. Tran, T. D. Ngo, and P. V. S. Lee. A numerical study of auxetic composite panels under blast loadings. *Composite Structures*, 135:339–352, 2016.

[66] M. Fu, Y. Chen, W. Zhang, and B. Zheng. Experimental and numerical analysis of a novel three-dimensional auxetic metamaterial. *Physica Status Solidi (B) Basic Research*, 253(8):1565–1575, 2016.

[67] S. Hou, T. Li, Z. Jia, and L. Wang. Mechanical properties of sandwich composites with 3D-printed auxetic and non-auxetic lattice cores under low velocity impact. *Materials and Design*, 160:1305–1321, 2018.

[68] A. Jung, S. Bronder, S. Diebels, M. Schmidt, and S. Seelecke. Thermographic investigation of strain rate effects in Al foams and Ni/Al hybrid foams. *Materials and Design*, 160:363–370, 2018.

[69] A. Jung, A. D. Pullen, and W. G. Proud. Strain-rate effects in Ni/Al composite metal foams from quasi-static to low-velocity impact behaviour. *Composites Part A: Applied Science and Manufacturing*, 85:1–11, 2016.

[70] N. Novak, K. Hokamoto, M. Vesenjak, and Z. Ren. Mechanical behaviour of auxetic cellular structures built from inverted tetrapods at high strain rates. *International Journal of Impact Engineering*, 122:83–90, 2018.

[71] W. Lee, Y. Jeong, J. Yoo, H. Huh, S. Park, S. H. Park, and J. Yoon. Effect of auxetic structures on crash behavior of cylindrical tube. *Composite Structures*, 208:836–846, 2019.

[72] L. Bai, C. Yi, X. Chen, Y. Sun, and J. Zhang. Effective design of the graded strut of bcc lattice structure for improving mechanical properties. *Materials*, 12(13), 2019.

[73] M. F. Rabbi, V. Chalivendra, and Y. Kim. Dynamic constitutive response of novel auxetic kevlar/epoxy composites. *Composite Structures*, 195:1–13, 2018.

[74] L. Zhou, J. Zeng, L. Jiang, and H. Hu. Low-velocity impact properties of 3D auxetic textile composite. *Journal of Materials Science*, 53(5):3899–3914, 2018.

[75] H. Wang, Z. Lu, Z. Yang, and X. Li. A novel re-entrant auxetic honeycomb with enhanced in-plane impact resistance. *Composite Structures*, 208:758–770, 2019.

[76] L. L. Hu, M. Z. Zhou, and H. Deng. Dynamic crushing response of auxetic honeycombs under large deformation: Theoretical analysis and numerical simulation. *Thin-Walled Structures*, 131:373–384, 2018.

[77] H. Wang, Z. Lu, Z. Yang, and X. Li. In-plane dynamic crushing behaviors of a novel auxetic honeycomb with two plateau stress regions. *International Journal of Mechanical Sciences*, 151:746–759, 2019.

[78] N. Novak, M. Borovinšek, M. Vesenjak, M. Wormser, C. Körner, S. Tanaka, K. Hokamoto, and Z. Ren. Crushing behavior of graded auxetic structures built from inverted tetrapods under impact. *Physica Status Solidi (B) Basic Research*, 256(1), 2019.

[79] L. Yang, O. Harrysson, H. West, and D. Cormier. Mechanical properties of 3D re-entrant honeycomb auxetic structures realized via additive manufacturing. *International Journal of Solids and Structures*, 69-70:475–490, 2015.

[80] Franziska Warmuth, Fuad Osmanlic, Lucas Adler, Matthias A. Lodes, and Carolin Koerner. Fabrication and characterisation of a fully auxetic 3D lattice structure via selective electron beam melting. *SMART MATERIALS AND STRUCTURES*, 26(2), 2017.

[81] Rui Magalhaes, P. Subramani, Tomas Lisner, Sohel Rana, Bahman Ghiassi, Raul Fangueiro, Daniel V. Oliveira, and Paulo B. Lourenco. Development, characterization and analysis of auxetic structures from braided composites and study the influence of material and structural parameters. *COMPOSITES PART A-APPLIED SCIENCE AND MANUFACTURING*, 87:86–97, AUG 2016.

[82] TC. Lim. *Micromechanical Models for Auxetic Materials.* Auxetic Materials and Structures, Engineering Materials. 2015.

[83] S. Mohsenizadeh, R. Alipour, A. Farokhi Nejad, M. Shokri Rad, and Z. Ahmad. Experimental investigation on energy absorption of auxetic foam-filled thin-walled square tubes under quasi-static loading. In Kurniawan, D and Nor, FM, editor, *2ND INTERNATIONAL MATERIALS, INDUSTRIAL, AND MANUFACTURING ENGINEERING CONFERENCE, MIMEC2015*, volume 2 of *Procedia Manufacturing*, pages 331–336, 2015. 2^{nd} International Materials, Industrial, and Manufacturing Engineering Conference, MIMEC2015, Bali, INDONESIA, FEB 04-06, 2015.

[84] F Scarpa, JR Yates, LG Ciffo, and S Patsias. Dynamic crushing of auxetic open-cell polyurethane foam. *PROCEEDINGS OF THE INSTITUTION OF MECHANICAL ENGINEERS PART C-JOURNAL OF MECHANICAL ENGINEERING SCIENCE*, 216(12):1153–1156, 2002.

[85] F Scarpa, LG Ciffo, and JR Yates. Dynamic properties of high structural integrity auxetic open cell foam. *SMART MATERIALS AND STRUCTURES*, 13(1):49–56, FEB 2004.

[86] T. C. Lim, A. Alderson, and K. L. Alderson. Experimental studies on the impact properties of auxetic materials. *PHYSICA STATUS SOLIDI B-BASIC SOLID STATE PHYSICS*, 251(2):307–313, FEB 2014.

[87] Li Yang, Ola Harrysson, Denis Cormier, Harvey West, Chun Park, and Kara Peters. Design of auxetic sandwich panels for structural applications. In *Solid freeform fabrication symposium*, volume 929, 2013.

[88] Li Yang, Ola A Harrysson, Harvey A West II, Denis R Cormier, Chun Park, and Kara Peters. Low-energy drop weight performance of cellular sandwich panels. *Rapid Prototyping Journal*, 2015.

[89] Olly Duncan, Leon Foster, Terry Senior, Andrew Alderson, and Tom Allen. Quasi-static characterisation and impact testing of auxetic foam for sports safety applications. *Smart Materials and Structures*, 25(5):054014, 2016.

[90] R. Edwin Raj, Venkitanarayanan Parameswaran, and B. S. S. Daniel. Comparison of quasi-static and dynamic compression behavior of closed-cell aluminum foam. *MATERIALS SCIENCE AND ENGINEERING A-STRUCTURAL MATERIALS PROPERTIES MICROSTRUCTURE AND PROCESSING*, 526(1-2):11–15, NOV 25 2009.

[91] J. E. Field, S. M. Walley, W. G. Proud, H. T. Goldrein, and C. R. Siviour. Review of experimental techniques for high rate deformation and shock studies. *International Journal of Impact Engineering*, 30(7):725–775, 2004.

[92] T. Nicholas. Tensile testing of materials at high rates of strain - an experimental technique is developed for testing materials at strain rates up to $103s^{-1}$ in tension using a modification of the split hopkinson bar or kolsky apparatus. *Experimental Mechanics*, 21(5):177–185, 1981.

[93] B. A. Gama, S. L. Lopatnikov, and J. W. Gillespie Jr. Hopkinson bar experimental technique: A critical review. *Applied Mechanics Reviews*, 57(1-6):223–250, 2004.

[94] TPM Johnson, SS Sarva, and S Socrate. Comparison of low impedance split-hopkinson pressure bar techniques in the characterization of polyurea. *Experimental mechanics*, 50(7):931–940, 2010.

[95] W. Chen, B. Zhang, and M. J. Forrestal. A split hopkinson bar technique for low-impedance materials. *Experimental Mechanics*, 39(2):81–85, 1999.

[96] Marco Peroni, George Solomos, and Norbert Babcsan. Development of a hopkinson bar apparatus for testing soft materials: application to a closed-cell aluminum foam. *Materials*, 9(1):27, 2016.

[97] Thomas Tancogne-Dejean, Adriaan B Spierings, and Dirk Mohr. Additively-manufactured metallic micro-lattice materials for high specific energy absorption under static and dynamic loading. *Acta Materialia*, 116:14–28, 2016.

[98] Pengfei Wang, Songlin Xu, Zhibin Li, Jinglei Yang, Chao Zhang, Hang Zheng, and Shisheng Hu. Experimental investigation on the strain-rate effect and inertia effect of closed-cell aluminum foam subjected to dynamic loading. *Materials Science and Engineering: A*, 620:253–261, 2015.

[99] Bao Yang, Liqun Tang, Yiping Liu, Zejia Liu, Zhenyu Jiang, and Daining Fang. Localized deformation in aluminium foam during middle speed hopkinson bar impact tests. *Materials Science and Engineering: A*, 560:734–743, 2013.

[100] Bing Hou, H Zhao, S Pattofatto, JG Liu, and YL Li. Inertia effects on the progressive crushing of aluminium honeycombs under impact loading. *International Journal of Solids and Structures*, 49(19-20):2754–2762, 2012.

[101] Jiagui Liu, Dominique Saletti, Stephane Pattofatto, and Han Zhao. Impact testing of polymeric foam using hopkinson bars and digital image analysis. *Polymer testing*, 36:101–109, 2014.

[102] A. Elmahdy and P. Verleysen. Challenges related to testing of composite materials at high strain rates using the split hopkinson bar technique. In *EPJ Web of Conferences*, volume 183, 2018.

[103] J. T. Hammer, T. J. Liutkus, J. D. Seidt, and A. Gilat. Using digital image correlation (DIC) in dynamic punch tests. *Experimental Mechanics*, 55(1):201–210, 2015.

[104] A. Gilat, T. E. Schmidt, and A. L. Walker. Full field strain measurement in compression and tensile split hopkinson bar experiments. *Experimental Mechanics*, 49(2):291–302, 2009.

[105] A. Gilat and J. D. Seidt. *Dynamic material characterization using digital image correlation*, volume 566 of *Applied Mechanics and Materials*. 2014.

[106] D. Fang, Y. Li, and H. Zhao. On the behaviour characterization of metallic cellular materials under impact loading. *Acta Mechanica Sinica/Lixue Xuebao*, 26(6):837–846, 2010.

[107] Lorna J Gibson and Michael F Ashby. *Cellular solids: structure and properties*. Cambridge university press, 1999.

[108] John Banhart. Manufacture, characterisation and application of cellular metals and metal foams. *Progress in Materials Science*, 46(6):559 – 632, 2001.

[109] A. Jung, E. Lach, and S. Diebels. New hybrid foam materials for impact protection. *International Journal of Impact Engineering*, 64:30–38, 2014.

[110] A. Jung and S. Diebels. Synthesis and mechanical properties of novel Ni/PU hybrid foams: A new economic composite material for energy absorbers. *Advanced Engineering Materials*, 18(4):532–541, 2016.

[111] D. Bancroft. The velocity of longitudinal waves in cylindrical bars. *Physical Review*, 59(7):588–593, 1941.

[112] C. Bacon. An experimental method for considering dispersion and attenuation in a viscoelastic hopkinson bar. *Experimental Mechanics*, 38(4):242–249, 1998.

[113] L. Wang, K. Labibes, Z. Azari, and G. Pluvinage. Generalization of split hopkinson bar technique to use viscoelastic bars. *International Journal of Impact Engineering*, 15(5):669–686, 1994.

[114] Q. Liu and G. Subhash. Characterization of viscoelastic properties of polymer bar using iterative deconvolution in the time domain. *Mechanics of Materials*, 38(12):1105–1117, 2006.

[115] M. Bussac, P. Collet, G. Gary, and R. Othman. An optimisation method for separating and rebuilding one-dimensional dispersive waves from multi-point measurements. application to elastic or viscoelastic bars. *Journal of the Mechanics and Physics of Solids*, 50(2):321–349, 2002.

[116] S. W. Park and M. Zhou. Separation of elastic waves in split hopkinson bars using one-point strain measurements. *Experimental Mechanics*, 39(4):287–294, 1999.

[117] H. Zhao and G. Gary. A new method for the separation of waves. application to the shpb technique for an unlimited duration of measurement. *Journal of the Mechanics and Physics of Solids*, 45(7):1185–1202, 1997.

[118] C. Bacon. Separation of waves propagating in an elastic or viscoelastic hopkinson pressure bar with three-dimensional effects. *International Journal of Impact Engineering*, 22(1):55–69, 1999.

[119] W. Chen, B. Zhang, and M. J. Forrestal. A split hopkinson bar technique for low-impedance materials. *Experimental Mechanics*, 39(2):81–85, 1999.

[120] W. Chen, F. Lu, and B. Zhou. A quartz-crystal-embedded split hopkinson pressure bar for soft materials. *Experimental Mechanics*, 40(1):1–6, 2000.

[121] D. J. Frew, M. J. Forrestal, and W. Chen. Pulse shaping techniques for testing brittle materials with a split hopkinson pressure bar. *Experimental Mechanics*, 42(1):93–106, 2002.

[122] D. J. Frew, M. J. Forrestal, and W. Chen. A split hopkinson pressure bar technique to determine compressive stress-strain data for rock materials. *Experimental Mechanics*, 41(1):40–46, 2001.

[123] Z. J. Rohrbach, T. R. Buresh, and M. J. Madsen. Modeling the exit velocity of a compressed air cannon. *American Journal of Physics*, 80(1):24–26, 2011.

[124] W. B. Stephenson. *Theoretical light gas-gun performance*. ASTIA, Arlington, 1961.

[125] A. E. Seigel. *Performance Calculations and Optimization of Gas Guns*. US Army, Adelphi, 1981.

[126] F. Gallina, R.S. Birch, and M. Alves. Design of a split hopkinson pressure bar. In *Proceedings of COBEM*, page art. no. 1558, 2003.

[127] O. Jiroušek, T. Doktor, D. Kytýř, P. Zlámal, T. Fíla, P. Koudelka, I. Jandejsek, and D. Vavřík. X-ray and finite element analysis of deformation response of closed-cell metal foam subjected to compressive loading. *Journal of Instrumentation*, 8(2), 2013.

[128] J. Falta, T. Fíla, P. Zlámal, and M. Adorna. Instrumentation of split hopkinson pressure bar for testing of cellular metallic materials. In 16^{th} *Youth Symposium on Experimental Solid Mechanics, YSESM 2018*, pages 10–14, 2018.

[129] J. Falta. *Instrumentation of Split Hopkinson Pressure Bar Setup for Dynamic Measurement - master thesis.* Czech Technical University, Prague, 2017.

[130] Yinggang Miao, X. Gou, and Zakir Sheikh. A technique for in-situ calibration of semiconductor strain gauges used in hopkinson bar tests. *Experimental Techniques*, 42, 09 2018.

[131] Yinggang Miao, Yulong Li, Q. Deng, Zhongbin Tang, H.-T Hu, and Tao Suo. Investigation on experimental method of low-impedance materials using modified hopkinson pressure bar. *Journal of Beijing Institute of Technology (English Edition)*, 24:269–276, 06 2015.

[132] Farhana Pervin, Weinong W Chen, and Tusit Weerasooriya. Dynamic compressive response of bovine liver tissues. *Journal of the mechanical behavior of biomedical materials*, 4(1):76–84, 2011.

[133] Jiangyue Zhang, Narayan Yoganandan, Frank A Pintar, Yabo Guan, Barry Shender, Glenn Paskoff, and Purushottam Laud. Effects of tissue preservation temperature on high strain-rate material properties of brain. *Journal of biomechanics*, 44(3):391–396, 2011.

[134] M. Adorna. *Evaluation of Dynamic Experiments Performed Using Split Hopkinson Pressure Bar - master thesis.* Czech Technical University, Prague, 2017.

[135] *Journal of the Society of Motion Picture Engineers: High-Speed Photography*, volume Preface p.5. 1949.

[136] M. Hudak. *Upgrade of SHPB for Advanced Measurements in transportation - master thesis.* Czech Technical University, Prague, 2018.

[137] M. Adorna, P. Zlámal, T. Fíla, J. Falta, M. Felten, M. Fries, and A. Jung. Testing of hybrid nickel-polyurethane foams at high strain-rates using hopkinson bar and digital image correlation. In 16^{th} *Youth Symposium on Experimental Solid Mechanics, YSESM 2018*, pages 72–76, 2018.

[138] M. Adorna, J. Falta, T. Fíla, and P. Zlámal. Preprocessing of hopkinson bar experiment data: Filter analysis. In 16^{th} *Youth Symposium on Experimental Solid Mechanics, YSESM 2018*, pages 77–81, 2018.

[139] R. Dvorak. *Numerical modelling of wave shapes during SHPB measurements - bachelor thesis.* Czech Technical University, Prague, 2018.

[140] T. C. Chu, W. F. Ranson, and M. A. Sutton. Applications of digital-image-correlation techniques to experimental mechanics. *Experimental Mechanics*, 25(3):232–244, 1985.

[141] I. Jandejsek, J. Valach, and D. Vavřík. Optimization and calibration of digital image correlation method. In *EAN 2010:* 48^{th} *International Scientific Conference on Experimental Stress Analysis*, pages 131–136, 2010.

[142] Bruce D Lucas, Takeo Kanade, et al. An iterative image registration technique with an application to stereo vision. 1981.

[143] D. Vavrik and I. Jandejsek. Experimental evaluation of contour j integral and energy dissipated in the fracture process zone. *Engineering Fracture Mechanics*, 129:14–25, 2014.

[144] P. Koudelka, O. Jiroušek, T. Fíla, and T. Doktor. Compressive properties of auxetic structures produced with direct 3D printing. *Materiali in Tehnologije*, 50(3):311–317, 2016.

[145] H. Zhao, I. Elnasri, and S. Abdennadher. An experimental study on the behaviour under impact loading of metallic cellular materials. *International Journal of Mechanical Sciences*, 47(4-5 SPEC. ISS.):757–774, 2005.

[146] R. A. Govender and R. J. Curry. The “open” hopkinson pressure bar: Towards addressing force equilibrium in specimens with non-uniform deformation. *Journal of Dynamic Behavior of Materials*, 2(1):43–49, 2016.

Appendix B

Attachments

The attachments of the thesis are included in its electronic version only. In the following text, a list of the attachments is provided together with a brief description of their content:

- **Attachment 1** - the technical documentation and drawings of the SHPB and the OHPB setup.
- **Attachment 2** - the MATLAB software toolbox containing a set of functions for the evaluation of both the SHPB and OHPB experiments.
- **Attachment 3** - the representative videos and slideshows showing the auxetic lattices in the impact experiments.
- **Attachment 4** - a set of images from the experimental campaigns.
- **Attachment 5** - a set of the representative results from the various experiments.